Acta Materialia 288 (2025) 120783

Contents lists available at ScienceDirect

Acta Materialia

journal homepage: www.elsevier.com/locate/actamat

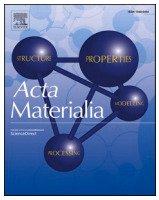

Full length article

Quantifying damage mechanisms through FE-based void tracking: Application to shear and tension in-situ laminography experiments on AA2198-T851

Christian C. Roth [a], Thilo F. Morgeneyer [b], Lukas Helfen [c,d], Dirk Mohr [a], Thomas Tancogne-Dejean [a,*]

[a] Department of Mechanical and Process Engineering, ETH Zurich, Switzerland
[b] MINES Paris, PSL University, Centre des Matériaux, CNRS UMR 7633, Evry, France
[c] Institute for Photon Science and Synchrotron Radiation, KIT, Germany
[d] Institut Laue–Langevin, CS 20156 Cedex 9, Grenoble 38042, France

ARTICLE INFO

Keywords:
Ductile fracture
Stress state
Quantitative void evolution
In situ 3D synchrotron imaging

ABSTRACT

This study presents a hybrid experimental-numerical postprocessing technique for analyzing damage evolution during in-situ tomography experiments. Using the displacement fields obtained from finite-element (FE) simulations as initial guesses, voids are tracked throughout loading by mapping their centroids to the initial configuration with a novel void tracking algorithm. This algorithm facilitates differentiation between void nucleation, growth and/or coalescence of existing voids. In-situ laminography experiments are performed on flat shear, central-hole tension, notched tension and compact tension specimens extracted from recrystallized aluminum alloy 2198-T851. The specimens are monotonically loaded all the way to fracture to gain insight into ductile failure mechanisms for predominantly biaxial stress states. Detailed 3D gray scale images are acquired at multiple stages of each experiment, allowing distinguishing between polycrystalline matrix, inter-metallic particles and voids at sub-micrometer resolution. The postprocessing of all experiments leads to a wealth of experimental data on void sizes, shapes, counts, volume fractions, and mechanisms of origin. Average stress states and macroscopic strain estimates are derived using continuum scale FE simulations with an anisotropic non-porous plasticity model and related to the void evolution. The tomographic observations show two primary damage mechanisms at early plastic straining stages: (1) intermetallic particle cracking and debonding, and (2) micro-crack emergence mainly at grain boundaries. At high plastic straining stages, grain boundary unzipping leads to fracture via micro-crack growth and coalescence, more prevalent under generalized shear than tension. It is found that particle-related void growth is slow and enhances the material's macroscopic ductility by delaying the growth of large voids.

1. Introduction

The nucleation, growth and coalescence of voids in a matrix material are the known driving mechanisms at the mesoscopic level that lead to ductile fracture of polycrystalline materials [1]. A first foundation of the field has been set by the seminal work of Mc Clintock [2]. Based on experiments on plasticine and theoretical analysis, he proposed a criterion for ductile fracture that accounts for the growth and the coalescence of holes. He observed a "relatively strong dependence of fracture strain on the transverse (intermediate) principal stress, rather than solely on the mean normal stress or the maximum principal stress", and noted that "changes in the size, shape, and spacing of the holes will be dependent on the entire history of stress, strain and rotation". A second important pillar for the developments in the field of ductile fracture is the work of Rice and Tracey [3]. They demonstrated an exponential dependence of the rate of void expansion on the stress triaxiality, along with a Lode parameter dependent multiplier.

Despite the attention to the intermediate principal stress and the Lode parameters in the late 1960′s, most research in the following three decades focused primarily on the roles of only two stress tensor

* Corresponding author.
E-mail address: thomatan@ethz.ch (T. Tancogne-Dejean).

https://doi.org/10.1016/j.actamat.2025.120783
Received 22 September 2024; Received in revised form 27 January 2025; Accepted 27 January 2025
Available online 28 January 2025

invariants: the hydrostatic and the von Mises stresses. The most widely used porous plasticity model is the GTN model which combines the Gurson pressure-dependent yield function [4], with a phenomenological void nucleation law [5], an evolution law for void growth [6], and void coalescence [7]. As pointed out in [8], any constitutive relation based on a standard Gurson-type plastic potential presumes that the voids remain essentially spherical. Numerous extensions have been made accounting for effects such as matrix anisotropy (e.g. [9]), strain rate (e.g. [10]) or void shape effects (e.g. [11–13]). It is only recent enhancements that incorporate the effect of the Lode parameter (e.g. [14–16]), but at the expense of partially losing the model's connection with micro-mechanics. Aside from providing mechanistic support for the development of advanced porous plasticity models, micromechanical considerations have led to comprehensive void coalescence criteria, e.g. [17–20]. The majority of micromechanical studies have primarily focused on void growth and coalescence. Experimental evidence of these phenomena is still scarce as compared to the number of computational studies. As far as void nucleation is concerned, both experimental and numerical studies are rare. Based on FE simulations, Babout et al. [21] developed a model that distinguishes between particle fracture and particle decohesion as driving nucleation mechanism. The nucleation of voids from cylindrical particles was investigated numerically by Fleck et al. [22]. Based on measurements from torsion experiments of cast aluminum A356, Horstemeyer et al. [23] introduced a void nucleation rule that, besides plastic strain, depends on the stress triaxiality and the Lode angle parameter. Another attempt in formulating an advanced nucleation law based on experimental evidence has been made by Morgeneyer and Besson [24].

Most recent experimental insight into the ductile fracture process has been derived from in-situ X-ray experiments. Maire and Withers [25] provide a comprehensive overview of computed tomography techniques in the context of mechanical testing. They conclude that computed tomography is an ideal means for following micro- and mesostructural developments over time. Using X-ray micro-tomography, Landron et al. [26] found a dependence of the void nucleation on the stress triaxiality for a dual phase (DP) steel. Toda et al. [27] investigated a DP steel with combined phase- and absorption-contrast tomography under tensile loading. They identified various nucleation sites, e.g. the ferritic or the martensitic interior or the corresponding interface. However, only limited growth was observed from these sites. In contrast, rapid growth was observed post force maximum from cracked martensite locations, exhibiting shear-dominated growth under macroscopic tension. Maire et al. [28] investigated three commercial aluminum alloys with different work hardening and strength using three different notched specimens by X-ray tomography. They conclude that smaller notches, i.e. fields of higher triaxiality, accelerate both nucleation and growth.

Landron et al. [29] used tensile experiments to assess the growth of voids in three steels using micro-tomography. Manually measuring the 20 largest pores, they found that besides the (anticipated) growth of single voids, the void shape also changed for the ferritic and the dual phase steel from initially spherical to prolate. Croom et al. [30] investigated ductile failure of high-purity copper wires with X-ray tomography. They showed that the dominant damage mechanism transitioned from shear localization to the nucleation of micron-sized voids, followed by void coalescence and subsequent growth of the coalesced cavities. They also emphasize the interaction of different mechanisms, concluding that the shear band drives the nucleation and growth of voids. As a result, coalescence occurs along the shear band rather than transverse to the axial load.

Madi et al. [31] investigate the effect of the material anisotropy on damage mechanisms for a X100 high-grade pipeline steel. They show how particles and their initial alignment influence the orientation of void nucleation and subsequent void growth using in-situ synchrotron tomography experiments. Hannard et al. [32] investigated the effect of the spatial arrangement of intermetallic particles on ductile failure for three aluminum alloys subjected to tensile loading. They report that while the yield and hardening responses are isotropic, one of the aluminum alloys exhibits a strongly anisotropic fracture response. They show that particle clustering in the as-produced material is the precursor for two coalescence stages, comprising intra- and inter-cluster coalescence, leading to an anisotropic fracture response. Recently, Vaughan et al. [33] combined crystal-plasticity finite element simulations with 3D X-ray computed tomography to investigate void growth rates in a cylindrical Al-2219.

Lecarme et al. [34] investigated the void growth in Ti-6-Al4 V by void tracking in 3D microtomography images throughout loading. They employed a graph-based data association to identify voids and measure their evolution with strain. More recently, Azman et al. [35] carried out experiments using synchrotron micro-tomography and a void tracking algorithm that allow distinction between nucleation, growth and coalescence. Another example regarding the sequence of void nucleation, growth and coalescence is shown in Guo et al. [36], who performed time-lapse synchrotron computed tomography (CT) on ferritic steel with tapered tensile specimens.

The limitation of classic tomography to axisymmetric or cylindrical specimen is overcome by synchrotron laminography [37]. Micro-laminography is particularly adapted to investigate damage evolution in regions of interest of flat samples at micrometer resolution [38].

Using recrystallized AA2198-T851 for in-situ micro-laminography, Buljac et al. [39] showed that shear damage micro-mechanisms involved detrimental grain-related flat cracks as major damage feature. These were identified as both intergranular and transgranular in [40]. A second type of damage feature was also found: intermetallic particle breakage normal to the maximal stress direction, but with limited effect on the final crack. Void growth was detected during shearing since rigid particle debris kept the voids open. Kong et al. [41] performed load path changes from shear to tension on a cruciform-shaped specimen in AA2198-T851, in which the same two main types of damage features were found: grain-related flat cracks and intermetallic particle cracks. Damage nucleation was observed at the end of shear pre-loading at nearly zero stress triaxiality, and subsequently the nucleated damage continued to grow and lead to final fracture during tension loading after the shear pre-strain. The processes were modelled in [42]. Under tension loading of a CT-like sample early strain localization in form of slant bands was found ahead of the notch in Morgeneyer et al. [43] for the AA2198-T851 material before damage onset.

In the present work, we present a new methodology to analyze the damage evolution during in-situ laminography (i.e. tomography) experiments on ductile materials. The central idea is to make use of the displacement field computed through accompanying finite element simulations to map experimentally-observed voids from the current configuration back to the initial configuration. This allows for the accurate tracking of voids throughout loading, thereby enabling the quantification of the mechanism of nucleation, growth and coalescence. In-situ laminography experiments are performed on shear, central hole-, notched- and compact-tension specimens extracted from aluminum alloy AA2198-T851 sheets. The new processing methodology is then applied to gain detailed insight into the effect of the stress state on the nucleation, growth and coalescence of voids.

All experimental procedures are presented in Section 2, while Section 3 presents the void tracking algorithm. The main results are presented in Section 4, where the mechanical fields, the void tracking algorithm performance and the void population are analyzed in depth for each specimen geometry. The last two sections present a discussion and conclusion of the findings. Details on the finite element analysis and extended experimental results are presented in appendices A to E.

2. Experimental procedures

2.1. Material

The material under investigation is a 2 mm thick recrystallized alu-

Table 1
Nominal chemical composition of AA2198-T851 (in wt%).

Cu	Li	Zn	Mn	Mg	Zr	Si	Ag	Fe
2.9–3.5	0.8–1.1	<0.35	<0.5	0.25–0.8	0.04–0.18	<0.08	0.1–0.5	<0.01

Table 2
Results from uniaxial tensile experiments on AA2198-T851.

	$\sigma_y[MPa]$	$\sigma_{UTS}[MPa]$	$\varepsilon_{p,UTS}[-]$	Lankford ratio r
Rolling direction (RD)	480	536	0.057	0.48
Diagonal direction (DD)	445	532	0.074	0.52
Transverse direction (TD)	449	527	0.051	0.53

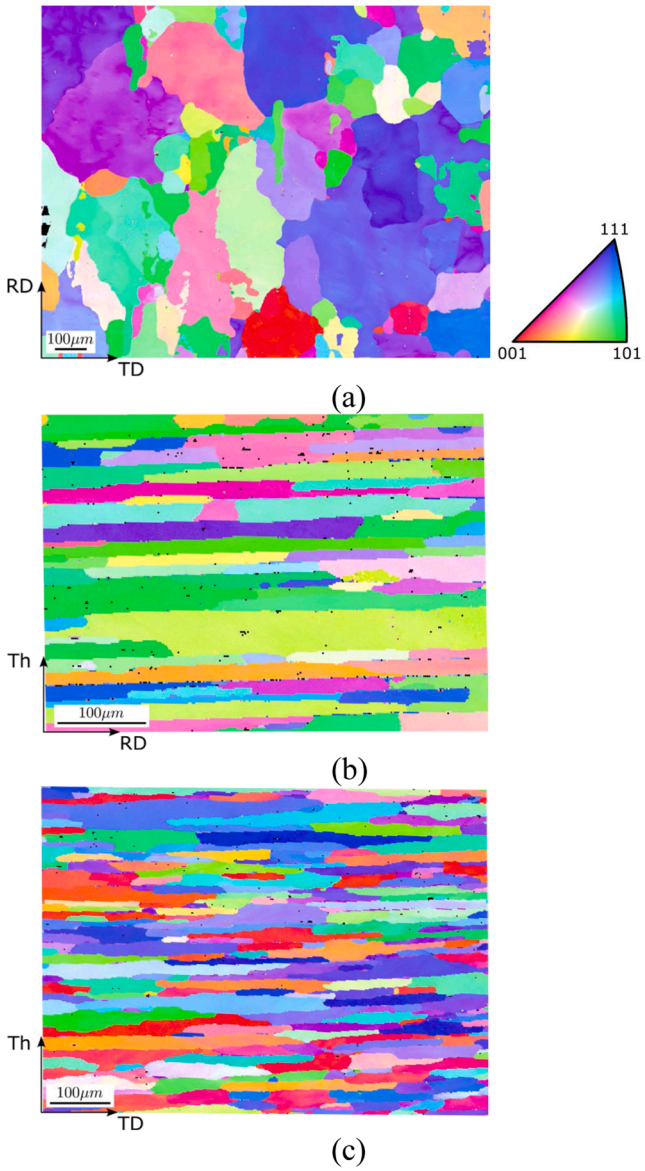

Fig. 1. Electron Backscatter Diffraction (EBSD): Inverse Pole Figure (IPF) revealing the pancake microstructure of the AA2198-T851 sheet. Note the difference in- and out-of-plane grain sizes of 82μm in RD, 80μm in TD and 20μm in Th directions, based on mean linear intercept method.

minum–copper–lithium alloy AA2198 in artificial temper T851. It is obtained from a cold rolling process followed by solution heat treatment, water quenching, stretching and artificial ageing. Its nominal chemical composition (in wt%) is given in Table 1. Yield stresses of about $\sigma_{y,RD} = 480MPa$, $\sigma_{y,DD} = 445MPa$ and $\sigma_{y,TD} = 449MPa$ are measured from uniaxial tensile tests for the rolling (RD), diagonal (DD) and transverse (TD) direction [43,44], indicating a slight anisotropy of the material. Irrespective of the specimen orientation, an ultimate tensile stress of about 530 MPa and Lankford ratios of about 0.5 are observed (Table 2).

Electron Backscatter Diffraction (EBSD) analyses with a step size of 2 μm are performed in a scanning electron microscope (Scios, FEI) using an acceleration voltage of 20kV. For this, the specimens are prepared by mechanical grinding with a 4000 grit SiC paper, followed by polishing with a diamond suspension and finishing with a silica colloid with a grain size of 50nm. The out-of-plane inverse pole figure (Fig. 1a) shows large flat grains with major diameters of up to 500 μm and an average of 82 μm in RD and 80 μm in TD measured using a mean linear intercept method. The two orthogonal through-thickness inverse pole figures (Fig. 1b-c) reveal highly elongated grains with an average thickness of 20 μm, corresponding to an aspect ratio of 20. A comparable microstructure was reported for the same alloy and temper in [45].

Energy Dispersive X-ray spectroscopy (EDX) is performed on a Zeiss Evo 10 with Oxford Instrument XMax^N. Intermetallic particles are embedded in the aluminum matrix (BSD sensor), some of which expose clear cracks. Fe and Cu-rich particles of angular shape and diameters between 5 and 15 μm are found as well as lithium-rich round precipitates of up to 2 μm size, which form bands aligned with the rolling direction. It is also noted that some of the iron and copper are dissolved within the matrix. The intermetallic particles' volume fraction is around 3.5×10^{-3}, while an initial porosity of less than 3×10^{-4} is observed [41].

2.2. Specimens

All laminography specimens are extracted from the base material using wire-electric discharge machining (EDM). The thickness of all specimens is reduced to 1 mm by milling under permanent cooling. The following four geometries (Fig. 2) are considered, probing specific stress states:

- Simple shear specimen: a "smiley" shear specimen (SH) with two parallel gage sections of height 1.5 mm (Fig. 2a), as described in [46].
- Uniaxial tension specimen: A central hole specimen (CH) with a single central circular cut-out of 4 mm diameter and a 10 mm wide gage section (Fig. 2c).
- Plane strain tension specimen: A notched tension specimen (NT) with 14 mm wide shoulder regions and two circular cut-outs of radius 2 mm, effectively reducing the width of the central gage section to 5 mm (Fig. 2d).
- High stress triaxiality specimen: A compact tension-like specimen (CT) of 60 mm width and 70 mm height with a straight unilateral cut of length 36 mm; the cut is made using an EDM with a wire of diameter 0.34 mm (Fig. 2g).

For all specimens, the loading direction corresponds to the transverse direction. All coordinates are reported with respect to the coordinate systems presented in Fig. 2. The origin is located at the center of SH, CH and NT specimen, and at the location of the extensometer for the CT specimen. The x-axis corresponds to the rolling direction (RD), the y-axis to the transverse direction (TD) and the z-axis to the thickness direction (th).

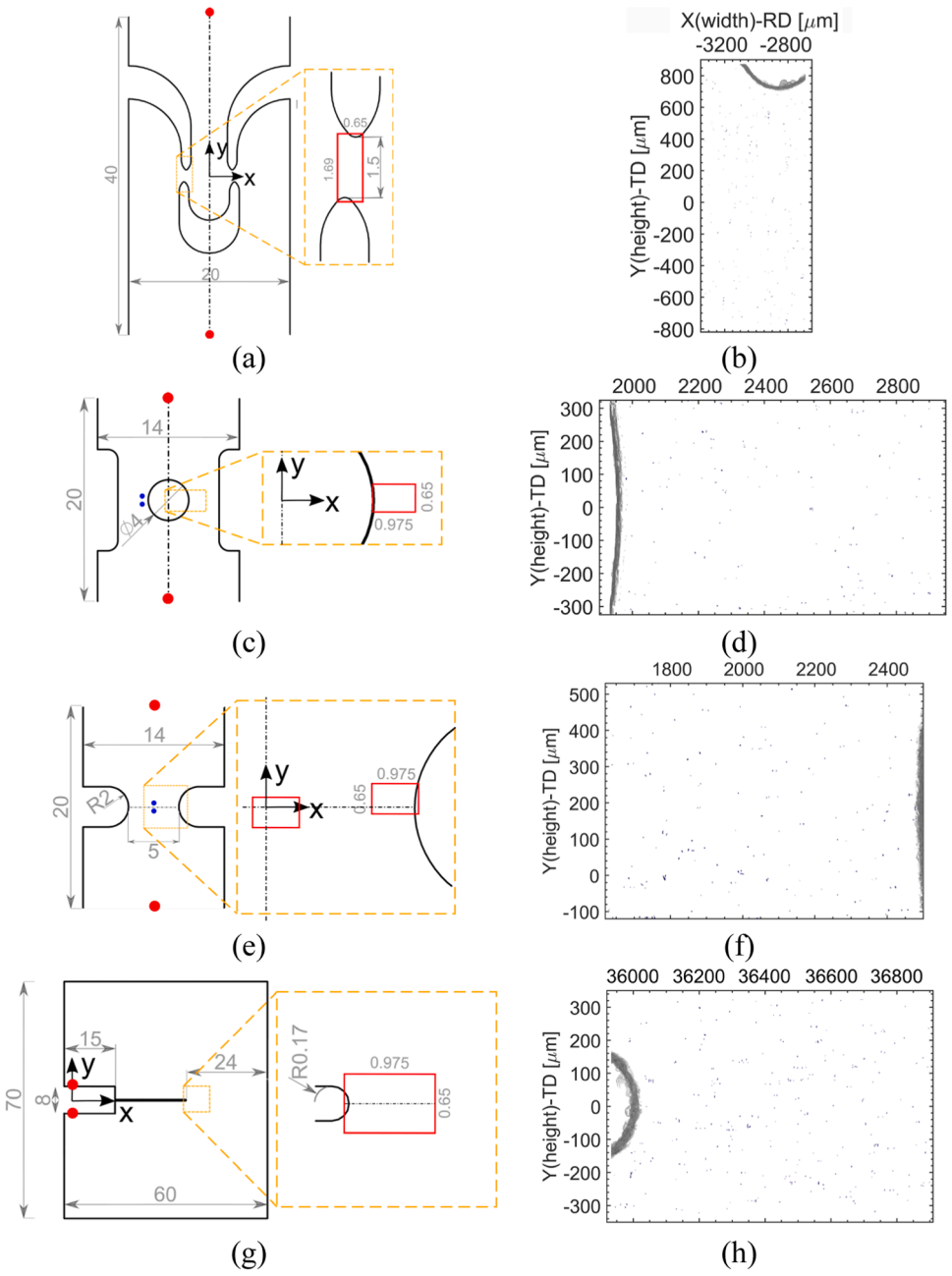

Fig. 2. Left column: Specimen geometries: (a) SH, (c) CH, (e) NT and (g) CT. Red dots highlight the position of the virtual extensometer for global displacement measurements. Blue dots denote the location of the local axial strain measurement. The red boxes denote the size and position of the laminography measurement region of interest, each of which has a thickness (out-of-plane) of 0.65 mm (0.7 mm for CT). Right column: Corresponding reconstructed and segmented regions of interest in the first step with porosities (blue) and free surfaces (light gray). (For interpretation of the references to colour in this figure legend, the reader is referred to the web version of this article.)

2.3. Synchrotron laminography experiments

Synchrotron laminography [37,38] is used for 3D imaging of the local regions of interest (red boxes, Fig. 2). All laminography experiments are performed on the imaging beamline ID19 of the European Synchrotron Radiation Facility (ESRF, Grenoble, France). The displacement steps are applied onto the pin-loaded specimens in a stepwise manner using a screw-driven loading device equipped with a 5 kN load cell (ME-Messsysteme KD40 s). The load frame is positioned on a rotating stage for laminography purposes. After each load increment, a series of radiographs is acquired, while the test frame (with the mounted specimen) is rotated around the laminographic axis. The axis of rotation is inclined with respect to the transmitted X-ray beam direction by an angle of about $\theta \approx 65°$. Details of the setup are shown in [43].

For each of the SH, CH and NT specimens, 3000 radiographs per 360° turn are acquired with a 25 keV pink beam under continuous specimen rotation with an indirect detector system [47]. This provides an effective voxel size of 0.65μm. The series of acquired 2D projections is then used to reconstruct 3D volumes using a GPU-accelerated implementation of a filtered-back projection algorithm [48–50]. The CT specimen volumes are reconstructed from 1500 angularly-equidistant radiographs with an exposure time of 250 ms for each projection and a voxel size of 0.7 μm. The minimum specimen to detector distance is 70 mm, leading to relatively strong edge enhancement due to phase contrast [51]. For all specimens, the region of interest extends 1000 voxels in the thickness direction, with an 8-bit gray level resolution.

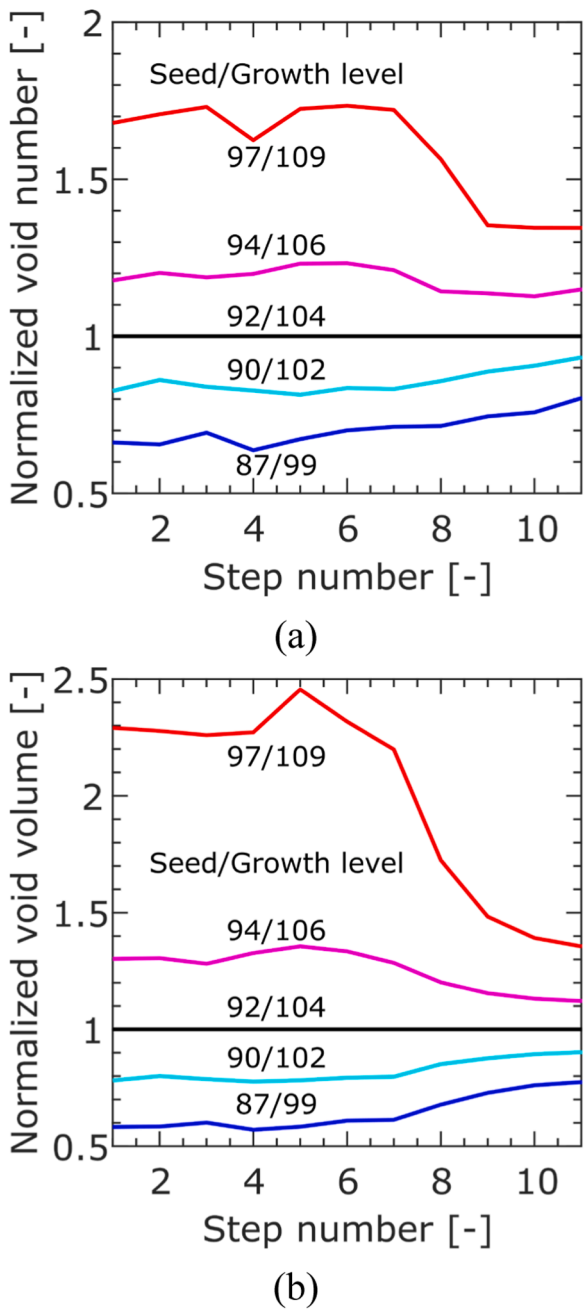

Fig. 3. Segmentation sensitivity study: effect of $a \pm 2$ and ± 5 variation in grey level for the seed and growth thresholding on the (a) normalized void number and (b) the normalized void volume for all loading steps of the NT-center specimen.

Besides the laminography acquisition system, a 5MP optical camera with 105 mm lens is used to observe the specimen surface and perform digital image correlation (DIC) at each loading step. Prior to testing, a fine black-and-white spray paint speckle pattern is applied. The commercial digital image correlation software VIC 2D-v6 (Correlated Solutions) is used with a subset size of 59 and a step size of 8. An eight-tap spatial grayscale interpolation is chosen to achieve sub-pixel accuracy. The strain fields are computed using a Gaussian filter of size 5. The effective surface strain is then calculated from the DIC measurements as

$$\bar{\varepsilon} = \frac{2}{\sqrt{3}}\sqrt{\varepsilon_I^2 + \varepsilon_I \varepsilon_{II} + \varepsilon_{II}^2}. \tag{1}$$

2.4. Ex-situ reference experiments and fractography

To complement the in-situ experiments, the SH-, CH- and NT-experiments are also performed ex-situ on a universal testing system at a constant cross-head velocity of 0.4mm/min. The system is equipped with custom-made high-pressure clamps [52]. A 12MP camera (Point Grey, Model GS3-U3–120S6M-C) along with a macro lens (Tokina, f2.8, 100 mm focal length) is used to acquire images at a frequency of 1 Hz, with a spatial resolution of about 3.1μm/pixel. The results from the in-situ and ex-situ experiments are linked using the DIC-based surface displacement measurements.

The fracture surface of all ex-situ experiments is observed post-mortem in a scanning electron microscope (Scios dual beam, FEI), with an acceleration voltage of 20kV. For selected locations with intermetallic particles, images from back-scattered electron (BSE) and Secondary Electron (SE) detectors are superimposed with the software GIMP's inbuilt "overlay" function to highlight chemical and topological contrast. The matrix appears dark gray, while the particles are shown in lighter gray.

3. Void tracking

The laminography technique allows for observing a fixed region of interest (red box in Fig. 2) of a specimen during in-situ experiments. As the specimen deforms, material and voids might flow in and out of this region (Eulerian observation). Here, we will restrict the investigation to the smallest ensemble of material points that can be monitored throughout the experiment (Lagrangian observation), denoted as the *trackable volume*. In the sequel, we propose a void tracking algorithm to monitor the evolution of voids comprised in the trackable volume throughout the loading. The algorithm will also serve as a classifier indicating if an observed void nucleated or evolved due to growth or coalescence.

3.1. Void identification and characterization

Segmentation of the gray scale voxel images is performed with a region growing algorithm [53] to separate voids from the matrix material. Initial seeding is carried out for gray levels below 92, while the voids are grown to gray levels of 104. This choice also helps to differentiate between laminography artefacts, actual voids and particles. To account for possible artefacts and errors of the laminography technique, $3 \times 3 \times 3$ voxel cubes are chosen as minimum void volume, corresponding to a physical volume of $7.41\mu m^3$ for the SH-, CH- and NT-experiments and $9.26\mu m^3$ for the CT-experiments. Gaps in some of the very large voids present in the last steps of the experiments are manually closed based on visual inspection of all slices of the corresponding step.

To assess the uncertainties related to the region growing algorithm, a sensitivity study is carried out in the vicinity of the chosen values. Varying the grayscale by ± 2 and ± 5 for the seed and growth values, a variation of up to ± 20 %/± 70 % in the initial void number and $+40$ %/$+140$ % in the initial void volume fraction (VVF) can be obtained (Fig. 3). However, as voids grow during loading and become more easily detectable, this uncertainty reduces to about ± 10 %/± 20 % for the last loading step before fracture.

The function "regionprops3" of the software Matlab R2019b is used to extract selected quantities from the segmented 3D images. Herein, the centroid coordinates, as well as the volume of each void are extracted together with the principal axis length of a hypothetical ellipsoid featuring the same second moment of inertia. Feret's shape factor F is then computed from the ratio of the minimum over the maximum principal axis length [31,54]. It is used as a metric to distinguish spherical voids ($F = 1$) from ellipsoidal voids ($F = 0$). As it cannot distinguish between needle- and pancake-shaped ellipsoids, we

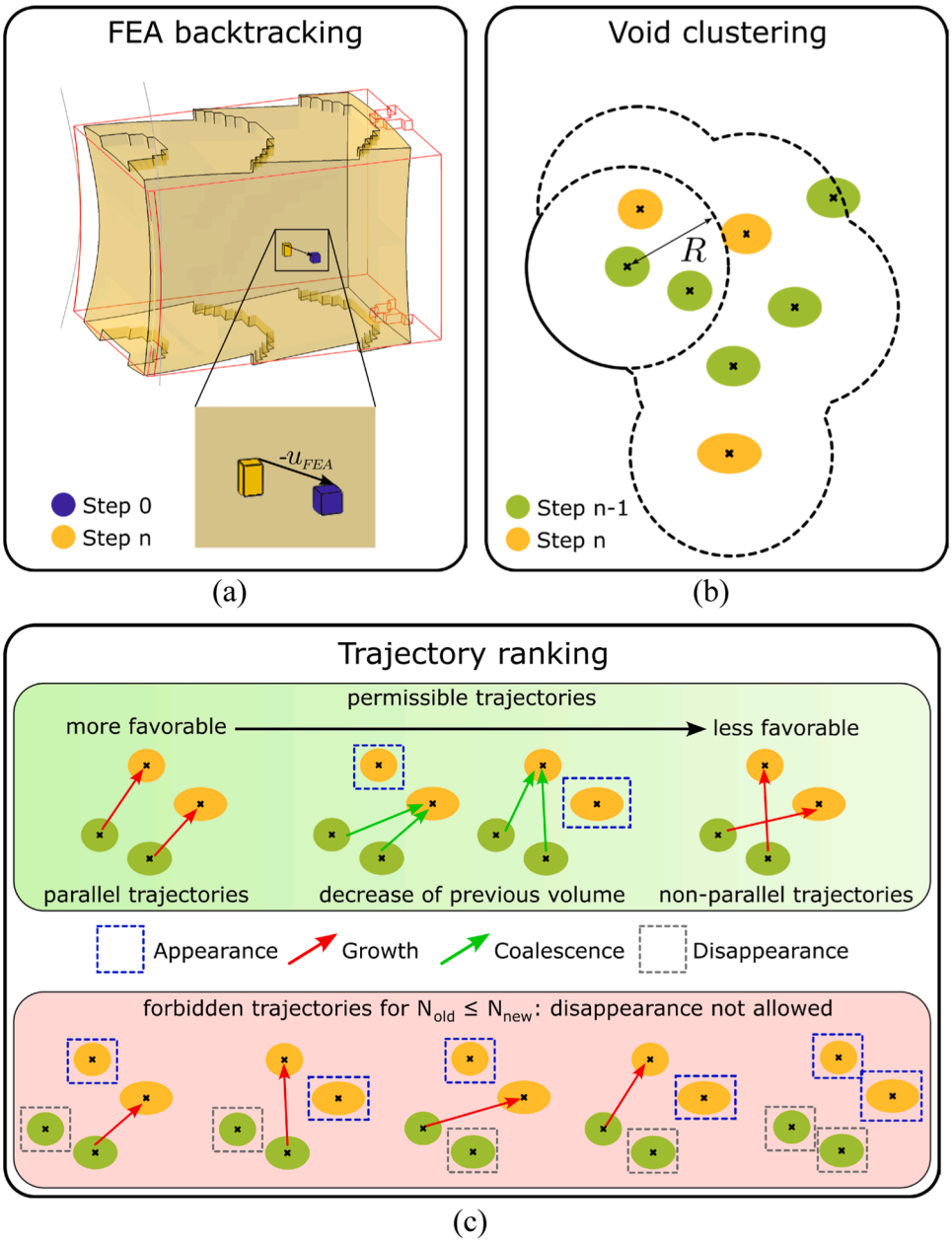

Fig. 4. Schematic of the components of the void tracking algorithm: (I) FEA-based volume translation with observable volume (red frame) and trackable volume at step n (light brown). (II) Identification of void clusters within radius R. (III) Possible void trajectories for the tracking algorithm from step n-1 to step n. Cases (1)-(4) (top) are permissible, while (5)-(9) (bottom) are forbidden for $N_{old} \leq N_{new}$ due to the disappearance of voids. (For interpretation of the references to colour in this figure legend, the reader is referred to the web version of this article.)

introduce the normalized principal moments of inertia as an additional metric. These are calculated based on the extracted principal moments of inertia $I_1, I_2, I_3, (I_1 \geq I_2 \geq I_3)$ of the voids

$$\lambda_i = \frac{I_i}{I_1 + I_2 + I_3},\ i \in [1, 2, 3]. \tag{2}$$

with the ordered principal axis length $r_1 \geq r_2 \geq r_3$ of the corresponding ellipsoids, the first two values can be written as

$$\lambda_1 = \frac{r_1^2 + r_2^2}{2\left(r_1^2 + r_2^2 + r_3^2\right)} \text{ and } \lambda_2 = \frac{r_1^2 + r_3^2}{2\left(r_1^2 + r_2^2 + r_3^2\right)}, \tag{3}$$

effectively removing any dependence on the volume and making it solely a metric of the void shape. This metric allows an even finer separation of spheres ($\lambda_1 = \lambda_2 = 1/3$) from disk-shaped ($\lambda_1 = 0.25, \lambda_2 = 0.5$) and needle-shaped ($\lambda_1 = 0.5, \lambda_2 = 0.5$) voids [55]. Constant Feret shape factors can be represented with isolines in the principal moments of inertia spaceλ_1, λ_2 as:

$$\lambda_1 = \frac{1}{2} - \frac{F^2}{1 + F^2}\lambda_2 \tag{4}$$

3.2. Region of interest and trackable volume

For each in-situ laminography experiment, we perform a non-porous finite element simulation. Details on the solid element meshes, boundary conditions and the non-porous constitutive framework are given in Appendix A. The trackable volume for a given experiment is then defined by all elements that are comprised within the laminographically-observable volume for all stages of loading.

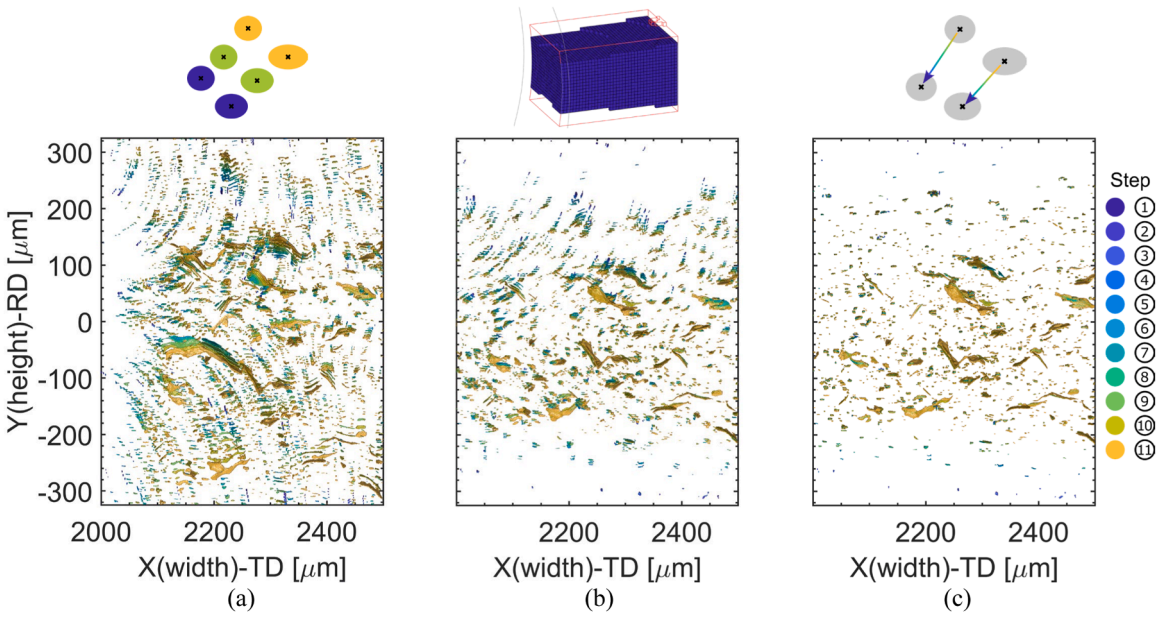

Fig. 5. Void tracking algorithm: Example of a projected 3D view of a subregion of the CH specimen. All loading steps (a) as obtained in the experiment, (b) after FEA-based volume translation and (c) after void tracking are shown. Each void is colored according to the corresponding loading step, while the matrix is made transparent. Note the evolution in the displacement field for the different loading steps, which is completely removed after the two-step translation and void tracking procedure.

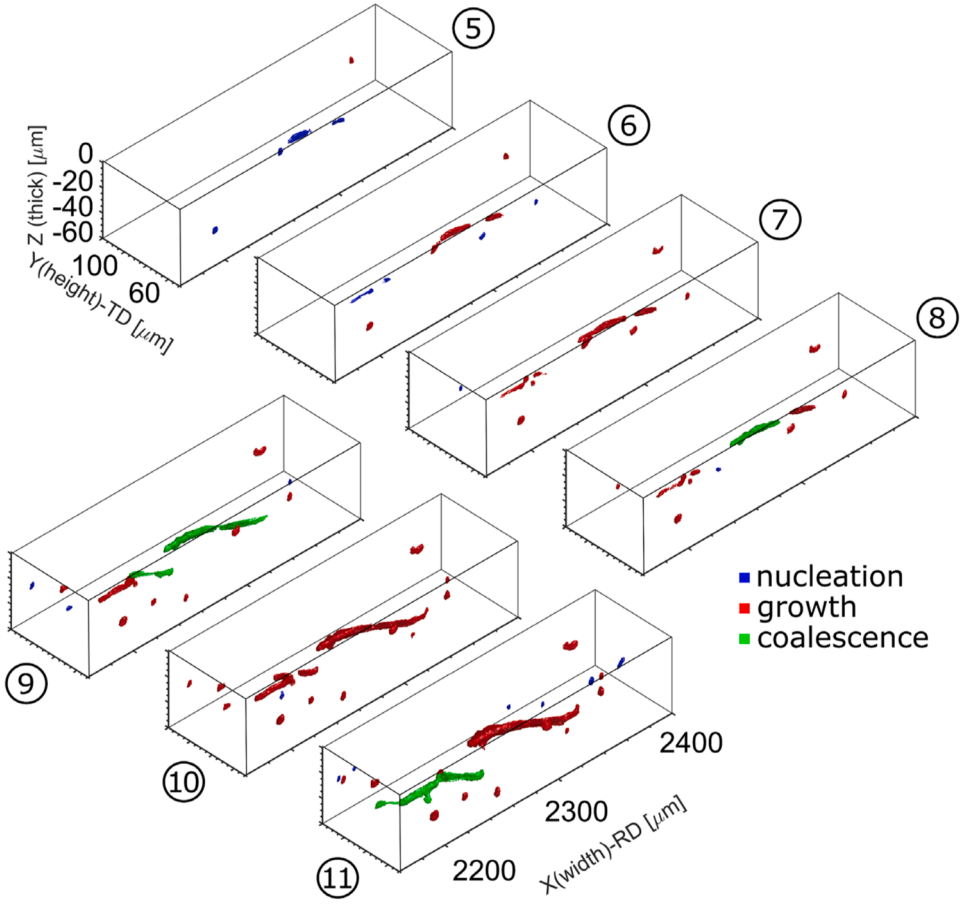

Fig. 6. Void evolution mechanism labeling: selected steps from a subregion of the CH experiment. Voids are labelled according to the identified evolution mechanism towards the current step: nucleation (blue), growth (red), coalescence (green). Note the re-occurrence of coalescence. (For interpretation of the references to colour in this figure legend, the reader is referred to the web version of this article.)

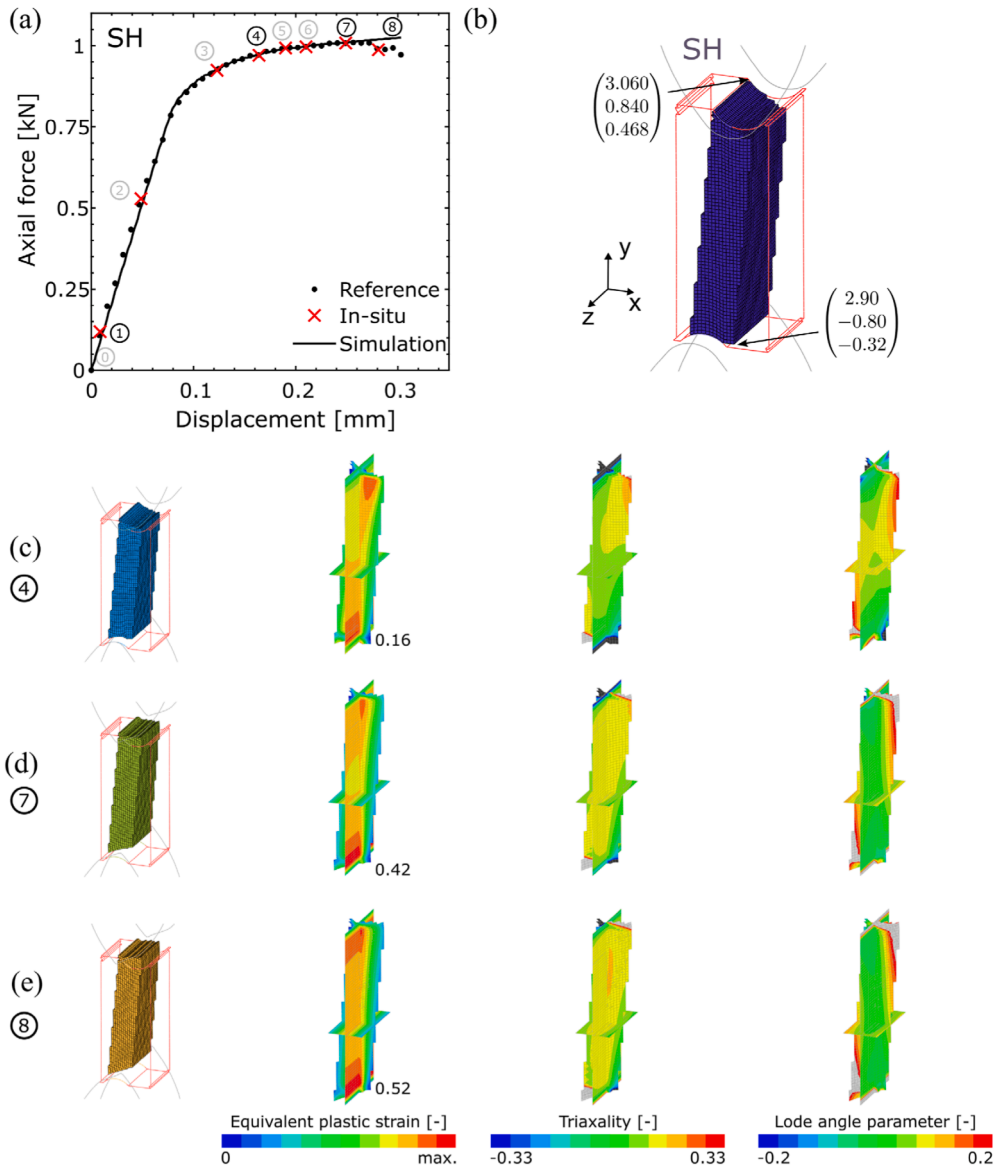

Fig. 7. Results from the numerical simulation of the SH specimen: (a) Force-displacement curve of the reference (black dots) and the in-situ (red crosses) experiments along with the numerical simulation (solid black line). (b) Observable (red frame) and trackable volume (FE mesh). (c)-(e) Evolution of the equivalent plastic strain, the stress triaxiality and the Lode angle parameter for selected steps. Note that the three orthogonal planes in (c)-(e) correspond to $x = 2.98$ mm, $y = 0$ mm and $z = 0$mm. (For interpretation of the references to colour in this figure legend, the reader is referred to the web version of this article.)

Fig. 7–11b show the observable (red frame) and trackable (FE mesh) volumes for all experiments. It should be noted that the trackable volume can be up to 37 % smaller than the observable volume, depending on the specimen.

An initial estimate of all void centroid locations in the reference configuration is obtained by translating (pulling back) the centroid of each void for every step based on the corresponding FE-obtained displacement (Fig. 4a). Fig. 5 shows an example of such a translation of the centroids in the current configuration (Fig. 5a) to the initial configuration (Fig. 5b). It should be noted that this FE-based processing method relies on the assumption of material homogeneity and the accurate alignment of the coordinate systems from the experiment and the numerical simulation for each loading step. More advanced finite element simulations, e.g. based on crystal plasticity, might lead to an improved initial guess. However, any misalignment between the FE and the experimental coordinate systems results in artificial rigid body motions, as shown exemplarily in Fig. 5b ($100\mu m < y < 200\mu m$) and requires a second tracking step.

3.3. Void tracking algorithm

The above FE-based void centroid translation can only serve as an initial guess of the position of the voids in the reference configuration. Besides compensating for the approximate nature of the numerical simulation as well as frame misalignments, a second step of void tracking allows classification of each void's evolution. For two subsequent loading steps (n-1) and (n), we consider four possible evolution scenarios: (i) void nucleation,[1] (ii) void growth, (iii) void coalescence and (iv) void disappearance.

To determine the most likely evolution event for a void between two subsequent steps (n-1) and (n), the following algorithm is proposed:

[1] The term "nucleation" is used throughout this paper to refer to voids that appear in our laminography images. In reality, we cannot rule out that these are pre-existing voids (rather than newly nucleated ones) that have just become visible due to void growth.

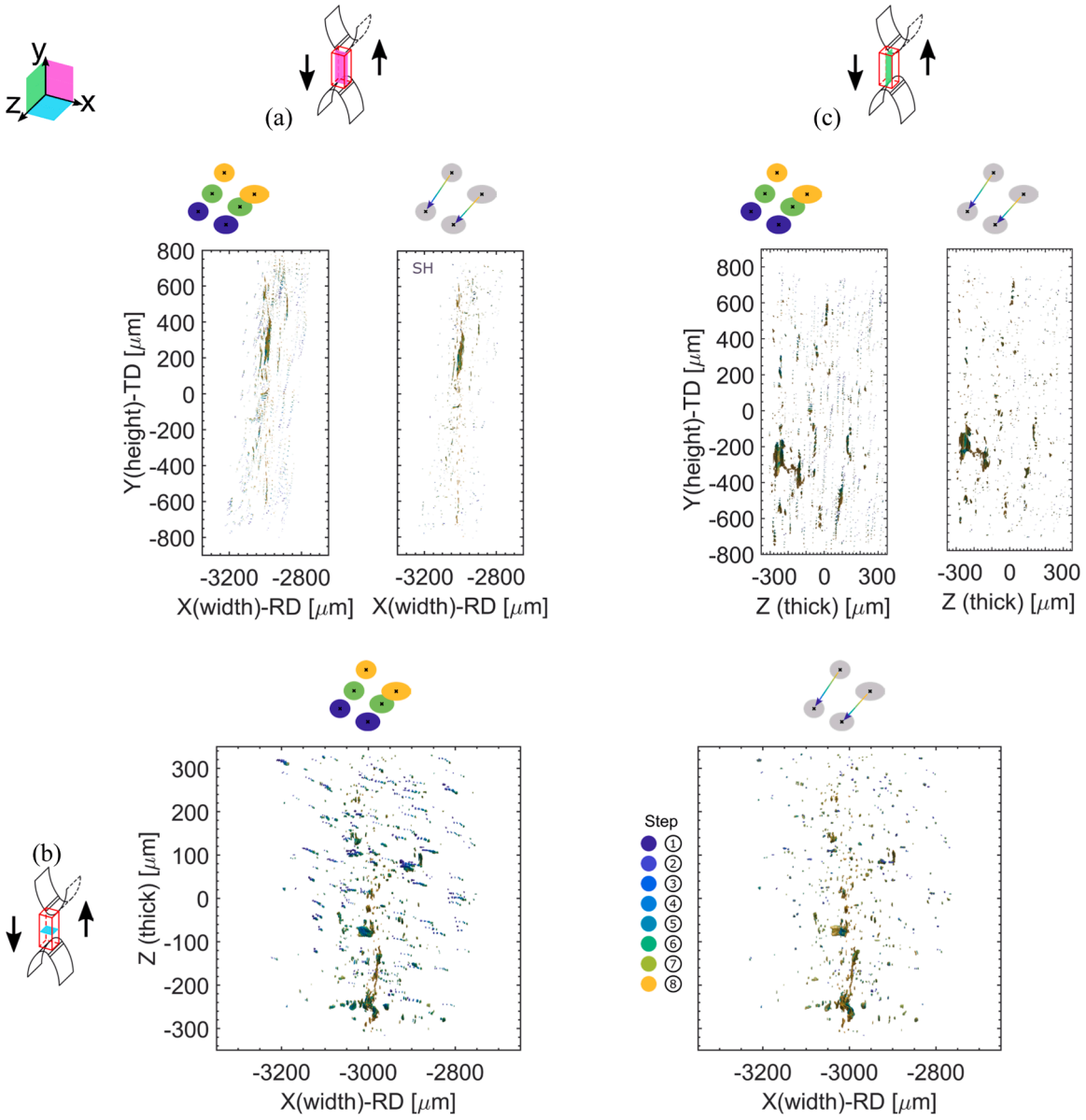

Fig. 8. Projected 3D views of the trackable volume of the SH specimen (left columns) before and (right columns) after void tracking for the (a) xy-, (b) the xz- and (c) the yz-plane. Each void is colored according to the corresponding loading step, while the matrix is made transparent. Note the evolution in the displacement field for the different loading steps (compare Fig. 7a), which is completely removed after the two-step translation and void tracking procedure.

1. Initially, void clusters are identified for both steps by recursively searching for neighboring voids (from either step) within a 15 µm radius sphere (dashed line Fig. 4b). For all considered cases, the maximum cluster size is nine voids.
2. For every void cluster, all possible evolutions, i.e. sets of void trajectories from the previous step to the current step, are defined (Fig. 4c). For a cluster of N_{old} voids and N_{new} voids (with $N_{old} \leq N_{new}$), and considering all possible cases of nucleation, growth and coalescence, each of the old voids can be randomly assigned to a new void, resulting in ${N_{new}}^{N_{old}}$ possible evolutions. Note that a new void can be assigned multiple times, which corresponds to coalescence. Void disappearance is only considered if $N_{old} > N_{new}$. This special case results in an additional $N_{old}!/(N_{old} - N_{new})!$ number of evolutions to be evaluated (Fig. 4c).
3. For every possible evolution, we compute the individual displacement vectors between all void centroids from step (n-1) to step (n), along with their direction and norm (distance traveled by the centroid). This allows directly assessing the difference between maximum and minimum centroid displacement for all voids in the current step cluster. Further, considering all possible void trajectories, the dot product of the normalized displacement vectors, i.e. the direction. is computed.
4. To choose the most likely set of trajectories, a cost function is then evaluated. It is based on a weighted sum of the average dot product and the average distance difference. An evolution is then assigned to the cluster if it is unique and if it features an ensemble motion close to a translation (average dot product above threshold 0.5). Note that depending on the number of old and new voids, more than one permissible trajectory might exist. If the ensemble motion is not close to a translation, the possible trajectories are set to include coalescence.
5. For these remaining cases, a second cost function is evaluated on all possible trajectories. Herein, the volume change between each new void and its related old voids is computed for all possible evolutions. The final evolution is then assigned as the set of trajectories minimizing the change in volume (min/max ratio of the volume change).

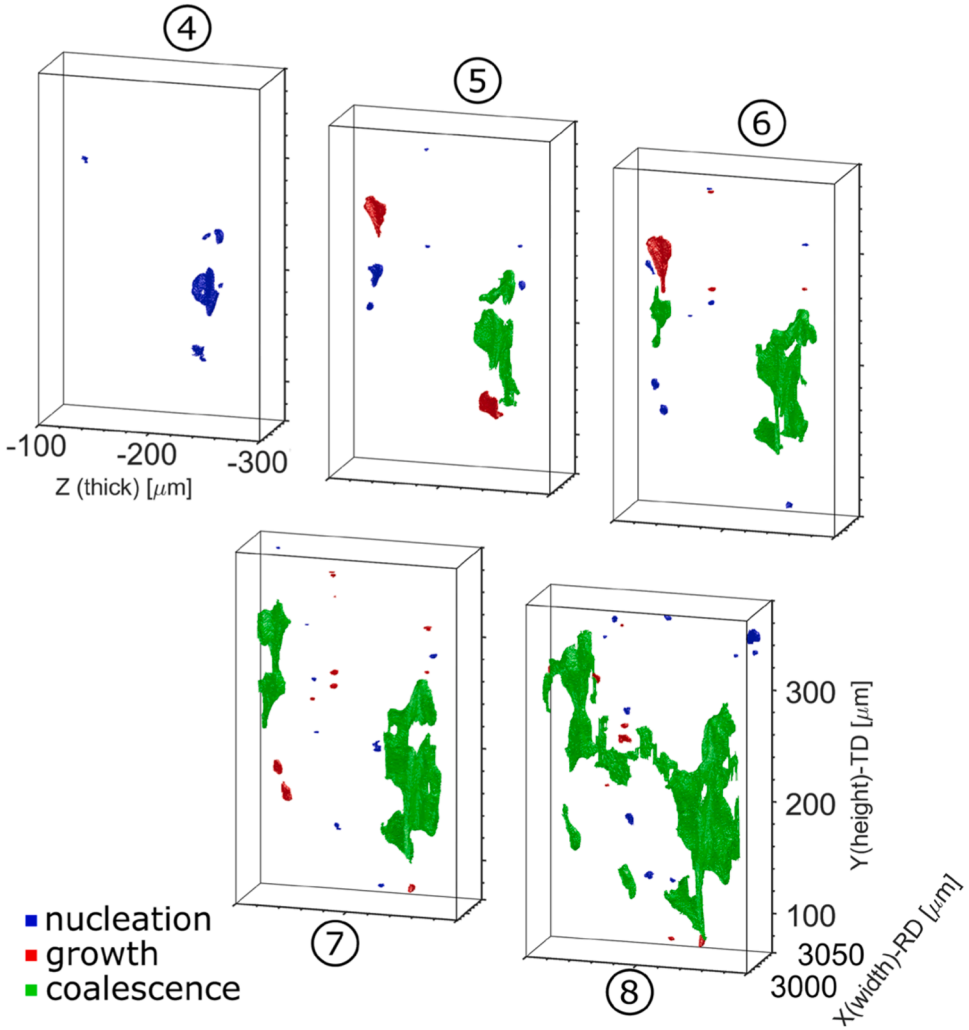

Fig. 9. Close-up view of a subregion of the SH experiment including the largest void for selected steps with mechanism labeling.

It should be noted that in the case of coalescence, the centroid of the new void is positioned at the mid-point of the previous centroids. The results of the algorithm are shown exemplary in Fig. 5c.

3.4. Analysis criteria for nucleation, growth and coalescence

The aforementioned FEA translation and backtracking algorithm allows us to label every observed void with the mechanism it originated from. Fig. 6 exemplifies this for a small volume within the CH-specimen. The voids at a step n have been colored to highlight the evolution mechanism from step n-1 to n: nucleation (blue), growth (red) or coalescence (green). The plot for step ⑤ indicates that a first set of four voids (blue) nucleated between steps ④ and ⑤, while a single small void grew (red). In the subsequent steps, the nucleated voids grow until a first coalescence (green) of the two voids in the center occurs between step ⑦ and ⑧. Additional nucleation and coalescence occur towards step ⑨ and ⑪, while the voids observed in step ⑩ are mostly the result of growth.

After assigning an evolution mechanism to each individual void, the void volume fraction and void number for each mechanism are quantified. We use the size of the deformed trackable volume as a reference to compute the void volume fractions (VVFs) for nucleation, growth and coalescence mechanisms for each step:

$$VVF^{(n)}_{mechanism} = \frac{1}{V_{trackable}} \sum_{mechanism} V^{(n)}_{mechanism}. \tag{5}$$

Similarly, the number of voids per unit volume is obtained for each mechanism by dividing the respective number of voids by the trackable volume.

4. Results

The results are reported separately for all four specimens. For each specimen, the experimental force-displacement curve along with the results from the FE analysis are presented. The stress state is discussed based on the stress triaxiality η and Lode angle parameter $\overline{\theta} \in [-1, 1]$. They are calculated from the stress invariants $\{I_1, J_2, J_3\}$ and defined as

$$\eta = -\frac{p}{\overline{\sigma}_{VM}} = \frac{I_1}{3\sqrt{3J_2}}, \tag{6}$$

$$\overline{\theta} = 1 - \frac{2}{\pi} \arccos\left[\frac{3\sqrt{3}}{2} \frac{J_3}{(J_2)^{3/2}}\right]. \tag{7}$$

This is followed by the 3D views of the reconstructed and backtracked volumes along with the evolution of selected voids and void population analyses. The initial reconstructed and segmented regions of interest are shown in Fig. 2.

4.1. Shear experiment

Fig. 7a shows the force-displacement response of the macroscopic

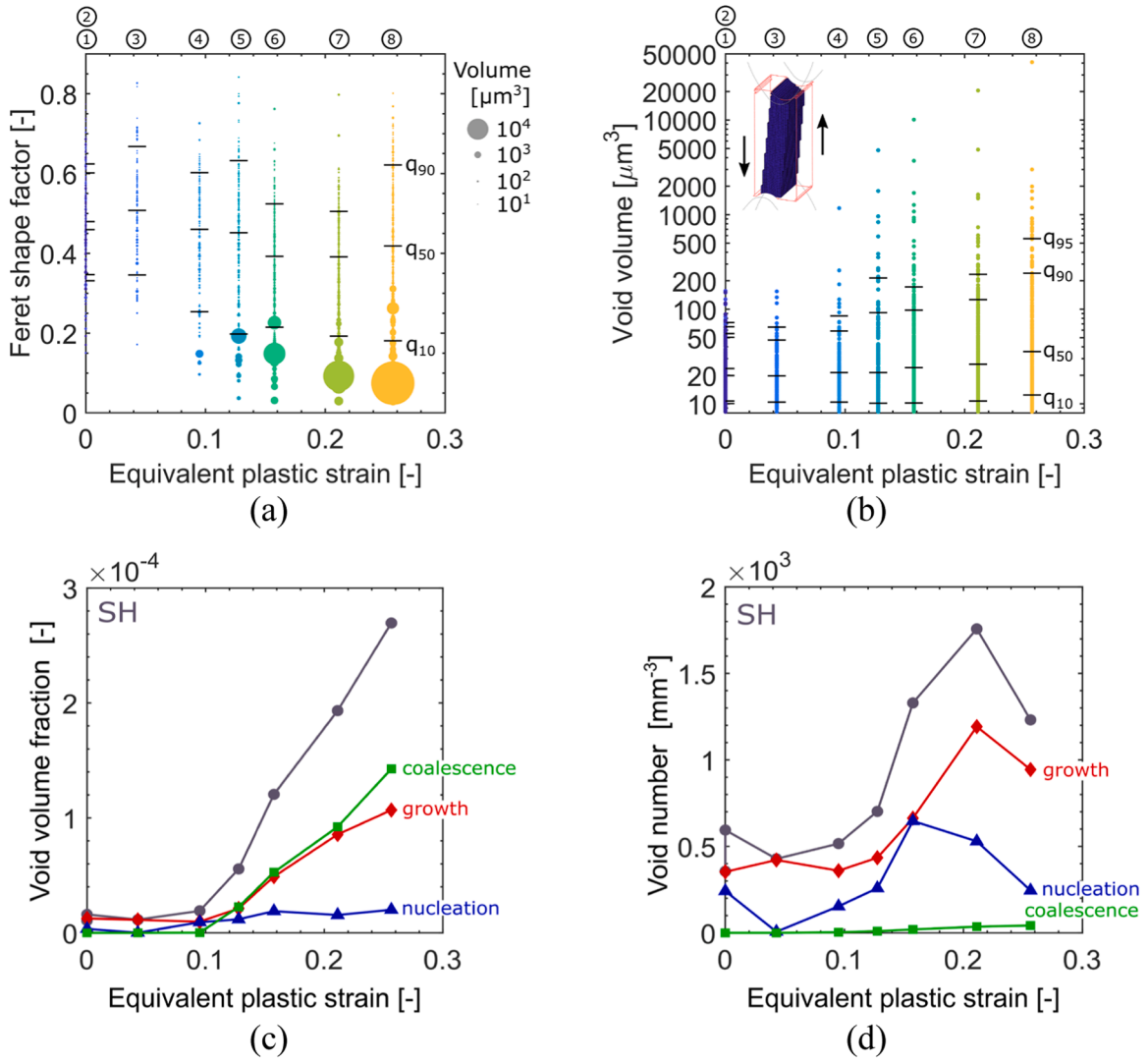

Fig. 10. Void population analysis of the SH experiment. Evolution of the (a) Feret shape factor, (b) void volume, (c) void volume fraction and (d) the void number per mm^3. The corresponding quantiles are denoted by horizontal black lines. The disc area in (a) scales linearly with the void volume. The total values in (c) and (d) are given in dark grey, while the fractions for nucleation, growth and coalescence are given in blue, red and green, respectively. Note the very low equivalent plastic strain increase between steps ① and ②. (For interpretation of the references to colour in this figure legend, the reader is referred to the web version of this article.)

Table 3
Summary of the shear experiments along with void volume fraction and void number evolution for the SH region with a trackable volume of 0.306 mm^3.

Step	U [mm]	F [kN]	VVF total [-] x10^{-5}				Void number/ unit volume [1/mm^3]				Stress State [-]		
			Total	Nucl.	Growth	Coal.	Total	Nucl.	Growth	Coal.	Triax.	Lode	EQPS
①	0.009	0.119	1.07	–	–	–	356.0	–	–	–	0.05	0.18	0.00
②	0.049	0.529	1.60	0.35	1.25	0.00	594.4	241.7	352.7	0.0	0.04	0.18	0.00
③	0.123	0.924	1.14	0.01	1.13	0.00	427.9	6.5	421.3	0.0	0.04	0.05	0.04
④	0.164	0.970	1.91	0.93	0.97	0.01	516.1	153.5	359.3	3.3	0.06	0.07	0.10
⑤	0.19	0.993	5.56	1.18	2.12	2.26	702.2	258.0	434.4	9.8	0.07	0.07	0.13
⑥	0.21	0.996	12.00	1.89	4.89	5.27	1329.3	646.7	663.0	19.6	0.08	0.07	0.16
⑦	0.249	1.008	19.30	1.55	8.56	9.22	1757.2	529.1	1192.2	35.9	0.10	0.08	0.21
⑧	0.281	0.987	27.00	2.01	10.70	14.30	1231.3	245.0	943.9	42.5	0.11	0.09	0.26

shear experiment (black solid dots) along with the corresponding in-situ laminography results (red crosses). The eight data points from in-situ measurements lie on top of the continuously recorded curve from the ex-situ experiment, underlining the good repeatability of the experiments. The specimens show an initially linear response, which is followed by a distinct yield point and a moderate hardening response. A force maximum of 1.02*kN* is reached at a displacement of 0.28*mm*, after which a minor drop in force is observed. This is followed by a short stagnation in force before complete fracture occurs at a displacement of 0.30*mm*. Detailed experimental results including reconstructed gray scale images, detailed void shape analyses and fractography images are given in Appendix B.

The FE-predicted force-displacement curve of the SH-specimen coincides with a <0.4 % difference almost up to final fracture with the experiment (black solid line, Fig. 7a). From step ⑧ onwards, the simulation overestimates the experiment by about 2.5 %, which is potentially

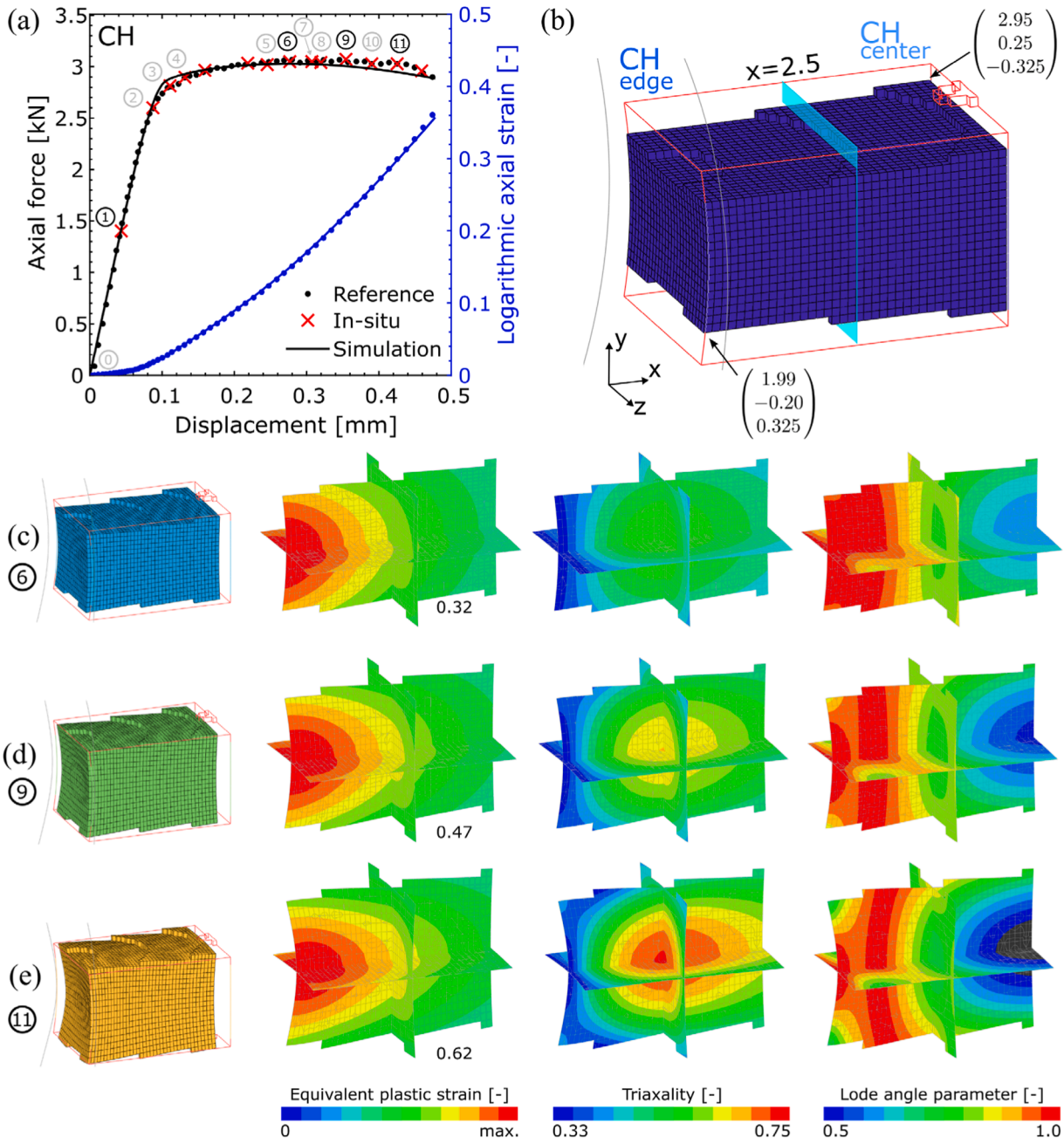

Fig. 11. Results from the numerical simulation of the CH specimen: Force-displacement curve of the reference (black dots) and the in-situ (red crosses) experiments along with the numerical simulation (solid black line). Local axial strain measurements are shown in blue. (b) Observable (red frame) and trackable volume (FE mesh). (c)-(e) Evolution of the equivalent plastic strain, the stress triaxiality and the Lode angle parameter for selected steps. Note that the three orthogonal planes in c-e correspond to $x = 2.5$ mm, $y = 0$ mm and $z = 0$mm. (For interpretation of the references to colour in this figure legend, the reader is referred to the web version of this article.)

attributed to the formation of crack-like void clusters (Fig. 9).

4.1.1. Mechanical fields

The evolution of the equivalent plastic strain, the stress triaxiality and the Lode angle parameter for the trackable volume for the SH-specimen are shown in Fig. 7c-e for selected loading steps. Throughout the loading, the equivalent plastic strain is concentrated in a band of about 0.3 mm in width and in a slanted hourglass shape. The maxima at the upper and lower boundary of the volume differ from the section's center by <20 %, underlining the homogenous plastic deformation of the zone. A maximum equivalent plastic strain value of $\bar{\varepsilon}_p = 0.52$ is obtained for step ⑧. A slight evolution in the stress triaxiality is observed at the specimen center, increasing from $\eta = 0.05$ (step ④) to $\eta = 0.11$ (step ⑧), while a variation of about ± 0.07 is observed within the volume. The Lode angle parameter is uniform around a zero mean without significant variation along the vertical y- axis.

4.1.2. Void tracking

For the SH specimen, the global shear deformation of the volume in y-direction is readily observable in Figs. 8a,c in the untreated state (left columns), while the top view (Fig. 8b) reveals a predominant shift in the void field in the x-direction. After void tracking, the visible rigid body motion has completely vanished and all voids are successfully translated into the reference configuration. Besides the very large void appearing at

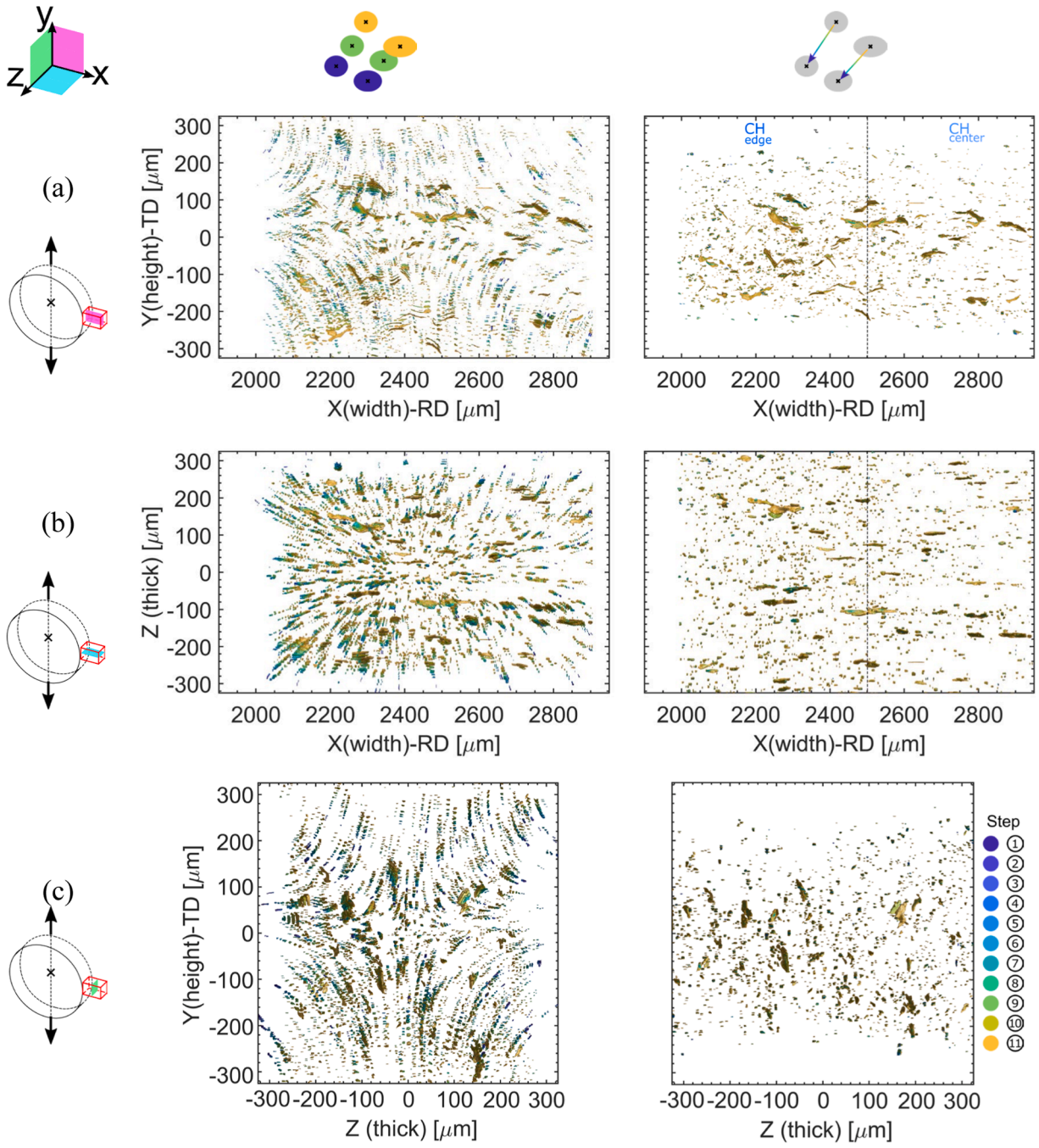

Fig. 12. Projected 3D views of the trackable volume of the CH volume (left column) before and (right column) after void tracking for the (a) xy-, (b) the xz- and (c) the yz-plane. Each void is colored according to the corresponding loading step, while the matrix is made transparent. Note the binning in CH-edge and CH-center at $x = 2500\mu$m and the evolution in the displacement field for the different loading steps (compare Fig. 11a), which is completely removed after the two-step translation and void tracking procedure.

$200\mu\text{m} < y < 400\mu\text{m}$, distinct void alignment bands are visible, for example at $z{=}{-}220\mu$m. It is speculated that these heterogeneities are the precursor sites for ductile failure.

Fig. 9 provides a close-up of the region around the largest void in the gage section. Several large voids ($V \geq 200\mu m^3$) nucleate towards step ④ at $z \approx -250\mu m$. Incipient coalescence is observed for these voids towards step ⑤, as several smaller voids nucleate and grow at $z \approx -110\mu m$. Through a series of coalescences along the y- (step ⑥&⑦) and z-direction (step ⑧), these voids form the largest void at the last step before failure with a volume of $V = 40853\mu m^3$. This is approximately 2000 times larger than its initial volume and contributes about 52 % of the total void volume of the region of interest. It is noteworthy that all coalescing voids lie in a narrow band of <50 μm thickness in the x-direction (RD).

4.1.3. *Quantitative void population analysis*

Figs. 10a,b show the evolution of the Feret shape factor and the volume for all voids along with selected quantiles (10th, 50th, 90th, 95th) against the average equivalent plastic strain from the trackable volume of the SH experiment. In Fig. 10a, the area of the marker disc is linearly related to the void volume. The evolution of the void volume fraction and the void number per cubic millimeter are shown in Fig. 10c, d. The total as well as the fractions attributed to nucleation (blue), growth (red) and coalescence (green) are shown.

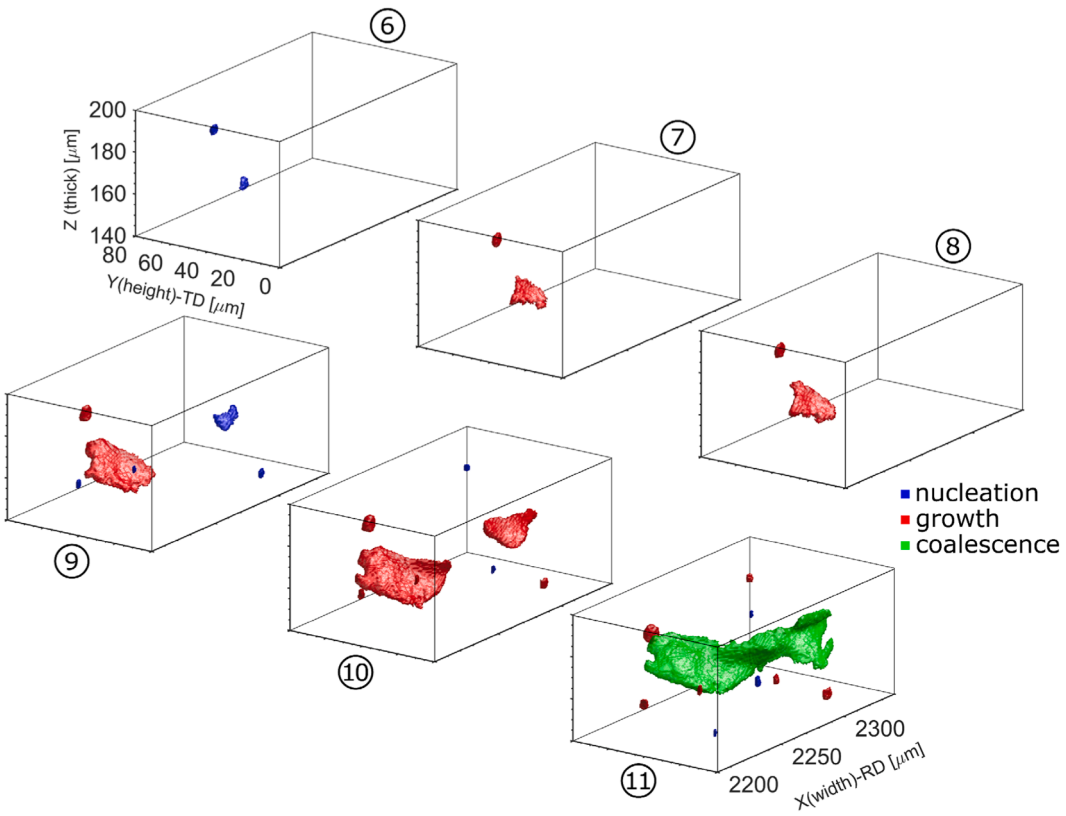

Fig. 13. Close-up view of a subregion of the CH-edge volume including the largest void for selected steps with mechanism labeling. Note the distinct growth and coalescence processes of individual voids forming one large void.

The majority of the observed initial porosity (109 voids) is of ellipsoidal shape with mean Feret shape factors around 0.48 and mean void volumes around $V \approx 20\mu m^3$(Fig. 10a,b). Up to a plastic strain of about 0.05, no significant change from the initial void volume, void volume fraction (1.07×10^{-5}) nor void number is observed, while the median Feret shape factor increases slightly to 0.51, i.e. the existing voids become more spherical. A first significantly larger and elongated void ($V = 1200\mu m^3, F = 0.15$) is observed at a plastic strain of 0.09. Hereafter, a noticeable drop in the Feret shape factors is seen as this void continues to grow and coalesce together with several other, severely elongated voids, eventually forming the largest void observed before the onset of failure. At the same time, the mean void volume only increases slightly to $V \approx 35\mu m^3$.

These observations are also supported by the global void volume fraction (Fig. 10c). A jump in the contribution of void volume fraction for coalescence to about 40 % is observed at an equivalent plastic strain of 0.09. It continues to constantly increase to >53 % at the last observable step, which corresponds to 1.4×10^{-4} of the 2.7×10^{-4} total in VVF. After the spike in nucleation around a plastic strain of 0.09, the percentage in VVF for nucleation decreases during the loading from 20 % to about 7 % in the last step. In a comparable manner, the number of growing voids per cubic millimeter increases from about $350mm^{-3}$ to about $1193mm^{-3}$ during the test (Fig. 10d). Nucleation follows a similar trend, however at less than half of the amount of growth, particularly during the early stages of loading. In stark contrast, the number of coalescing voids evolves at a low and constant rate and remains at <50 voids (per unit volume) for the last observable step. Together with the observation in VVF this indicates that a very small number of voids grow and coalesce to significant void volume fractions in this experiment. A summary of all measurements of the shear experiment is given in Table 3. Additional details on the evolution of the void shape are shown in Fig. B5.

It is noteworthy that for the last observed step, the number of voids per unit volume decreases by about 30 %. While this can partially be attributed to the effects of coalescence and void closure near the large micro-crack, it seems to also relate to segmentation limitations in this volume, effectively removing several smaller voids (compare Fig. 9y-z-plane, step ⑦ and ⑧).

4.2. Central hole tension experiments (uniaxial tension)

Fig. 11a presents the force-displacement curves from both in-situ and ex-situ experiments along with the local axial strain from a 1 mm long extensometer on the side of the central hole. After an initially linear response, a distinct yield point is observed at step ②, followed by a small force increase up to a maximum of 3.07 kN close to step ⑨. Final failure is observed about 0.2 mm later and 0.05 mm after the last evaluated imaging step ⑪. Additional details on the experiment are given in Appendix C.

The force-displacement curve obtained from the corresponding finite element simulation (solid line) deviates slightly from the experimental observations. An initial overshoot of 3.2 % is followed by a slight underestimation of the force level post force maximum. Good agreement of the simulations and experiments is observed when comparing the local strain evolution. It shows differences of <1 % (blue curves on secondary axis of Fig. 7a).

4.2.1. Mechanical fields

For the CH-specimen, the highest plastic strains are observed close to the central hole boundary of the trackable volume, with a pronounced gradient towards the CH-specimen center (Fig. 11c-e). For most steps, the equivalent plastic strain on the right boundary of the trackable volume is about 2.25 times lower than that on the free boundary. The Lode angle parameter decreases from $\bar{\theta} \approx 1$ at the free boundary to about 0.75 in the volume center throughout loading, however remaining close to a generalized tension stress state. In contrast, the stress

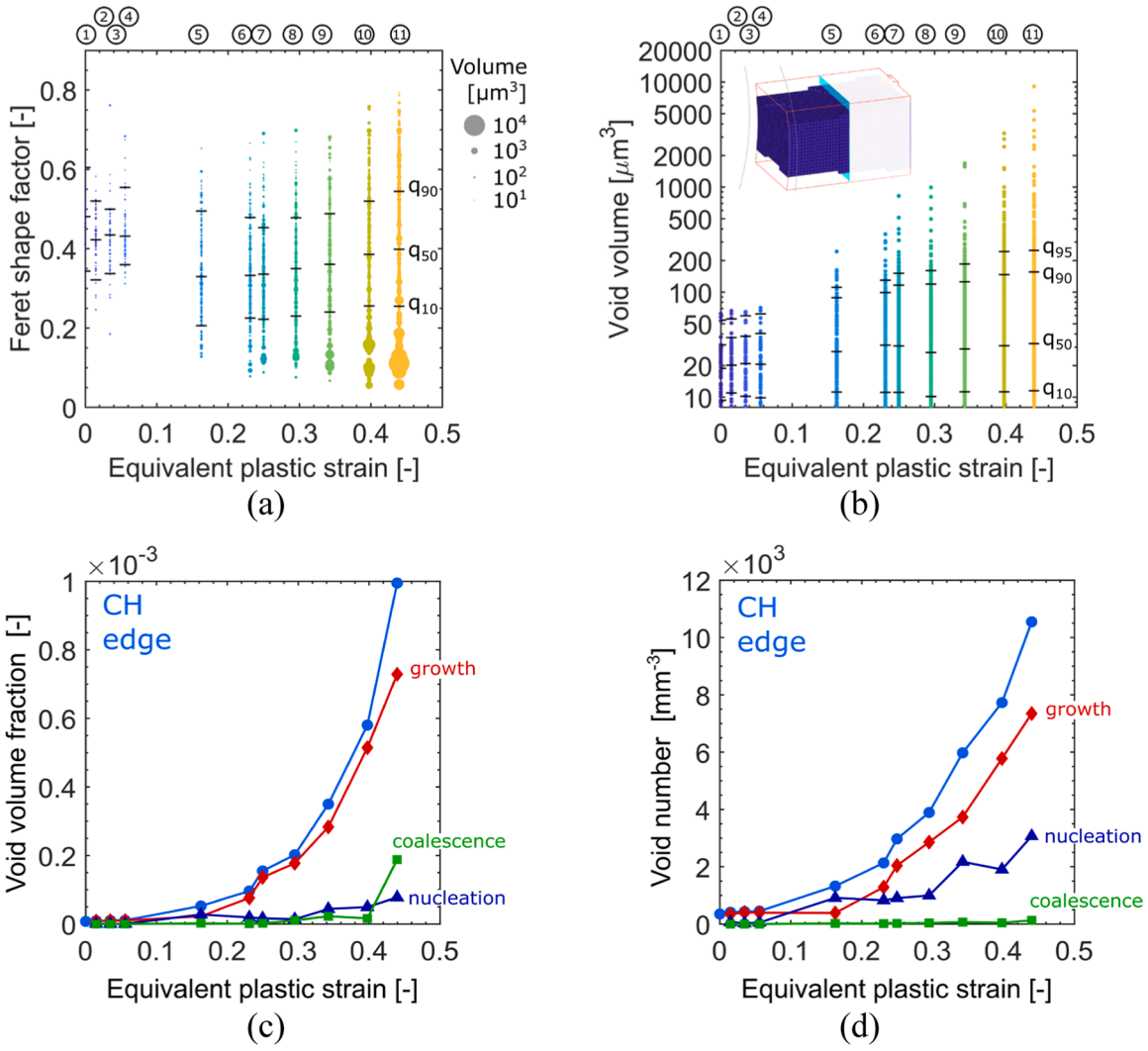

Fig. 14. Void population analysis of the CH-edge volume. Evolution of the (a) Feret shape factor, (b) void volume, (c) void volume fraction and (d) the void number per mm^3. The corresponding quantiles are denoted by horizontal black lines. The disc area in (a) scales linearly with the void volume. The total values in (c) and (d) are given in light blue, while the fractions for nucleation, growth and coalescence are given in blue, red and green, respectively. (For interpretation of the references to colour in this figure legend, the reader is referred to the web version of this article.)

triaxiality increases from uniaxial tension ($\eta = 0.33$) at the free boundary towards the center of the trackable volume. Driven by the onsetting necking behind the free edge, it increases at this location from $\eta = 0.52$ (Fig. 11c, ⑥) to about $\eta = 0.75$ (Fig. 11e, ⑪). Due to these high gradients in the mechanical fields, we divide the trackable volume into two smaller volumes (referred to as "CH-edge" and "CH-center", Fig. 11b) when analyzing the void evolution and reporting average quantities.

4.2.2. Void tracking

The projected views of the segmented CH volume are shown for all observed steps in Fig. 12. The superposition of the projections for all steps exposes the severe deformation of the trackable volume (left column). The observed symmetry is seen as an indicator of the good alignment of the coordinate frame and the strong effect of the mechanical fields on the damage evolution. The right column views are obtained after pulling back the voids in the reference configuration and subsequent void tracking. This process appears to be successful in the sense that there is no noticeable offset between the void patterns for different steps.

Fig. 13 shows a close-up view including the largest void within the entire volume. It is located within the CH-edge subregion. A first pair of newly-nucleated voids is observed in the plane $x \approx 2225\mu m$towards step ⑥. These voids grow until two more voids are nucleated in the plane $x \approx 2300\mu m$ towards step ⑨. After further growth, the coalescence of the voids is detected in step ⑪, resulting in a void volume of $V = 9082\mu m^3$. Based on the evolution in shape of these voids, it is speculated that the small voids originated from particles, while the larger platelet-shaped voids are related to both inter- and transgranular failure [40].

4.2.3. Quantitative void population analysis

Figs. 14a,b show the evolution of the void shape (Feret shape factor) and the void volume as a function of the equivalent plastic strain in the CH-edge subregion. At step ①, about 46 voids are observed with a maximum volume of $62\mu m^3$, a median Feret shape factor of 0.44 and a median volume of $21\mu m^3$. A significant drop in median Feret shape factor to 0.33 is observed at a plastic strain of about 0.16 followed by an increase towards a value of 0.4 at the last step. With increasing plastic loading (up to step ⑦), the median void volume increases to $30\mu m^3$, but stays almost constant throughout the remaining loading steps. In contrast, the 90th quantile of the void volume increases significantly for the same steps from $117\mu m^3$ to $156\mu m^3$, while the largest void grows from $824\mu m^3$ to more than $5000\mu m^3$ with a Feret shape factor below 0.2. The corresponding evolution for the CH center region is shown in

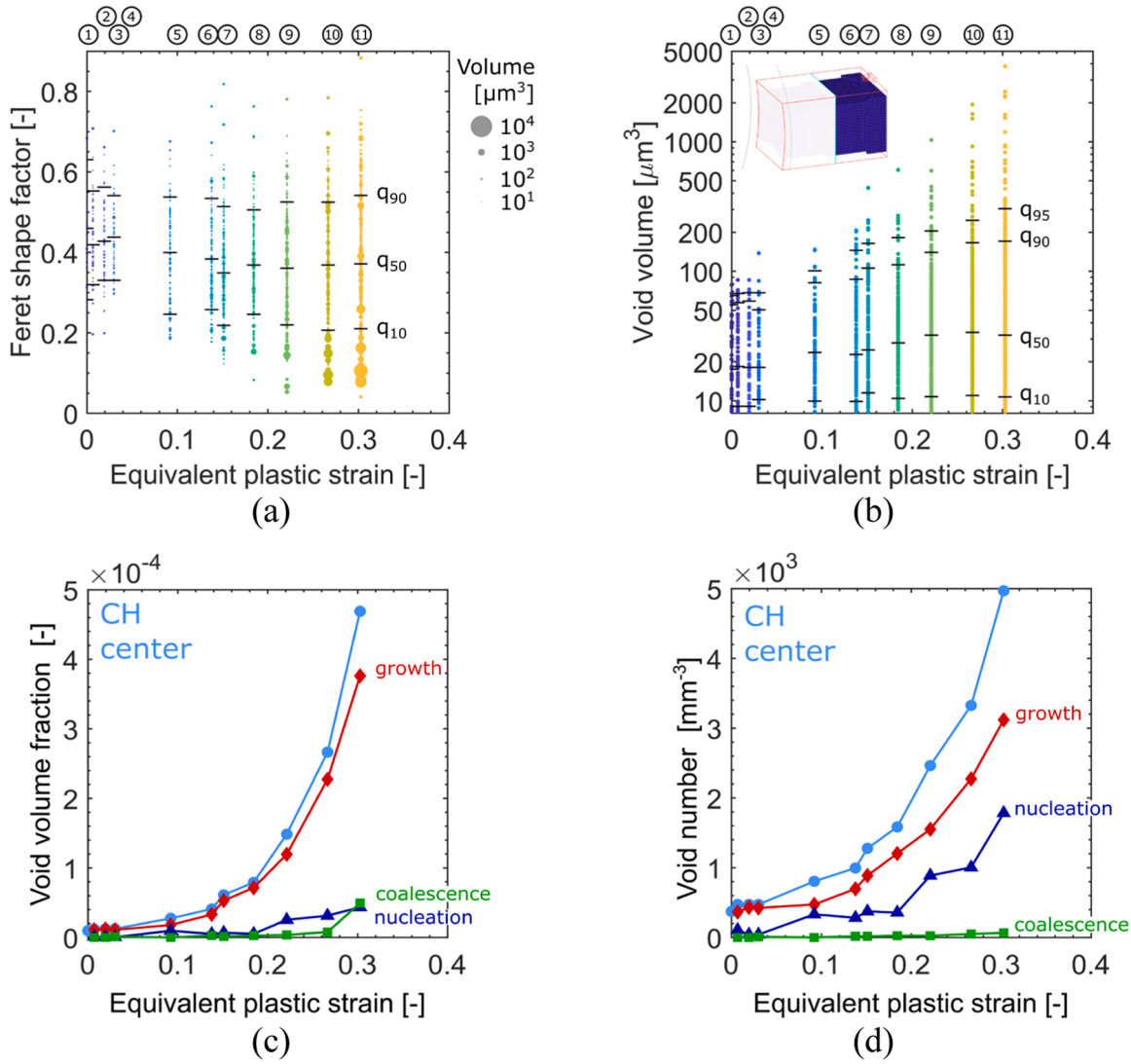

Fig. 15. Void population analysis of the CH-edge volume. Evolution of the (a) Feret shape factor, (b) void volume, (c) void volume fraction and (d) the void number per mm^3. The corresponding quantiles are denoted by horizontal black lines. The disc area in (a) scales linearly with the void volume. The total values in (c) and (d) are given in pale blue, while the fractions for nucleation, growth and coalescence are given in blue, red and green, respectively. (For interpretation of the references to colour in this figure legend, the reader is referred to the web version of this article.)

Table 4
Summary of the CH experiment along with void volume fraction and void number evolution for the CH-edge with a trackable volume of 0.131 mm^3.

Step	U [mm]	F [kN]	VVF total [-] x10^{-5}				Void number/ unit volume [1/mm^3]				Stress State [-]		
			Total	Nucl.	Growth	Coal.	Total	Nucl.	Growth	Coal.	Triax.	Lode	EQPS
①	0.04	1.403	0.76	–	–	–	350.6	–	–	–	0.38	0.84	0.00
②	0.09	2.601	0.95	0.08	0.09	0.00	411.6	68.6	343.0	0.0	0.42	0.84	0.01
③	0.11	2.814	1.04	0.04	1.00	0.00	434.4	30.5	403.9	0.0	0.42	0.87	0.03
④	0.13	2.897	1.08	0.06	1.01	0.00	449.7	53.4	396.3	0.0	0.42	0.89	0.06
⑤	0.25	3.020	5.27	2.78	2.25	0.24	1326.2	914.6	388.7	22.9	0.44	0.91	0.16
⑥	0.28	3.049	9.64	1.92	7.63	0.10	2134.1	830.8	1288.1	15.2	0.45	0.91	0.23
⑦	0.31	3.049	15.50	1.67	13.60	0.21	2972.4	907.0	2042.6	22.9	0.45	0.91	0.25
⑧	0.32	3.041	20.20	1.39	17.70	1.06	3894.7	998.4	2858.1	38.1	0.46	0.90	0.30
⑨	0.35	3.071	35.00	4.39	28.30	2.27	5975.4	2172.2	3734.6	68.6	0.47	0.90	0.34
⑩	0.39	3.028	58.10	4.95	51.50	1.64	7728.4	1905.4	5777.2	45.7	0.48	0.89	0.40
⑪	0.43	3.028	99.50	7.79	72.90	18.80	10,548.4	3071.5	7347.3	129.6	0.49	0.87	0.44

Fig. 15. Throughout the loading, comparable values for void shape and void volume are measured for all quantiles, with the exception of the largest void that does not grow above the 5000μm^3 mark.

The evolution for both void volume fraction as well as void number per cubic millimeter are shown for the CH edge region (Fig. 14c,d) and the CH center region (Fig. 15c,d). After no significant increase up to a strain of 0.06, the CH edge volume reaches a total VVF of 1.0 $\times$ 10^{-3} (Fig. 14c) at a plastic strain of 0.44, while the CH center reaches about half of that value (0.47 $\times$ 10^{-3}) at the last observable step at a strain of 0.3 (Fig. 15c). For both regions, void growth is the main contributing

Table 5
Summary of the CH experiment along with void volume fraction and void number evolution for the CH-center with a trackable volume of 0.121 mm^3.

Step	U [mm]	F [kN]	VVF total [-] x10^{-5}				Void number/ unit volume [1/mm^3]				Stress State [-]		
			Total	Nucl.	Growth	Coal.	Total	Nucl.	Growth	Coal.	Triax.	Lode	EQPS
①	0.04	1.403	0.97	–	–	–	373.3	–	–	–	0.42	0.69	0.00
②	0.09	2.601	1.21	0.12	1.09	0.00	472.9	107.9	365.1	0.0	0.47	0.61	0.01
③	0.11	2.814	1.24	0.05	1.19	0.00	472.9	41.5	431.4	0.0	0.46	0.61	0.02
④	0.13	2.897	1.25	0.04	1.09	0.11	472.9	41.5	423.1	8.3	0.44	0.64	0.03
⑤	0.25	3.020	2.75	0.96	1.79	0.00	804.8	331.9	472.9	0.0	0.46	0.69	0.09
⑥	0.28	3.049	4.09	0.50	3.31	0.28	995.6	282.1	696.9	16.6	0.48	0.69	0.14
⑦	0.31	3.049	6.12	0.67	5.31	0.14	1277.7	373.3	887.7	16.6	0.49	0.69	0.15
⑧	0.32	3.041	7.92	0.51	7.14	0.27	1584.7	356.8	1203.0	24.9	0.51	0.69	0.18
⑨	0.35	3.071	14.90	2.54	12.00	0.36	2464.1	887.7	1551.5	24.9	0.53	0.68	0.22
⑩	0.39	3.028	26.60	3.13	22.70	0.78	3326.9	1003.9	2273.3	49.8	0.55	0.66	0.27
⑪	0.43	3.028	46.90	4.34	37.60	4.95	4969.7	1783.8	3119.5	66.4	0.56	0.65	0.30

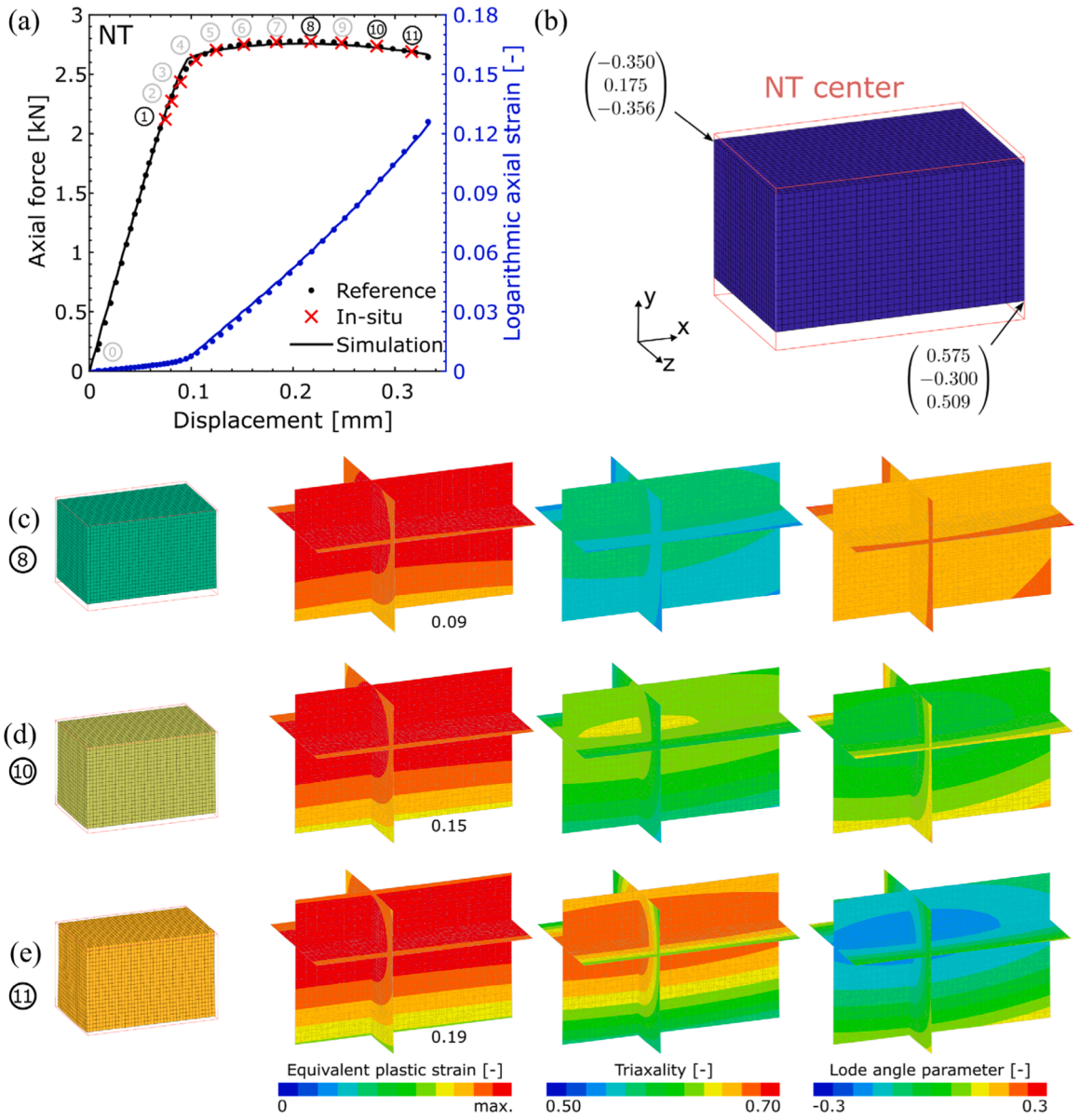

Fig. 16. Results from the numerical simulation of the NT specimen: (a) Force-displacement curve of the reference (black dots) and the in-situ (red crosses) experiments along with the numerical simulation (solid black line). Local axial strain measurements are shown in blue. (b) Observable (red frame) and trackable volume (FE mesh) for the NT center. (c)-(e) Evolution of the equivalent plastic strain, the stress triaxiality and the Lode angle parameter for selected steps. Note that the three orthogonal planes in c-e correspond to $x = 0$ mm, $y = 0$ mm and $z = 0$mm. (For interpretation of the references to colour in this figure legend, the reader is referred to the web version of this article.)

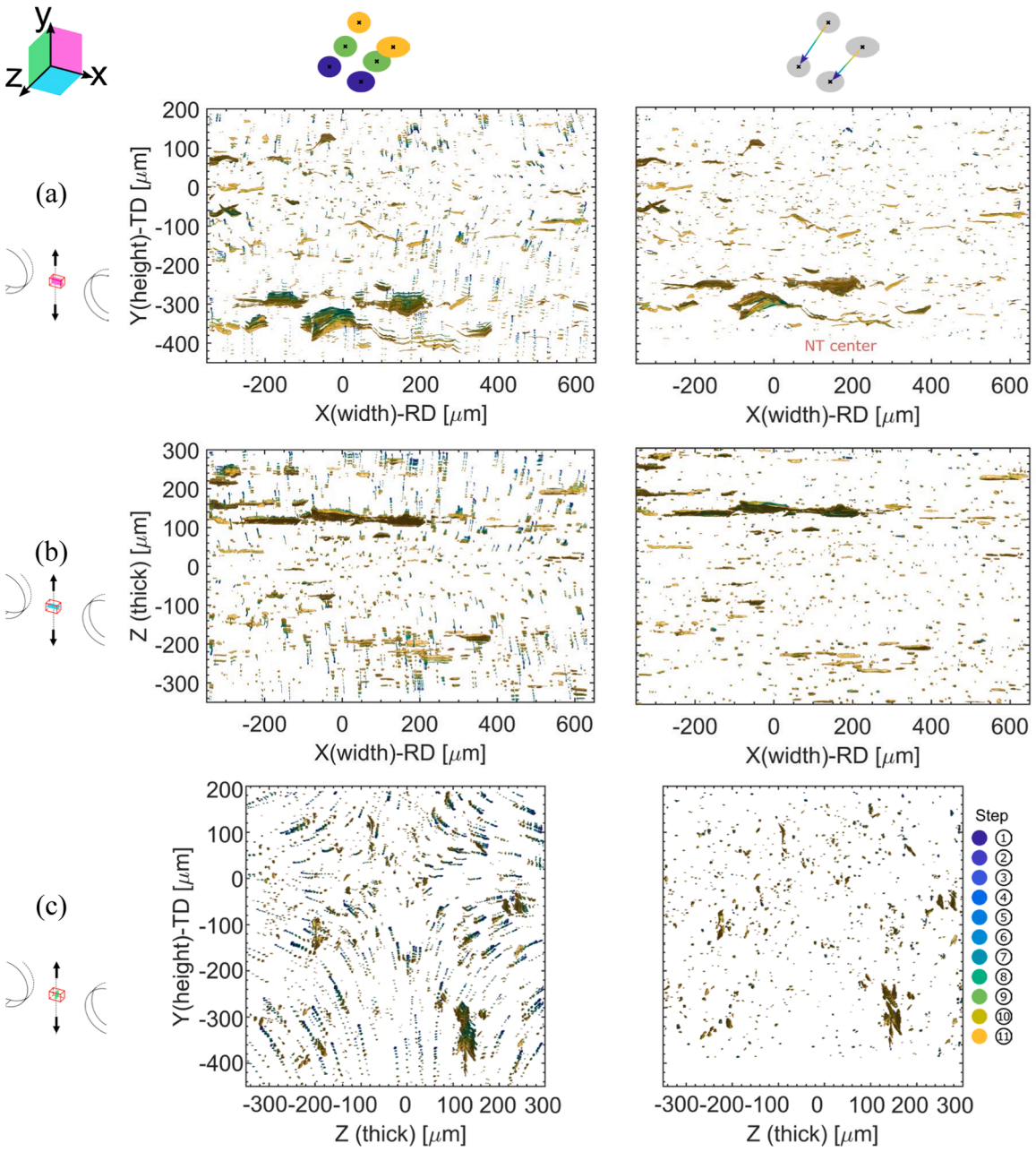

Fig. 17. Projected 3D views of the trackable volume of the NT-center volume (left column) before and (right column) after void tracking for the (a) xy-, (b) the xz- and (c) the yz-plane. Each void is colored according to the corresponding loading step, while the matrix is made transparent. Note the evolution in the displacement field for the different loading steps (compare Fig. 16a), which is completely removed after the two-step translation and void tracking procedure.

factor with >80 % up to the second last step (Fig. 14& 15c). Only in this last observable step does the VVF in coalescence starkly increase and contributes to about 20 % of the total VVF for the CH edge and 10 % for the CH center. When looking at the void number per cubic millimeter (Fig. 14& 15d), void growth is still the main fraction with up to 7.3 × 10^3 mm^{-3} of the overall 10.5 × 10^3 mm^{-3} voids in the CH edge region. However, the number of nucleated voids in the last step (3.1 × 10^3 mm^{-3}) significantly exceeds the number of coalescing voids (0.1 × 10^3 mm^{-3}).

The almost constant median volume along with the significant increase in void number points towards a strong nucleation of (smaller) voids, which is further supported by a slightly increasing median Feret shape factor. Overall, the failure mechanism of the central hole specimen is driven by significant growth of a small number of voids along with significant nucleation of smaller voids. A summary of all measurements is given in Table 3 and 4 for the CH-edge and CH-center regions. Additional details on the evolution of the void shape are shown in Fig. C5 and Table 5.

4.3. Notched tension experiment (plane strain and uniaxial tension)

For the notched tension (NT) specimen, two separate regions of interest denoted NT-center and NT-notch are observed for each of the eleven in–situ loading steps (Fig. 2e). Fig. 16a shows the corresponding force-displacement response of the macroscopic NT-experiment (black solid dots) along with the laminography results (red crosses) and the evolution of the local axial strain from a 1 mm long centrally positioned virtual extensometer. The force-displacement curve seems to leave the linear regime at step ①, followed by a monotonic hardening up to a force maximum (2.76 kN, step ⑧) and a necking-induced reduction in

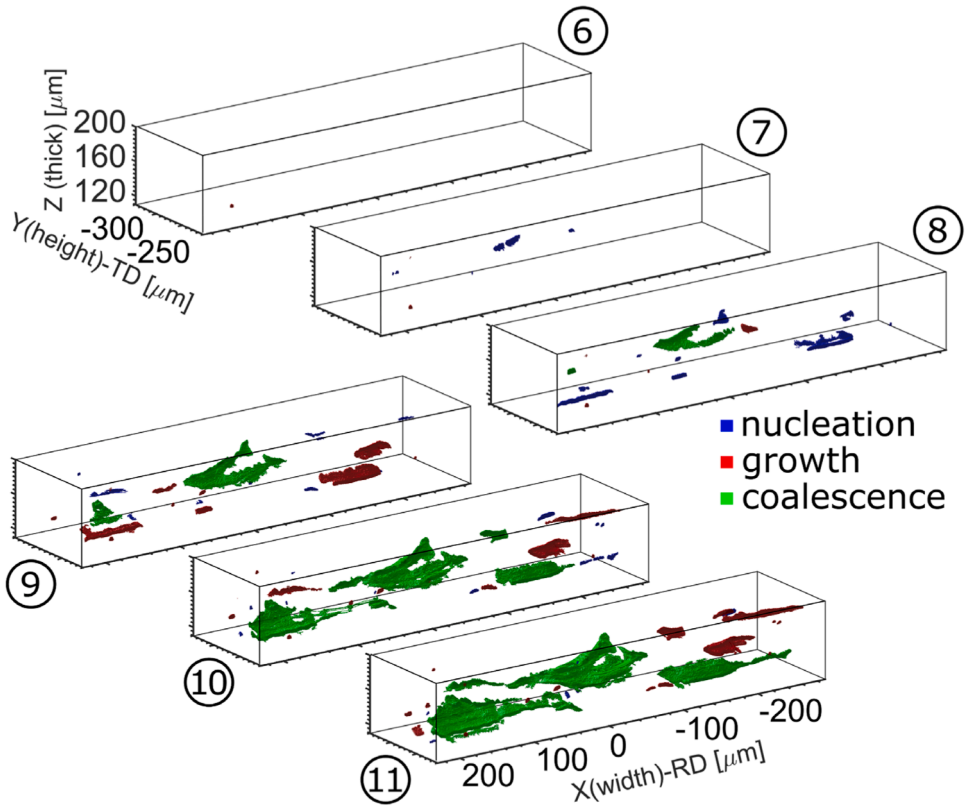

Fig. 18. Close-up view of a subregion of the NT-center volume including the largest void for selected steps with mechanism labeling.

load carrying capacity; final fracture is attained at a displacement of 0.33 mm and 2 .66kN. Both the force-displacement response as well as the local strain measurements show good agreement between the numerical simulation (solid lines) and the experimental recordings for the NT-specimen.

4.3.1. *Mechanical fields*

According to our simulations, the NT-center region features the most uniform mechanical fields (Fig. 16d-e) of all volumes observed in this study. A slight variation in the equivalent plastic strain and the stress state is mainly due to the minor offset of the trackable volume away from the specimen center, as indicated by the coordinates of the corner points in Fig. 16b. This leads to a maximum variation of about 28 % in the equivalent plastic strain on the lower edge of the volume irrespective of the step. Due to necking, the stress state evolves from close to plane strain tension ($\eta = 0.57$ and $\overline{\theta} = 0.15$) at step ⑧ (Fig. 16c) to a more biaxial state ($\eta = 0.68$and $\overline{\theta} = -0.17$) at step ⑪ (Fig. 8e). However, within the trackable volume, the spatial average of the stress triaxiality does not vary by >15 %.

In contrast, the NT-notch region (Fig. 20) features more significant spatial variations in the stress state and the plastic deformation. Both the stress triaxiality and the Lode angle parameter gradually evolve from an uniaxial stress state at the free boundary towards plane strain tension ($\eta = 0.52$, $\overline{\theta} = 0.44$) on the inward facing side of the volume ($x = 1.65$ mm) at step ⑧ and biaxial tension ($\eta = 0.61$, $\overline{\theta} = 0.25$) at step ⑪. This gradient in stress state motivates the sub-division of the NT-notch region into "NT-notch/edge" and "NT-notch/center" volumes at approximately half of the volume width ($x = 2.05$ mm, red plane, Fig. 20b).

4.3.2. *Void tracking*

The projected 3D views of the segmented volume of both the NT-center and NT-notch regions are given in Figs. 17 and 21, respectively. After void tracking (right columns in Figs. 17 and 21), no clear patterns are present in the projected 3D views, irrespective of the projection plane. A slight misalignment of the observed region of interest from the specimen's symmetry planes is visible in the untreated displacement field in Figs. 17c and 21c. Further, it is remarkable that the two volumes of the NT-notch show distinct and already visually observable differences in the void size and number.

A close-up of a subregion of the NT-center is shown in Fig. 18. A first nucleation is observed at $x \approx 180\mu m$ towards step ⑥ and at $x \approx 0\mu m$towards step ⑦. Already towards step ⑧, a large coalescence occurs at this location, along with further nucleation of elongated voids at $x \approx -150\mu m$ and $x \approx 200\mu m$. Over the course of the loading, these newly formed voids grow further and coalesce into an approximately $400\mu m$ long micro-crack. The corresponding subregion of the NT notch shows a similar evolution (Fig. 22). Several smaller voids nucleate and grow towards steps ⑥ and ⑦, while two larger and elongated voids are nucleated towards step ⑧. Aside from further nucleation and growth of smaller voids, it is the coalescence of these two voids that results in an approximately $380\mu m$ long micro-crack of volume $V = 137318\mu m^3$ in the last observable step.

4.3.3. *Quantitative void population analysis*

The evolution of the void shape, the void volume, as well as the void volume fraction and the void number per unit volume for the NT-center region is shown in Fig. 19. A total for 211 voids is initially observed with a VVF of 1.64×10^{-5}, a mean void volume of $20\mu m^3$ and a median Feret shape factor of 0.42. Up to an equivalent plastic strain of 0.06, almost no change in either of the quantities is observed, only the void volume reveals that three voids larger than $100\mu m^3$ exist. Distinct changes are already observed at the next step, for a plastic strain of about 0.08. Two voids exceed the $1000\mu m^3$ mark with a very low Feret shape factor of <0.1. It is noteworthy that coalescence already begins to play a significant role at this early stage, contributing about 28 % to the VVF in step ⑨. During the following loading steps, the voids continue to grow exponentially, resulting in four highly elongated voids (Feret shape

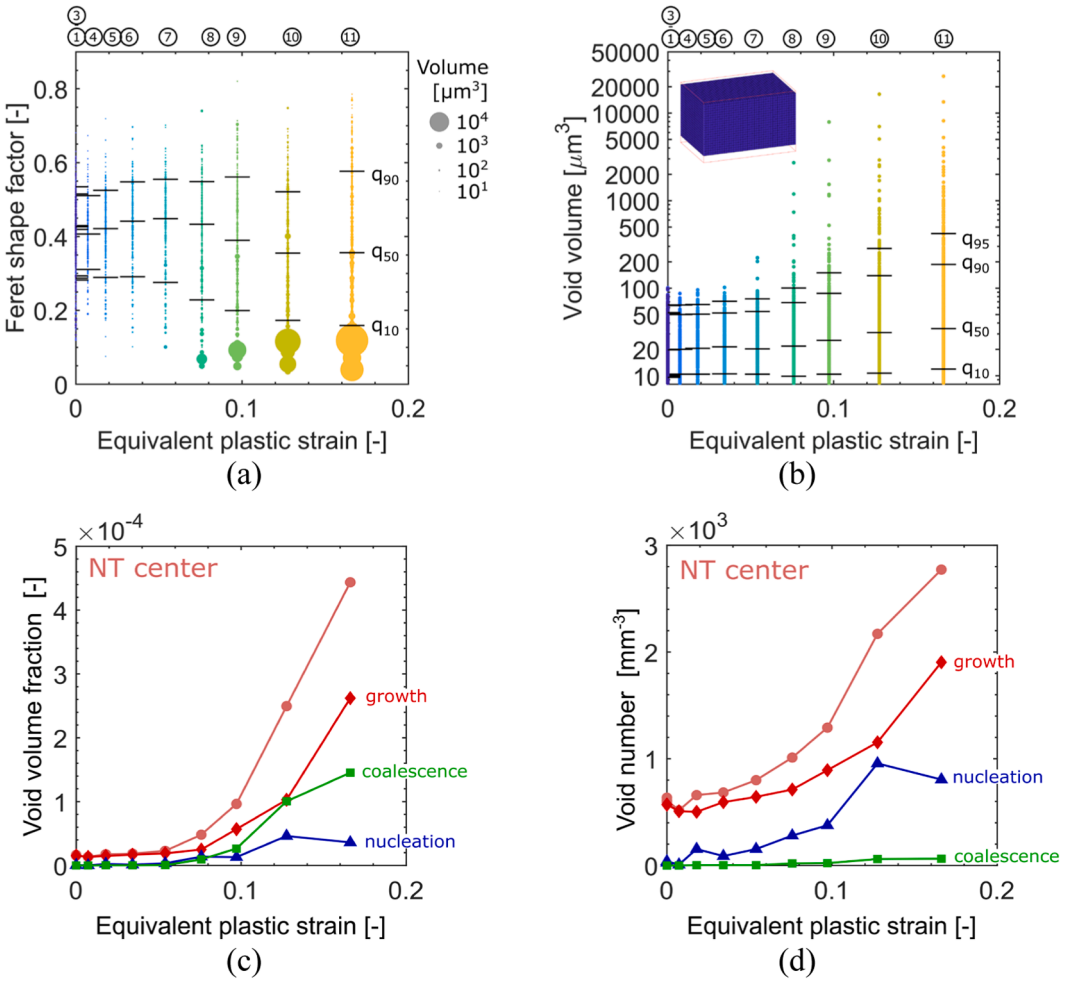

Fig. 19. Void population analysis of the NT-center volume. Evolution of the (a) Feret shape factor, (b) void volume, (c) void volume fraction and (d) the void number per mm^3. The corresponding quantiles are denoted by horizontal black lines. The disc area in (a) scales linearly with the void volume. The total values in (c) and (d) are given in pale pink, while the fractions for nucleation, growth and coalescence are given in blue, red and green, respectively. (For interpretation of the references to colour in this figure legend, the reader is referred to the web version of this article.)

factor below 0.2) exceeding a volume of 5000μm^3 at the maximum equivalent plastic strain of 0.17. From the force maximum at step ⑧ to this final observable step ⑪, the volume of the largest void has increased by almost 10 times (from 2711μm^3 at force maximum to 26319μm^3). For the last step, a VVF of 4.44 $\times$ 10^{-4} is measured to which nucleation, growth and coalescence contribute with about 8 %, 59 % and 33 % respectively. However, when looking at the void number per mm^3, the number of coalescing voids remains very low (below 2 %), as the percentage in number of nucleating voids increases from about 20 % to about 40 %, while the percentage in number of growing voids decreases accordingly throughout the loading. Overall, 1009 voids with a median volume of 33μm^3 are observed for the last step. All measurements for the NT-center region are given in Table 6.

The evolution of the quantities for the NT-notch/edge and NT-notch/center are shown in Figs. 23 and 24, respectively. Both regions feature initial values similar to the NT-center region. For the NT-notch/edge, at an equivalent plastic strain of about 0.09 (step ⑧), an initial increase in void volume is observed along with a minor decrease in the Feret shape factor. While growing exponentially, only four voids grow to a volume of more than 200μm^3 in the last step, out of which only the largest reaches more than 1000μm^3. For the NT-notch/center sub-region, a significant drop in Feret shape factor along with a noticeable increase in void volume occurs at an equivalent plastic strain of about 0.08. At this early stage, the largest void already exceeds 1000μm^3, while at the end of the loading five voids exceed this value. However, the largest void has grown to 137318μm^3 at step ⑪, about 115x more than at the force maximum (step ⑧). For both regions, a slow but constant increase in the median void volume to 35μm^3 at the end of the loading is observed. At the same time nucleation remains low for both volumes, first observed at plastic strain levels above 0.06 and remaining at a VVF below 4 $\times$ 10^{-5}. The number in nucleated voids per mm^3 increases at a constant rate to 398mm^{-3} for the NT-notch/edge region, and to 1035 mm^{-3} for the NT-notch/center region. For both regions, the VVF for growth follows a similar trend, culminating to 6.77 $\times$ 10^{-4} for the NT-notch/edge and 1.94 $\times$ 10^{-4} for the NT- notch/center. However, the strong difference in total VVF of about one order of magnitude (8.15 $\times$ 10^{-4} vs. 124.7 $\times$ 10^{-4}) is mainly due to the difference in coalescence. For the NT-notch/edge region, almost no coalescence occurs during the loading, either in VVF or in the void number per mm^3. In contrast, for the NT-notch/center region, significant coalescence in VVF is observed at plastic strain levels as low as 0.11, for which it contributes about 64 % to the total. This number increases further to >80 % for the last observable step, making the mechanism the main contributor. However, it is only a very small number of voids per mm^3, that contributes to this volume change, increasing from 3 to 14 during the same time. A summary of all measurements for the NT-notch/edge and NT-notch/center are shown in Table 7 and 8. Additional details on the evolution of the void shape and volume are shown in Figs. D6 and D7.

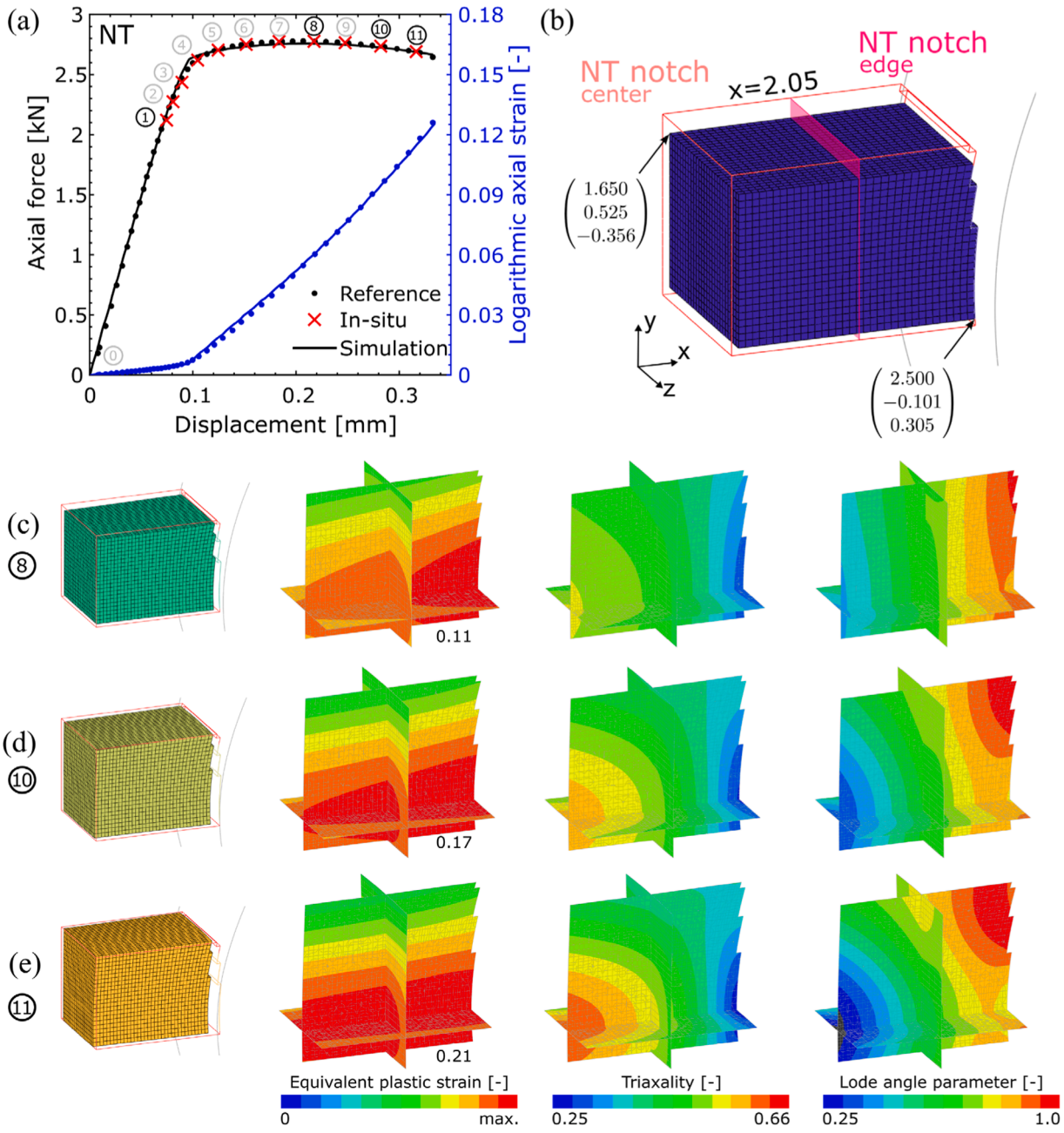

Fig. 20. Results from the numerical simulation of the NT specimen: Force-displacement curve of the reference (black dots) and the in-situ (red crosses) experiments along with the numerical simulation (solid black line). Local axial strain measurements are shown in blue. (b) Observable (red box) and trackable volume (FE mesh) for the NT notch. (c)-(e) Evolution of the equivalent plastic strain, the stress triaxiality and the Lode angle parameter for selected steps. Note that the three orthogonal planes in c-e correspond to $x = 2.05$ mm (the binning), $y = 0$ mm and $z = 0$mm. (For interpretation of the references to colour in this figure legend, the reader is referred to the web version of this article.)

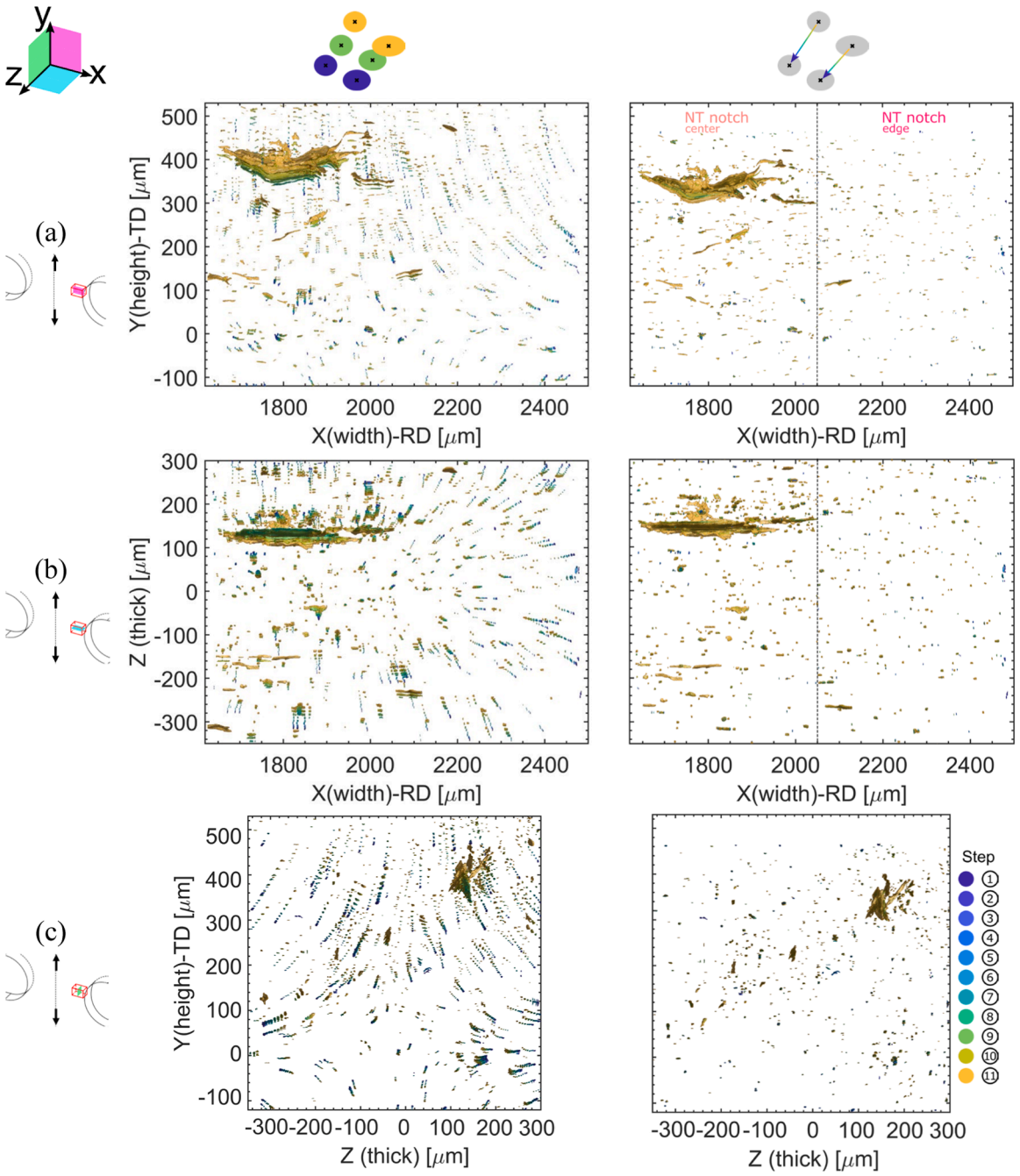

Fig. 21. Projected 3D views of the trackable volume of the NT-notch volume (left column) before and (right column) after void tracking for the (a) xy-, (b) the xz- and (c) the yz-plane. Each void is colored according to the corresponding loading step, while the matrix is made transparent. Note the binning in NT-notch/edge and NT-notch/center at $x = 2050\mu m$ and the evolution in the displacement field for the different loading steps (compare Fig. 20a), which is completely removed after the two-step translation and void tracking procedure.

Table 6
Summary of the NT experiment along with void volume fraction and void number evolution for the NT-center with a trackable volume of 0.364 mm^3.

Step	U [mm]	F [kN]	VVF total [-] x10^{-5}				Void number/ unit volume [1/mm^3]				Stress State [-]		
			Total	Nucl.	Growth	Coal.	Total	Nucl.	Growth	Coal.	Triax.	Lode	EQPS
①	0.075	2.120	1.64	–	–	–	634.6	–	–	–	0.56	0.10	0.00
②	0.081	2.273	1.54	0.03	1.51	0.00	593.4	24.7	568.7	0.0	0.56	0.09	0.00
③	0.089	2.436	1.58	0.05	1.54	0.00	609.9	38.5	571.4	0.0	0.57	0.08	0.00
④	0.105	2.619	1.35	0.02	1.34	0.00	516.5	8.2	508.2	0.0	0.56	0.13	0.01
⑤	0.124	2.703	1.75	0.24	1.49	0.03	659.3	153.8	502.7	2.7	0.55	0.17	0.02
⑥	0.152	2.750	1.84	0.13	1.69	0.02	684.1	87.9	593.4	2.7	0.55	0.20	0.03
⑦	0.184	2.773	2.29	0.34	1.89	0.06	799.5	153.8	642.9	2.7	0.55	0.21	0.05
⑧	0.217	2.776	4.82	1.37	2.49	0.1	1011.0	280.2	711.5	19.2	0.56	0.20	0.08
⑨	0.248	2.764	9.64	1.31	5.68	2.65	1291.2	376.4	892.9	22.0	0.57	0.15	0.10
⑩	0.282	2.736	25.00	4.61	10.30	10.00	2170.3	956.0	1153.8	60.4	0.60	0.08	0.13
⑪	0.316	2.691	44.40	3.61	26.20	14.50	2772.0	804.9	1903.8	63.2	0.63	−0.02	0.17

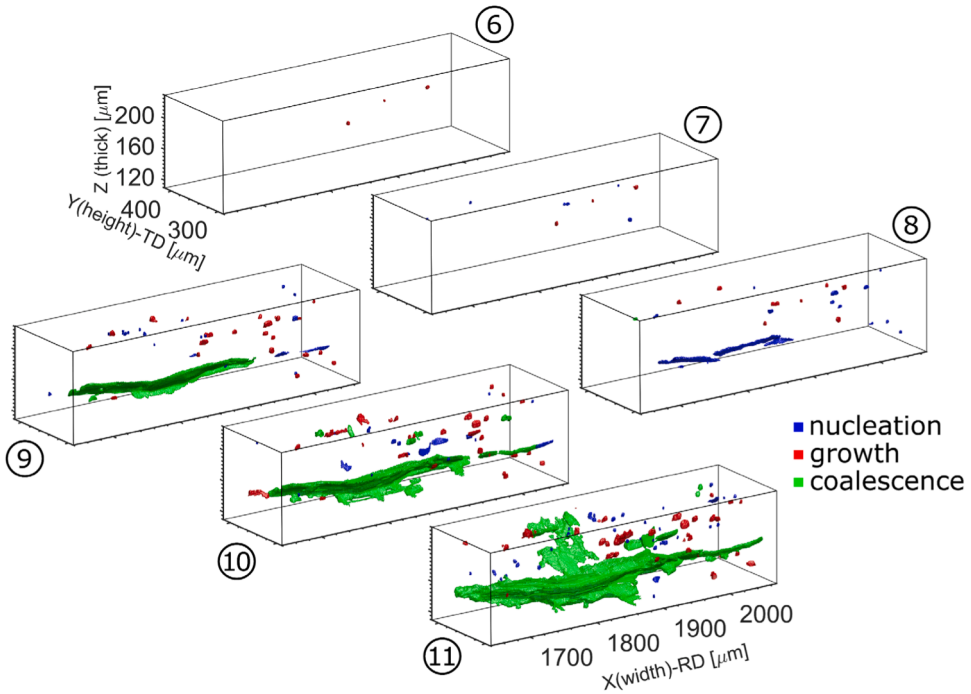

Fig. 22. Close-up view of a subregion of the NT-notch volume including the largest void for selected steps with mechanism labeling. Note the distinct growth and coalescence processes of individual voids forming one/several very long void(s).

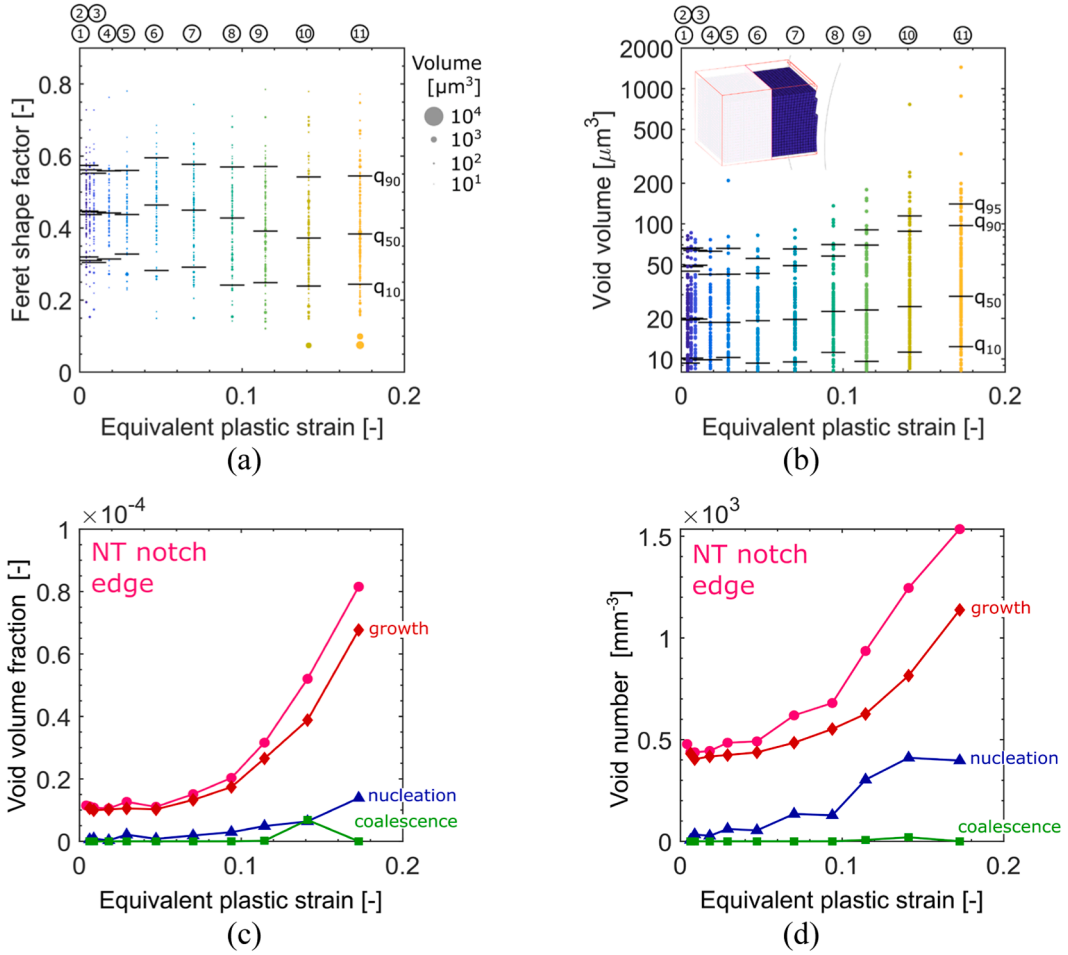

Fig. 23. Void population analysis of the NT-notch/edge volume. Evolution of the (a) Feret shape factor, (b) void volume, (c) void volume fraction and (d) the void number per mm^3. The corresponding quantiles are denoted by horizontal black lines. The disc area in (a) scales linearly with the void volume. The total values in (c) and (d) are given in raspberry, while the fractions for nucleation, growth and coalescence are given in blue, red and green, respectively. (For interpretation of the references to colour in this figure legend, the reader is referred to the web version of this article.)

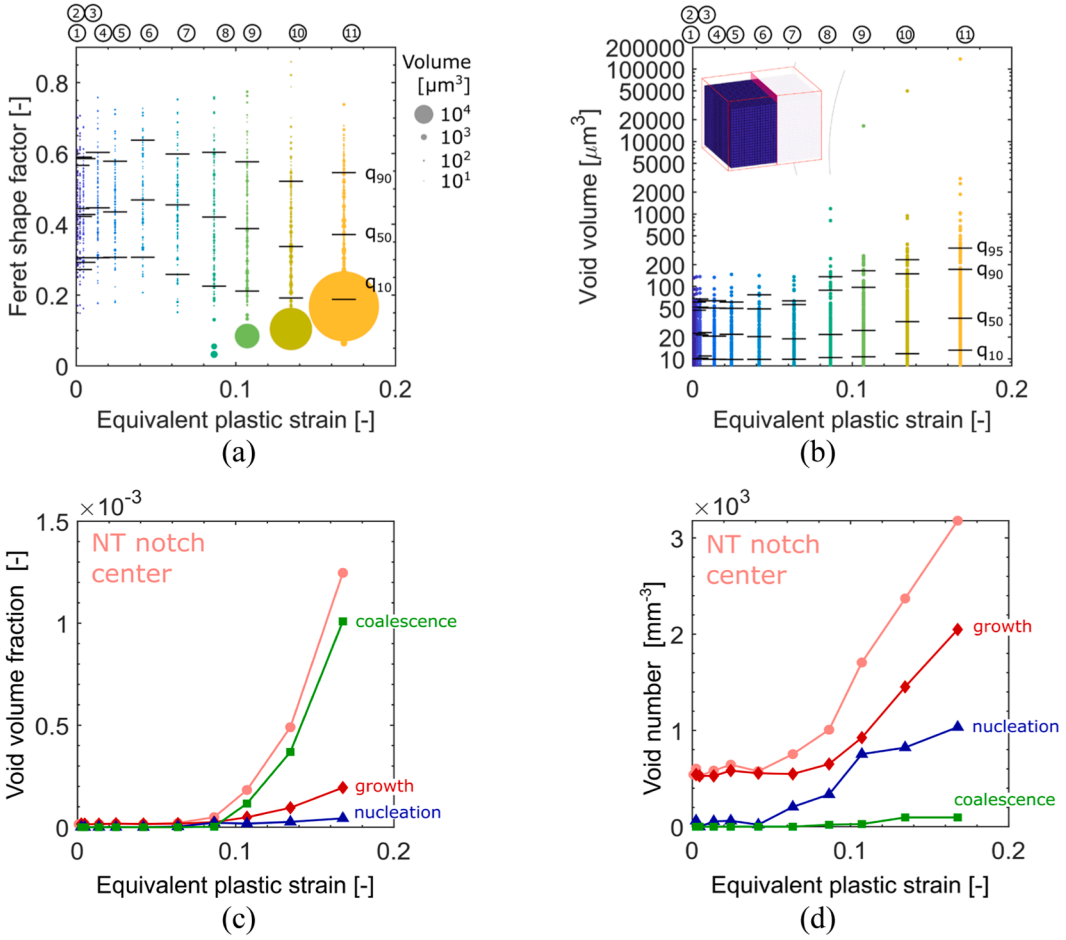

Fig. 24. Void population analysis of the NT-notch/center volume. Evolution of the (a) Feret shape factor, (b) void volume, (c) void volume fraction and (d) the void number per mm^3. The corresponding quantiles are denoted by horizontal black lines. The disc area in (a) scales linearly with the void volume. The total values in (c) and (d) are given in light pink, while the fractions for nucleation, growth and coalescence are given in blue, red and green, respectively. (For interpretation of the references to colour in this figure legend, the reader is referred to the web version of this article.)

Table 7
Summary of the NT experiment along with void volume fraction and void number evolution for the NT-notch/edge with a trackable volume of 0.149 mm^3.

Step	U [mm]	F [kN]	VVF total [-] x10^{-5}				Void number/ unit volume [1/mm^3]				Stress State [-]		
			Total	Nucl.	Growth	Coal.	Total	Nucl.	Growth	Coal.	Triax.	Lode	EQPS
①	0.075	2.120	1.15	–	–	–	478.0	–	–	–	0.39	0.86	0.00
②	0.081	2.273	1.12	0.06	1.06	0.00	437.6	6.7	430.9	0.0	0.39	0.85	0.01
③	0.089	2.436	1.08	0.09	0.99	0.00	437.6	33.7	404.0	0.0	0.39	0.84	0.01
④	0.105	2.619	1.05	0.03	1.02	0.00	444.4	26.9	417.4	0.0	0.38	0.81	0.02
⑤	0.124	2.703	1.26	0.21	1.05	0.00	484.8	60.6	424.2	0.0	0.38	0.81	0.03
⑥	0.152	2.750	1.10	0.08	1.02	0.00	491.5	53.9	437.6	0.0	0.38	0.82	0.05
⑦	0.184	2.773	1.51	0.19	1.33	0.00	619.4	134.7	484.8	0.0	0.39	0.83	0.07
⑧	0.217	2.776	2.03	0.29	1.74	0.00	680.0	127.9	552.1	0.0	0.39	0.83	0.09
⑨	0.248	2.764	3.16	0.49	2.65	0.02	935.9	303.0	626.1	6.7	0.39	0.83	0.11
⑩	0.282	2.736	5.20	0.64	3.88	0.68	1245.6	410.7	814.7	20.2	0.39	0.82	0.14
⑪	0.316	2.691	8.15	1.39	6.77	0.00	1535.1	397.2	1137.8	0.0	0.40	0.82	0.17

Table 8
Summary of the NT experiment along with void volume fraction and void number evolution for the NT-notch/center with a trackable volume of 0.146 mm^3.

Step	U [mm]	F [kN]	VVF total [-] x10^{-5}				Void number/ unit volume [1/mm^3]				Stress State [-]		
			Total	Nucl.	Growth	Coal.	Total	Nucl.	Growth	Coal.	Triax.	Lode	EQPS
①	0.075	2.120	1.47	–	–	–	541.3	–	–	–	0.45	0.58	0.00
②	0.081	2.273	1.69	0.10	1.59	0.00	602.9	61.7	541.3	0.0	0.46	0.59	0.00
③	0.089	2.436	1.48	0.00	1.48	0.00	527.6	0.0	527.6	0.0	0.46	0.58	0.00
④	0.105	2.619	1.58	0.07	1.51	0.00	582.4	54.8	527.6	0.0	0.47	0.55	0.01
⑤	0.124	2.703	1.78	0.07	1.71	0.00	644.0	61.7	582.4	0.0	0.47	0.56	0.02
⑥	0.152	2.750	1.58	0.03	1.55	0.00	575.5	20.6	555.0	0.0	0.47	0.57	0.04
⑦	0.184	2.773	2.06	0.32	1.74	0.00	753.7	205.5	548.1	0.0	0.47	0.58	0.06
⑧	0.217	2.776	4.92	2.21	2.46	0.25	1007.2	335.7	650.9	20.6	0.48	0.58	0.09
⑨	0.248	2.764	18.20	1.75	4.85	11.60	1706.0	753.7	925.0	27.4	0.49	0.57	0.11
⑩	0.282	2.736	49.10	2.60	9.53	36.90	2370.6	822.2	1452.5	95.9	0.50	0.55	0.13
⑪	0.316	2.691	124.7	4.34	19.40	100.9	3179.1	1034.6	2048.6	95.9	0.52	0.53	0.17

4.4. Experiments on compact tension specimens (biaxial tension stress states)

For the compact tension (CT) specimen no additional ex-situ experiment is performed; for this experiment only the notch opening displacement (NOD) curve from the in-situ experiment is available along with the results from the FE-simulation in Fig. 25a. Overall, five loading steps are recorded from initial loading to final fracture. The observable (red box) and trackable volume (blue FE mesh) used for the analysis are shown in Fig. 25b.

4.4.1. Mechanical fields

For the CT specimen (Fig. 25c-e), the spatial gradients in the stress triaxiality field are similar to those for the CH-specimen. However, significantly higher triaxiality values of around $\eta = 1$ are reached at the center of the CT volume, while the inward facing side ($x = 36.874$ mm) remains at about $\eta = 0.74$. The Lode angle parameter distribution remains almost unchanged throughout the loading, from $\overline{\theta} \approx 1$ on the free boundary and $\overline{\theta} \approx -0.45$ at the inward facing side. A Lode angle parameter of $\overline{\theta} \approx 0.4$ occurring at approximately half of the volume width is selected to sub-divide into "CT/edge" and "CT/center" volume ($x = 36.415$ mm, green plane, Fig. 10b). Most noticeable is the gradient in the equivalent plastic strain field. While very high strain values are reached on the free boundary, a rapid decrease to about 75 % is observed about 0.1 mm behind the free edge and 40 % at the volume center.

4.4.2. Void tracking

The projected views of the segmented CT volume (Fig. 26, left

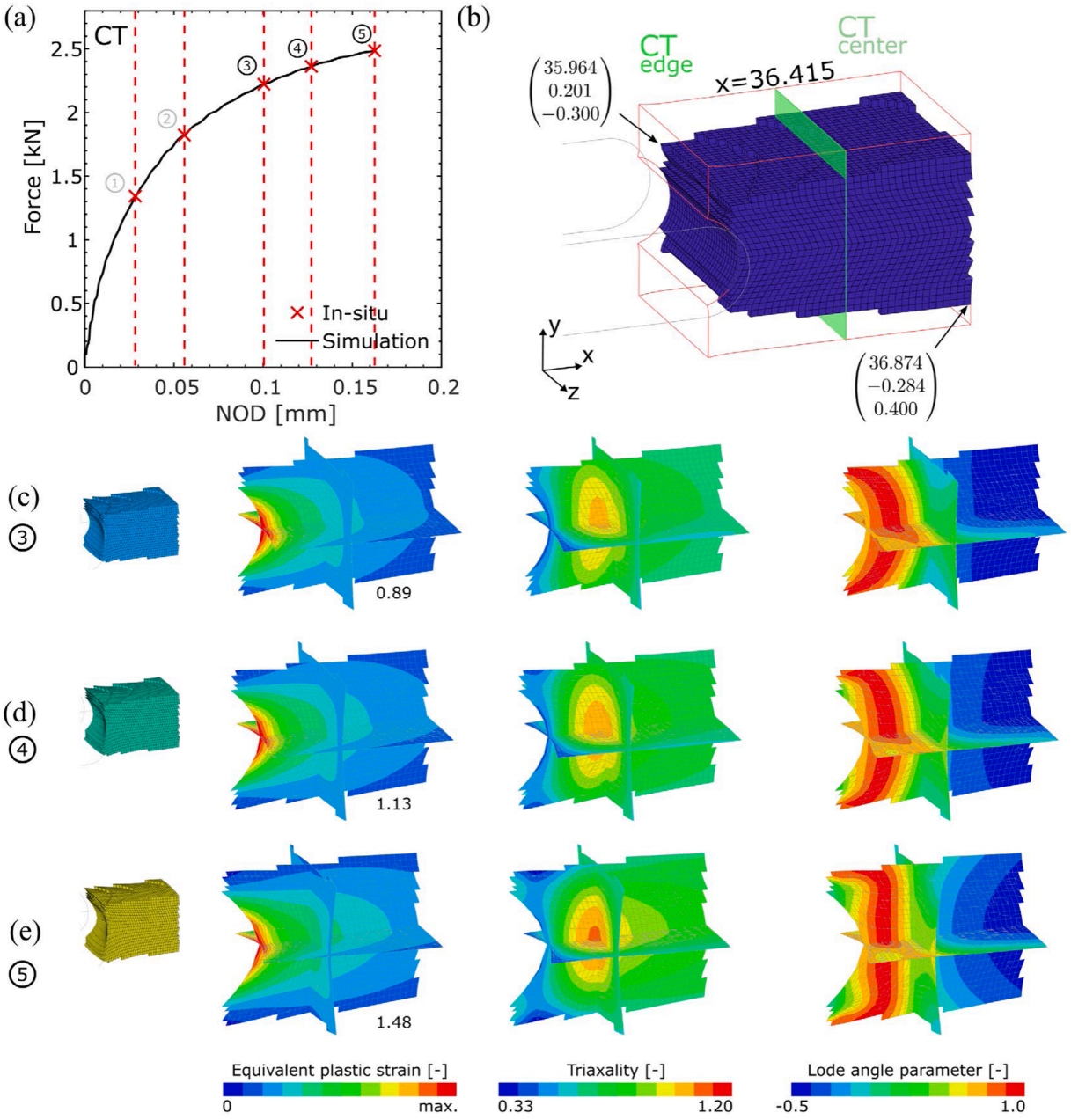

Fig. 25. Results for the CT specimen: (a) Notch opening displacement (NOD) of the in-situ (red lines) experiments along with the Force-NOD from the numerical simulation (solid black line). (b) Observable (red box) and trackable volume (FE mesh). (c)-(e) Evolution of the equivalent plastic strain, the stress triaxiality and the Lode angle parameter for selected steps. Note that the three orthogonal planes in c-e correspond to $x = 36.415$ mm, $y = 0$ mm and $z = 0$mm. (For interpretation of the references to colour in this figure legend, the reader is referred to the web version of this article.)

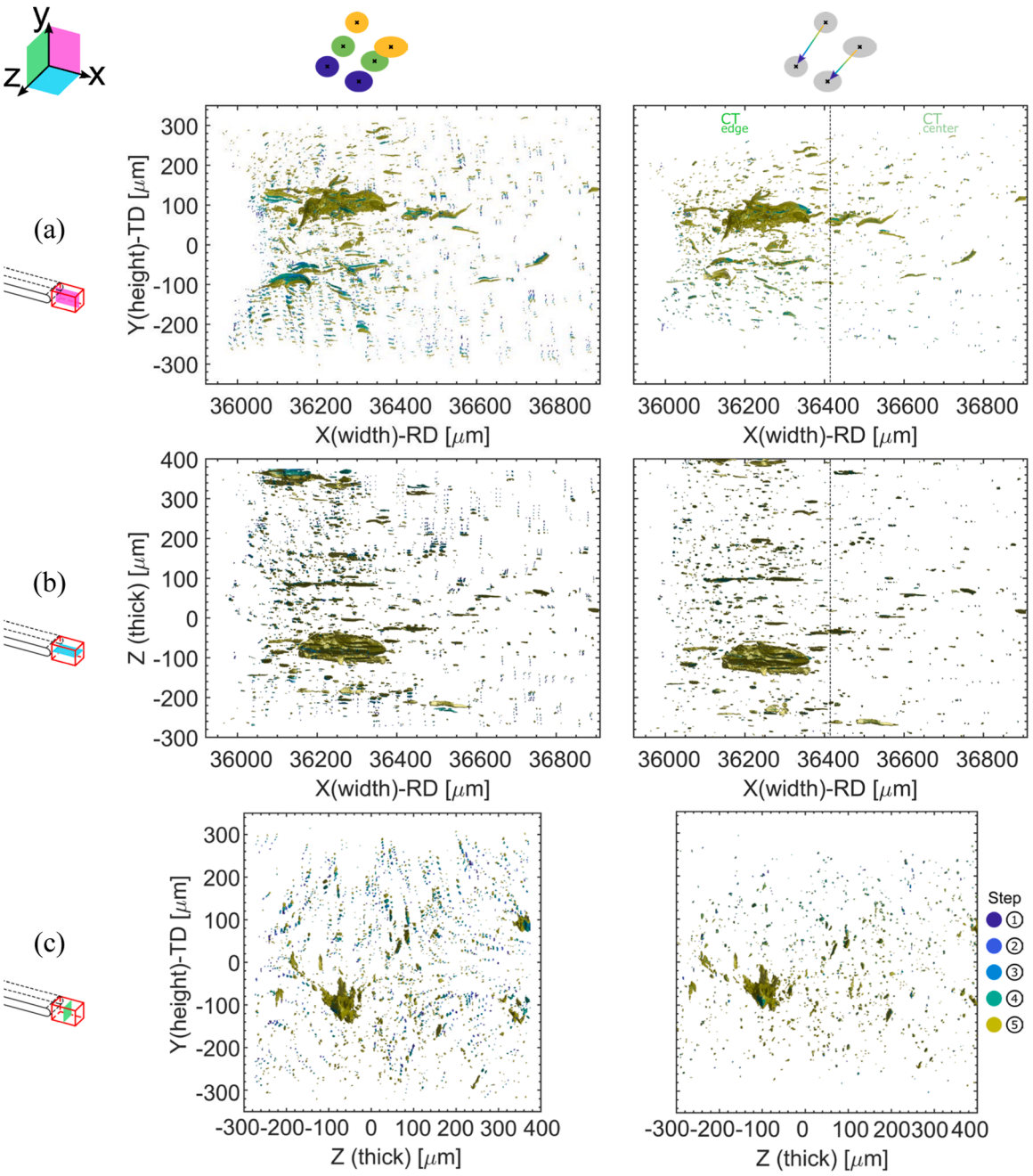

Fig. 26. Projected 3D views of the trackable volume of the CT (left column) before and (right column) after void tracking for the (a) xy-, (b) the xz- and (c) the yz-plane. Each void is colored according to the corresponding loading step, while the matrix is made transparent. Note the binning in CT-edge and CT-center at x = 36415μm and the evolution in the displacement field for the different loading steps (compare Fig. 25a), which is completely removed after the two-step translation and void tracking procedure.

column) and the corresponding plots after void tracking (Fig. 26 right column) are dominated by a very large void that forms right behind the notch at $x \approx 36{,}250\mu$m. The two chosen sub-volumes "CT/edge" and "CT/center" already reveal visually noticeable differences in void number and sizes. No traces of rigid body motions can be observed in the void field after void tracking. It is remarkable that tentative localization planes are visible in the backtracked plots of the Y-Z-plane for the CT regions near the largest voids. Fig. 27 shows a close-up of a subregion of the CT edge which contains the biggest void. Three platelet-shaped voids nucleate towards step ③ and begin to coalesce and grow significantly during further loading, forming a void of $V = 113808\mu m^3$. At the same time, additional elongated voids are nucleated and grow, but at a significantly lower rate than the biggest void.

4.4.3. *Quantitative void population analysis*

Figs. 28 and 29 show the evolution of the void shape, the void volume, the void volume fraction (VVF) and the void number per unit volume for the CT-edge and CT-center regions. An initial VVF of about 1.8×10^{-5} is observed for both regions with about 800 voids per mm^3 and a mean void volume of about $20\mu m^3$. The median Feret shape factor evolves from an initial value of about 0.54 to about 0.45 at the last observable step ⑤. At this step two voids exceed $5000\mu m^3$for the CT edge, the largest having grown to 113,808 μm^3 with a Feret shape factor of 0.24.

For the CT-edge (Fig. 28c), a VVF of 1.87×10^{-2} is obtained in the last step at a plastic strain of 0.47, which is approximately 200x higher than the 1.5×10^{-4} measured in the CT-center at a plastic strain of 0.3

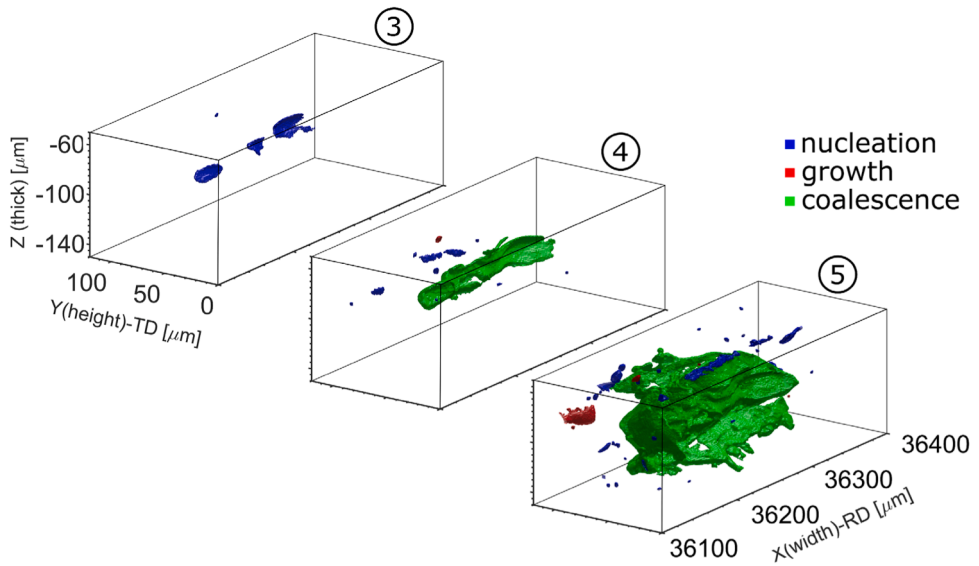

Fig. 27. Close-up view of a subregion of the CT volume including the largest void for selected steps with mechanism labeling.

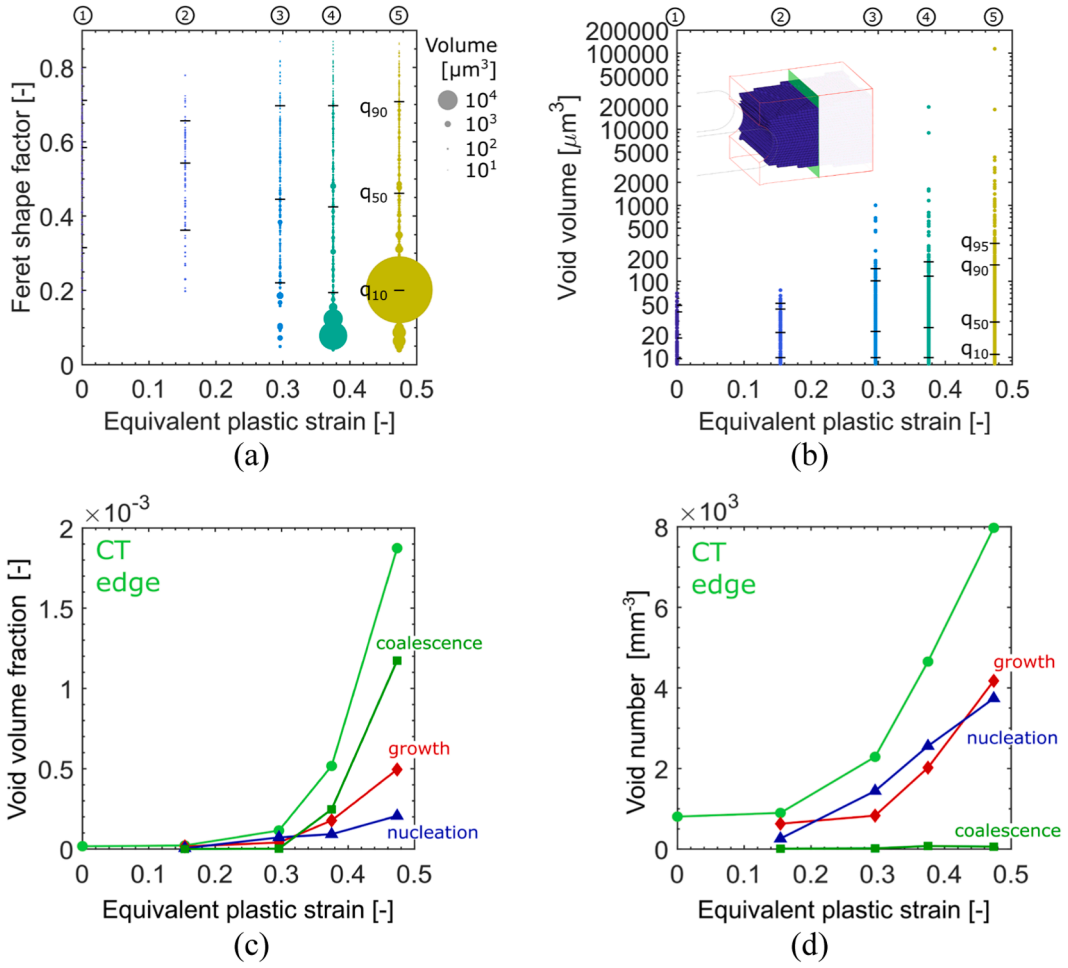

Fig. 28. Void population analysis of the CT-edge volume. Evolution of the (a) Feret shape factor, (b) void volume, (c) void volume fraction and (d) the void number per mm^3. The corresponding quantiles are denoted by horizontal black lines. The disc area in (a) scales linearly with the void volume. The total values in (c) and (d) are given in light green, while the fractions for nucleation, growth and coalescence are given in blue, red and green, respectively. (For interpretation of the references to colour in this figure legend, the reader is referred to the web version of this article.)

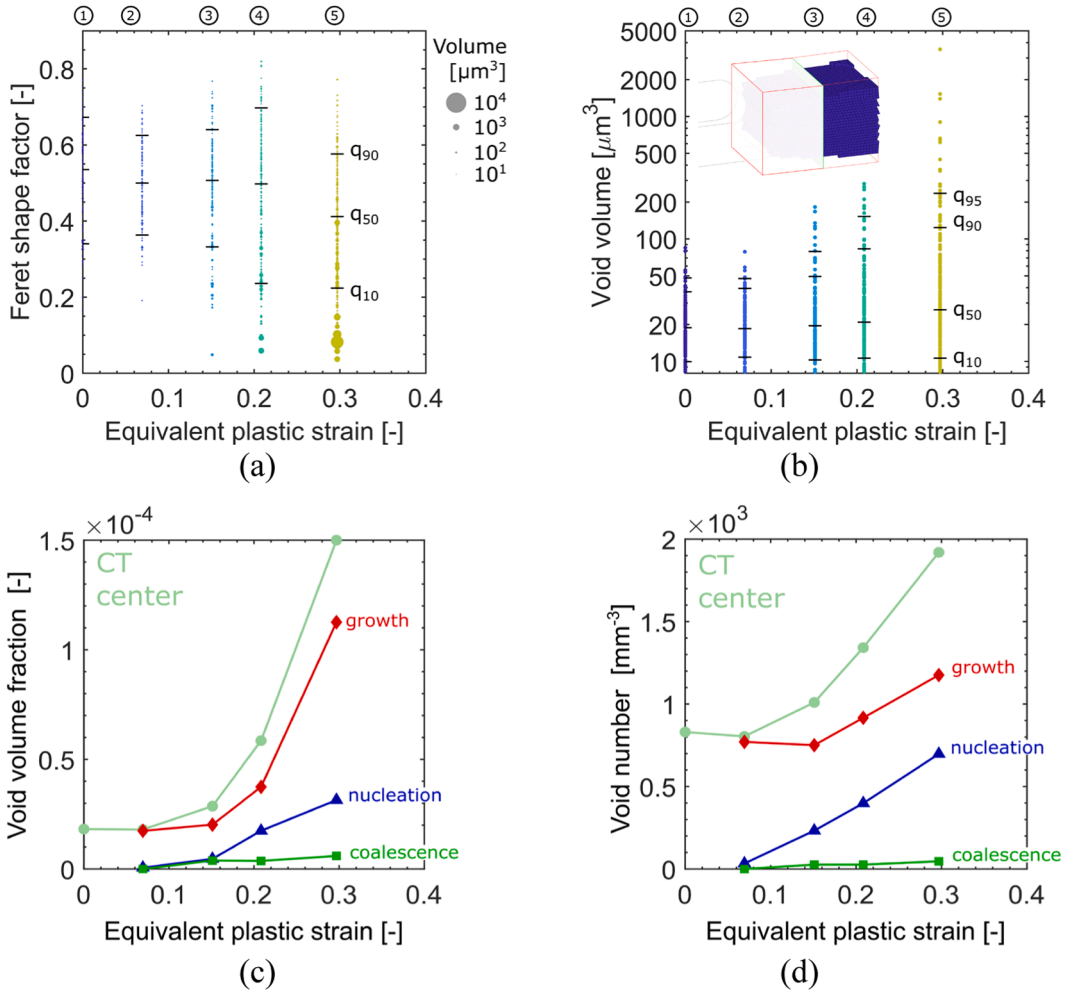

Fig. 29. Void population analysis of the CT-center/volume. Evolution of the (a) Feret shape factor, (b) void volume, (c) void volume fraction and (d) the void number per mm^3. The corresponding quantiles are denoted by horizontal black lines. The disc area in (a) scales linearly with the void volume. The total values in (c) and (d) are given in pale green, while the fractions for nucleation, growth and coalescence are given in blue, red and green, respectively. (For interpretation of the references to colour in this figure legend, the reader is referred to the web version of this article.)

Table 9
Summary of the CT experiment along with void volume fraction and void number evolution for the CT-edge with a trackable volume of 0.119 mm^3.

Step	NOD [mm]	F [kN]	VVF total [-] x10^{-5}				Void number/ unit volume [1/mm^3]				Stress State [-]		
			Total	Nucl.	Growth	Coal.	Total	Nucl.	Growth	Coal.	Triax.	Lode	EQPS
①	0.000	0.000	1.76	–	–	–	805.0	–	–	–	−0.14	−0.08	0.00
②	0.056	1.822	2.18	0.5	1.64	0.04	897.2	259.9	628.9	8.4	0.71	0.47	0.15
③	0.100	2.222	11.52	7.26	4.02	0.24	2289.2	1442.3	830.1	16.8	0.69	0.58	0.30
④	0.127	2.362	51.72	9.24	17.77	24.71	4653.8	2557.5	2020.8	75.5	0.68	0.60	0.38
⑤	0.163	2.485	187.4	20.65	49.51	117.3	7974.4	3739.8	4175.9	58.7	0.65	0.57	0.47

Table 10
Summary of the CT experiment along with void volume fraction and void number evolution for the CT-center with a trackable volume of 0.151 mm^3.

Step	NOD [mm]	F [kN]	VVF total [-] x10^{-5}				Void number/ unit volume [1/mm^3]				Stress State [-]		
			Total	Nucl.	Growth	Coal.	Total	Nucl.	Growth	Coal.	Triax.	Lode	EQPS
①	0.000	0.000	1.82	–	–	–	830.3	–	–	–	0.11	0.30	0.00
②	0.056	1.822	1.80	0.06	1.74	0.00	803.7	33.2	770.5	0.0	0.63	−0.39	0.07
③	0.100	2.222	2.87	0.46	2.02	0.39	1009.6	232.5	750.6	26.6	0.67	−0.29	0.15
④	0.127	2.362	5.85	1.74	3.74	0.37	1341.7	398.5	916.6	26.6	0.70	−0.25	0.21
⑤	0.163	2.485	15.00	3.14	11.30	0.60	1919.6	697.4	1175.7	46.5	0.73	−0.21	0.30

(Fig. 29c). This is almost solely attributed to coalescence, which contributes 63 % to the total VVF for the CT-edge and only 1 % for the CT-center. Remarkably, the void number per unit volume for coalescence is almost on par for the two zones. In other words, in the CT-edge a small number of voids coalesces into very large volumes. When looking at growth, both center and edge volumes follow similar trajectories, reaching a VVF of about 4×10^{-5} and 11×10^{-5} at a plastic strain of 0.3, with 830 and 1175 voids per mm^3, respectively. However, for the CT-edge a VVF for growth of 49.51×10^{-5} is reached at the last step with plastic strain of 0.47, with >4175 voids per mm^3. Similar trajectories are observed for nucleation – both volumes reach a VVF of about 4×10^{-5}, at a plastic strain of 0.3, while the maximum number of voids nucleated per unit volume is 1442 for the CT-edge and 697 for the CT/center. A summary of all measurements of the CT-edge and CT-center regions are given in Tables 9 and 10, respectively. Additional information on the evolution of the void shape and volume is given in Fig. E3.

5. Discussion

5.1. Fracture mechanisms

The experiments on four different specimen types reveal the sequence of events from damage initiation to final fracture for distinct stress states. At an early stage of plastic loading, two important microstructural damage mechanisms become apparent in all AA2198-T851 specimens: (i) intermetallic particles begin to crack and debond from the matrix; and (ii) flat micro-cracks appear mainly from grain boundaries. These mechanisms can be inferred from the segmented images discussed above, from slices of the reconstructed laminography volumes shown in the Appendices (Figs. B2, C2, D2, E1) and selected fractography (Figs. B4, C4, D5). For the CH-, NT- and CT-specimens, the maximum principal axis of the micro-cracks (coalesced voids) is approximately perpendicular to the direction of loading (Figs. 13, 18, 22, 27), while for the SH specimen (Fig. 9), it is aligned with the direction of simple shearing.

Further into the loading, these mechanisms progress at different rates for the different specimens (and stress states). The micro-cracks begin to open in a stable manner. This occurs mainly along the direction of maximum shear (Mode II) for SH, and normal to the direction of maximum tension (Mode I) for all other experiments. This process leads to significant micro-crack growth and coalescence until final specimen failure. Different from the damage mechanism of ferritic-bainitic FB600 steel [56] and aluminum alloy AA2024 [57], particle related void growth evolves slowly and seems to have only limited impact on the

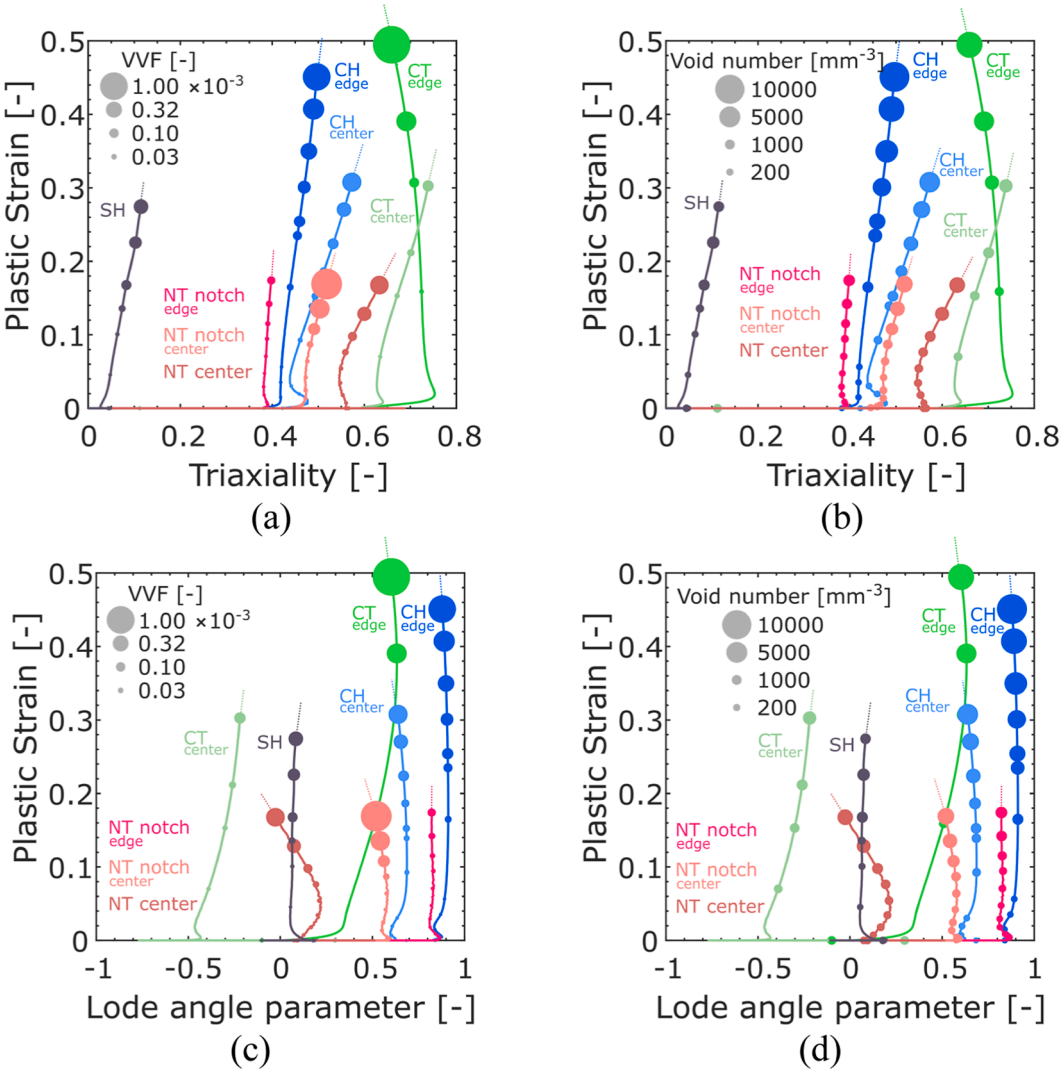

Fig. 30. Loading histories for all observed volumes for (top row) the stress triaxiality and (bottom row) the Lode angle parameter. The measured void volume fraction (VVF) (left column) and the void number per unit volume (right column) are denoted by circles. It should be noted that the last measurement does not coincide with the onset of fracture.

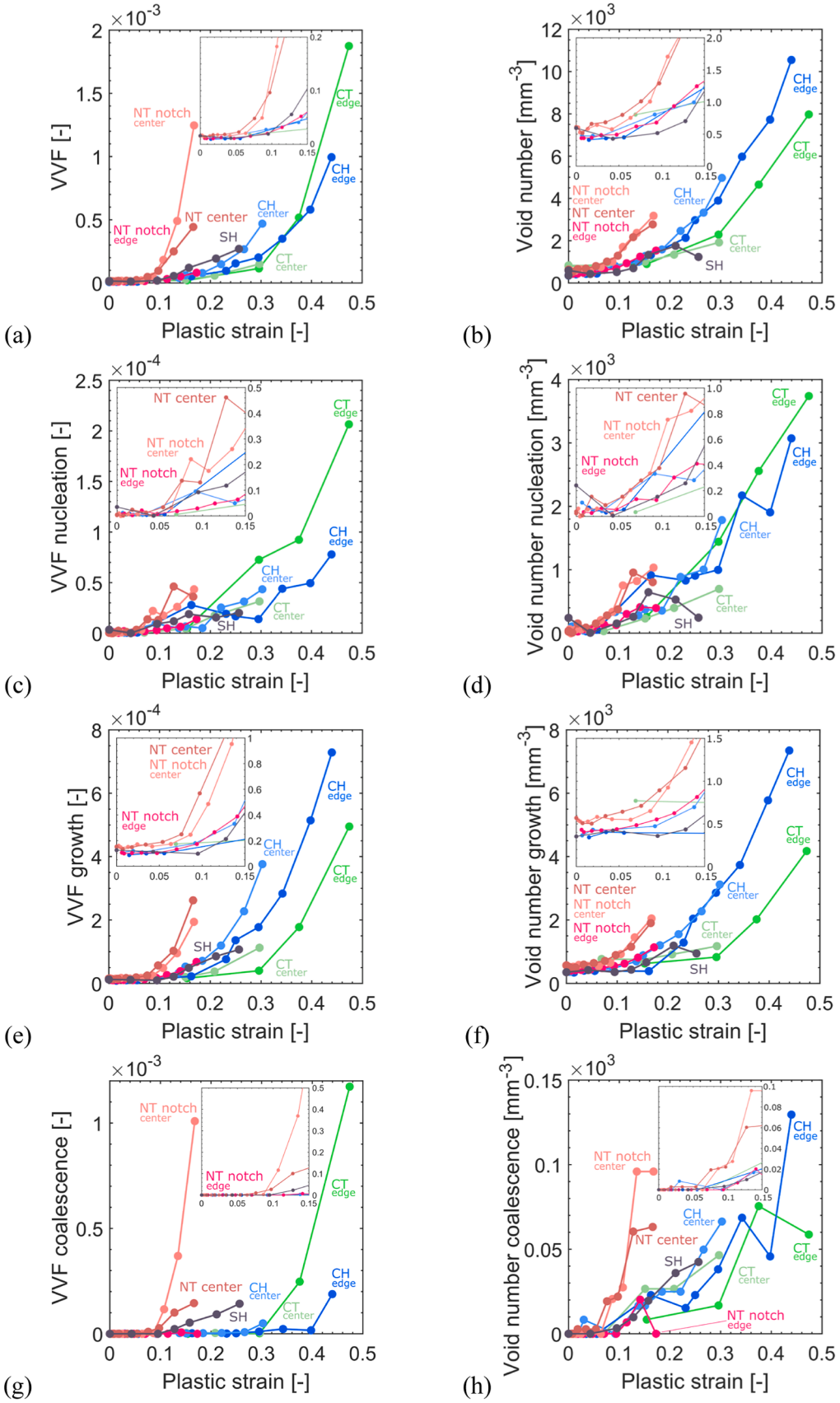

Fig. 31. Evolution of (left column) the void volume fraction (VVF) and (right column) the void number per unit volume for all observed volumes separated in (a-b) total, (c-d) nucleation, (e.f) growth and (g-h) coalescence. It should be noted that the last measurement does not coincide with the onset of fracture.

final fracture of the AA2198-T851. It should be noted that due to the sheet nature of the investigated material and the chosen specimen geometries, no observations are made at stress triaxiality above $\eta > 1.2$.

5.2. Effect of stress state on void evolution

Fig. 30 shows the evolution of the stress triaxiality (left column) and Lode angle parameter (right column) averaged over the trackable volumes. It showcases the wide range of stress states, from shear to biaxial tension, covered in this experimental campaign. It should be noted that comparable stress states can be obtained for different specimen geometries, e.g. the NT-notch/edge and the CH-edge (uniaxial tension) or the NT-center and NT-notch/center (plane strain tension). Fig. 31 compares the evolution of the void volume fraction (left column) and void number per unit volume (right column) for all regions and mechanisms (total (a-b), nucleation (c-d), growth (e-f) and coalescence (g-h)). Independent of the mechanism, it is reassuring that regions with similar stress states (NT-center and NT-notch/center, CH-edge and NT-notch/edge) exhibit similar evolutions in VVF and void number. Furthermore, the evolutions for the CH-center fall between the NT-center and the CH-edge, which is in agreement with their respective stress state history (Fig. 30). This directly implies that similar stress state histories will result in similar VVF and void number, i.e. damage evolution.

Regions undergoing plane strain tension loading (NT-notch/center and NT-center) tend to initiate damage significantly earlier, increasing at a much higher rate. This holds true for all damage mechanisms while being very pronounced for coalescence. Compared to this, regions undergoing tensile dominated loading, with a Lode angle parameter close to unity (i.e. both CH regions and the CT-edge), attain much larger plastic strain, as well as higher void numbers and VVF at the last observable loading step. For these stress states, the material can sustain high plastic straining with relatively low damage. The large VVF together with the large number of voids per unit volume indicates that damage is spread over many (smaller) voids and microcracks, which leads to further damage tolerance. In other words, for certain stress states, the nucleation of a large number of small voids appears to lead to an increase in the attainable plastic strain. It is speculated that this mechanism leads to a locally more uniform (and homogeneous) distribution of the loading of the material which will eventually cumulate in a void sheeting event of smaller voids at a smaller scale [57]. These observations agree qualitatively with the findings in [8].

The SH-volume differs substantially from all other regions. It shows very high and stable coalescence in VVF accompanied by moderate nucleation and growth, while the evolution of the void number per unit volume is on par with the tension dominated CH-and CT-regions, only decreasing in the last observable step. Stable coalescence behavior is observed, which is tentatively attributed to the low triaxiality value (up to 0.1) preventing the opening of very large voids. The principal damage mechanism under low triaxiality cannot be captured by the overall void volume fraction, but rather by the development of a few very large microcracks in a sequence of growth and coalescence.

When focusing on nucleation, the VVF (Fig. 31c) and the number of voids (Fig. 31d) show no clear dependence on the stress state and appear to be mainly driven by the increase in plastic strain. Similar nucleation rates are obtained for all observed volumes and only at higher strain levels, the CH- and CT-regions show a more rapid increase in the void number per unit volume. It should be noted that experiments at higher resolution would allow to further study the void nucleation process [58].

For the void growth mechanism, all regions follow an exponential growth in VVF and void number (Fig. 31e-f); they initiate at different strain levels and follow slightly different exponents, with the exception of the SH. Among the stress states covered here, plane strain tension seems to result in the earliest increase of the VVF and the void number.

When looking at coalescence, it is noteworthy that for all regions with generalized shear stress states ($\overline{\theta} \approx 0.0$, NT-center, NT-notch/center and SH) this mechanism occurs early into the loading at plastic strains as low as 0.1 with significant VVF and void numbers per unit volume (Figs. 31g,h). For zones with generalized tension or compression ($\overline{\theta} \approx \pm 1$, CH- and CT-volumes), coalescence is observed at much higher strains of about 0.3 and 0.4, respectively. Overall, an increase of coalescence activity occurs very close to final fracture; it typically corresponds to the formation of microcracks. In addition, distinct differences are observed in the rate of coalescing voids per unit volume (Fig. 31h). It is more than two times higher for the volumes that undergo plane strain tension loading as compared to the others (CH- and CT-volumes). At the same time, for the NT-notch/edge region ($\eta \approx 0.4, \overline{\theta} \approx 0.9$), almost no increase in VVF or void number is observed. Overall, the above observations suggest that generalized shear stress states ($\overline{\theta} \approx 0$) favor coalescence and hence the early failure.

When looking at the evolution of the largest three voids in each region (Figs. 10, 14, 15, 19, 23,24, 28, 29b), it becomes apparent that these voids grow significantly larger for regions with near zero Lode angle parameter. This is tentatively attributed to earlier localization and more heterogenous strain fields, which can be observed, for example in the surface DIC field of the NT specimen (Fig. D1) or its xz-plane projection (Fig. D4c,d). It is speculated that voids will grow faster in localized bands, leading to a small number of very large voids, which will result in earlier coalescence and failure. Microstructure based simulations, e.g. [33,59], or Digital Volume Correlation (DVC), e.g. [43], could help shed more light on this observation.

For the development of void evolution models the following findings could be most relevant. The void evolution is only a function of the stress state and equivalent plastic strain. Below an equivalent plastic strain limit, in the present case about 0.07,[2] the void population does not change noticeably. Only above this limit, all regions exhibit an exponential increase in VVF and void number for all mechanisms. Except for simple shear, the void volume fraction appears as a good indicator of damage. The highest VVF for a given strain is observed for plane strain tension, which is consistent with the "plane strain valley" that is typically observed for metals when plotting the fracture strain as a function of the stress-triaxiality. However, there is competition between the global behavior of a region and the development of a few stable large microcracks within it. This could require modeling approaches allowing for the development of localized deformation zones. Void nucleation seems to be stress state independent, i.e. it is a function of the plastic strain only. In contrast, void growth as well as void coalescence rates appear to be stress state dependent. Further, a generalized shear state, i.e. Lode angle parameter zero, results in earlier void growth as well as coalescence. There is a distinct Lode angle dependent threshold for the onset of coalescence, which starts as early as the beginning of initial void evolution for the generalized shear state. The differences in the void evolution curves for the different specimens suggest that void nucleation can delay the growth of extremely large voids, thereby increasing the apparent macroscopic strain to fracture.

6. Conclusion

A new hybrid experimental-numerical postprocessing technique is proposed to analyze the evolution of damage during in-situ laminography experiments. The central idea is to make use of the displacement field obtained from basic finite element simulations to facilitate the tracking of voids inside monotonically-loaded specimens. Specifically, the centroids of voids observed at a given stage of loading (current configuration) are mapped back to the initial configuration using FE-computed displacements. In conjunction with a novel tracking

[2] Recall that the limited spatial resolution of the experimental setup and analysis does not suffice to detect any void nucleation, growth or coalescence below a volume of $8\mu m^3$

algorithm, this mapping onto a common reference configuration turns out to be effective for monitoring the damage evolution. In particular, the tracking algorithm detects whether a void observed at time step n is the outcome of nucleation or the growth and/or coalescence of voids present at time step n-1.

A comprehensive program of in-situ laminography experiments is performed to gain insight into the stress-state dependency of the ductile failure of aluminum alloy 2198-T851 by studying regions of interest in flat samples at micrometer resolution. It comprises static monotonic experiments on shear (SH), central hole tension (CH), notched tension (NT) and compact tension (CT) specimens. These experiments cover primarily biaxial stress states ranging from simple shear to equi-biaxial tension. The observations include 3D reconstructions with a voxel size of about 0.7μm at about ten different stages per experiment. The experimental results are reported in great detail including the void sizes, the number of voids, the void shapes (Feret shape factor) and the void volume fractions along with the mechanism of origin (nucleation, growth, coalescence). In addition, the corresponding average stress state and macroscopic strain estimates are provided based on continuum scale finite element simulations with an anisotropic non-porous phenomenological plasticity model.

The main findings of the investigation are:

- Experimental evidence of two primary damage mechanisms is observed: (i) at early stages of plastic straining $\left(\bar{\varepsilon}_p < 0.1\right)$: (1) cracking and debonding of intermetallic particles from the polycrystalline matrix, and the (2) emergence of inter- and transgranular micro-cracks. (ii) At stages of high plastic straining $\left(\bar{\varepsilon}_p > 0.1\right)$, grain boundaries unzip in a stable manner, leading to specimen fracture due to micro-crack growth and coalescence.
- Micro-crack coalescence appears to be more likely for generalized shear (zero Lode angle parameter) than for generalized tension (Lode angle parameter unity). Different from grain-boundary micro-cracks, particle-related void growth is slow. The latter damage mechanism has limited impact on the ductile fracture of the present 2198-T851 aluminum alloy, contrasting with earlier findings on ferrite-bainite steel (FB600) and the aluminum alloy 2024-T351.
- The evolution of the Feret shape factor and void volumes across different specimens suggest that the nucleation of new voids slow down the growth of large voids, thereby enhancing the material's ductility at the macroscopic level.

CRediT authorship contribution statement

Christian C. Roth: Writing – original draft, Visualization, Validation, Software, Project administration, Methodology, Formal analysis, Data curation, Conceptualization. **Thilo F. Morgeneyer:** Writing – review & editing, Supervision, Resources, Methodology, Investigation, Funding acquisition, Conceptualization. **Lukas Helfen:** Software, Resources, Investigation, Funding acquisition. **Dirk Mohr:** Writing – review & editing, Supervision, Funding acquisition, Conceptualization. **Thomas Tancogne-Dejean:** Writing – original draft, Visualization, Validation, Software, Methodology, Investigation, Formal analysis, Data curation, Conceptualization.

Declaration of competing interest

The authors declare that they have no known competing financial interests or personal relationships that could have appeared to influence the work reported in this paper.

Acknowledgements

Drs. Ante Buljac and Xiang Kong (MINES Paris) are thanked for the help with the in-situ experiments. The European Synchrotron Radiation Facility (ESRF), beamline ID19, is thanked for providing beamtime (experiments ma1006 and ma2183). Constellium C-TEC is thanked for materials supply. ANR is also acknowledged for partial funding of this work through projects Cominside (ANR-14-CE07–0034) and Lambda (ANR17-CE08–0051). Prof. Vincent Grolleau (ETH/UBS) is thanked for fruitful discussions. Mr. Knut Krieger (inspire AG) is thanked for specimen preparation for microscopy and Ms. Chiara Monti (inspire AG) is thanked for the help with the EDX analysis.

Appendix A. Finite Element Analysis

Finite element simulations are carried out for all experiments (SH, CH, NT, CT) to (i) identify the parameters of the material model and (ii) to extract relevant quantities at each material point during loading. This comprises the displacements, the stress triaxiality and the Lode angle parameter along with the equivalent plastic strain.

Constitutive framework

Along with isotropic elasticity (Young's modulus E, Poisson ratio ν), an extension of the Yld2000–2d [60,61] with parameters $\alpha_1, \ldots, \alpha_8$ and exponent m is used to describe the AA2198-T851 with self-similar hardening and an associated flow rule. A linear combination with weighting parameter $\alpha \in [0,1]$ of a Swift law [62] with parameters $\{A, \varepsilon_0, n\}$ and a Voce law [63] with parameters $\{k_0, Q, \beta\}$ is used to describe the deformation resistance $k\left[\bar{\varepsilon}_p\right]$ as a function of the equivalent plastic strain:

$$k_\varepsilon\left[\bar{\varepsilon}_p\right] = \alpha A\left(\varepsilon_0 + \bar{\varepsilon}_p\right)^n + (1-\alpha)\left\{k_0 + Q\left(1 - e^{-\beta\bar{\varepsilon}_p}\right)\right\}. \tag{8}$$

For a more detailed description of the model, the reader is referred to [57].

Specimen discretization and calibration procedure

All simulations are carried out with the finite element software Abaqus/Explicit v6.14, applying uniform mass scaling so that at least 250′000 time increments are reached. Taking advantage of the specimen's symmetries, only one-eighth of the CH and NT specimens are modeled, while a quarter of the SH and CT specimens are discretized. The height of the meshed region corresponds to half of the extensometer length from the respective experiment. Zero normal displacement constraints are applied to all nodes on the symmetry surfaces, while the measured displacement-time history is applied to the nodes on the upper face of the model. To accurately represent the geometric deformation, particularly during necking, a very fine mesh with element edge length of 25μm is used in the critical regions, corresponding to 20 elements over half the thickness. An overview of the four geometries is given in Fig. A1.

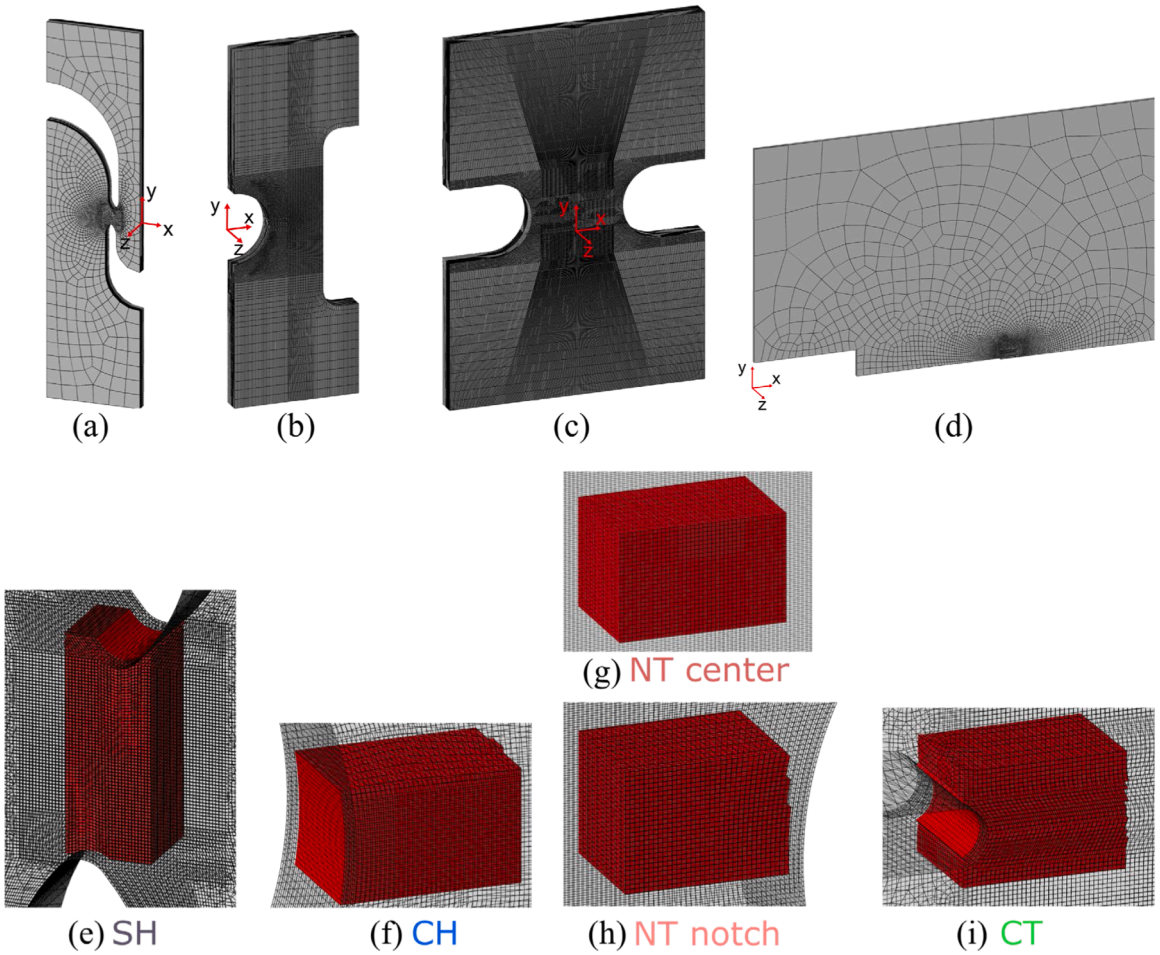

Fig. A1. Finite Element mesh for the (a) shear (SH), (b) central hole (CH), (c) notched tension (NT) and (d) compact tension (CT) specimens. The corresponding observable volumes of the laminography experiment are shown in red in (e)-(i).

Following the methodology of Dunand et al. [61], the yield stress ratios of the three uniaxial tensile experiments along with their corresponding Lankford ratios are used to obtain an initial guess of the eight alpha parameters of the Yld2000 model with an chosen exponent of m = 8 [64]. The strain hardening parameters for the Swift and Voce models are obtained from independent least-square fits of the true stress-true strain curve in the 0° direction. Subsequently, the parameters $\mathbf{p} = \{Y_{EBT}, r_{EBT}, \alpha\}$ are used to minimize the difference between the experimental and computed force-displacement curves for the SH, CH, NT and UT (RD (0°), DD(45°), TD(90°)) experiments through the cost function

$$\Phi[\mathbf{p}_k] = \sum_{j=1}^{6} \frac{1}{N_j} \sum_{i=1}^{N_j} \left(F_{j,i}^{\exp}[u] - F_{n,i}^{sim}[u, \mathbf{p}_k] \right)^2. \tag{9}$$

Herein $F_i^{\exp}$ and F_i^{sim} denote the force levels at the i th experimental data point (with a total of $N_j = 100$ points per curve). Fig. A2 gives an overview of the calibrated model along with the yield surface for different shear stress levels. Table A1 gives an overview of the identified material model parameters.

Table A1
Material model parameters (Yld2000–3D) for AA2198-T851.

E [GPa]	ν [−]	ρ [kg/m^3]	m [−]				
70	0.33	2897	8				
α_1 [−]	α_2 [−]	α_3 [−]	α_4 [−]	α_5 [−]	α_6 [−]	α_7 [−]	α_8 [−]
0.90896	0.99905	0.85422	0.99592	0.98062	0.81424	0.97348	1.19405
A [MPa]	ε_0 [−]	n [−]	k_0 [MPa]	Q [MPa]	β [−]	α_{SV} [−]	
677.87	0.0253	0.0945	479.83	87.59	17.45	0.15	

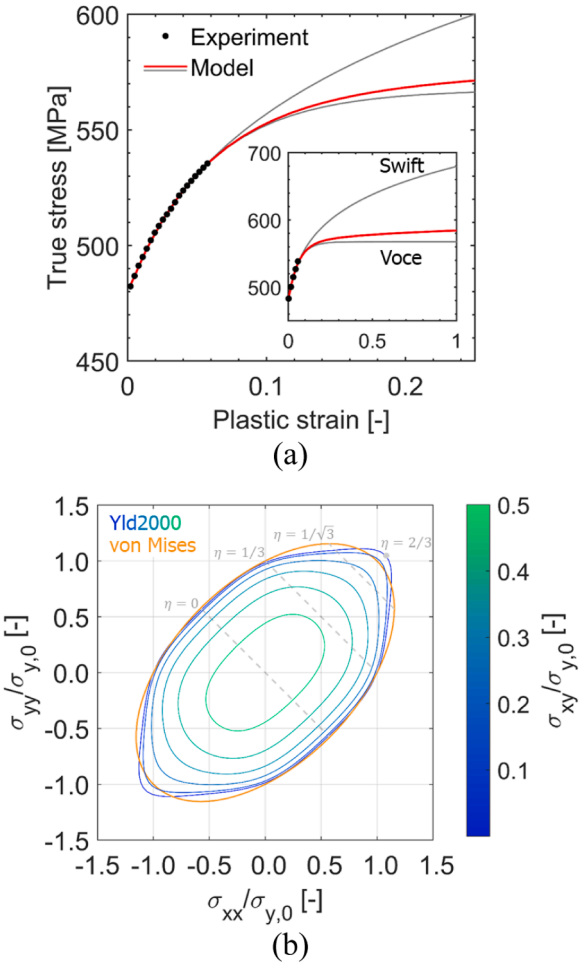

Fig. A2. Experimental and numerical results used for AA2198- T851: (a) True stress - plastic strain response for uniaxial loading (black dots) and calibrated Swift-Voce strain hardening (b) Yield surface of the calibrated Yld2000–3D model. The von Mises yield surface is shown as reference in orange.

Appendix B. Extended experimental results on SH specimen

The SH region is observed in eight loading steps before final failure. The corresponding force displacement curves from both in-situ and ex-situ experiments are shown in Fig. B1a. The view of the optical camera at step ⓪ of the laminography experiment is presented in Fig. B1b. It shows the two regions of interest used for digital image correlation (green area) and the area analyzed through laminography (red box). Selected results from the DIC measurement are shown in Fig. B1c. At step ④, two plastically-deformed zones are visible in the gage section of the shear specimen, in which plastic strain is accumulated during the subsequent loading steps. For the final step before fracture (step ⑧), a maximum effective strain of $\bar{\varepsilon}_{eff} = 0.48$ is measured in both gage sections. In step ⑨, the left gage section has failed between the apex of both cut-outs, while a maximum effective strain of $\bar{\varepsilon}_{eff} = 0.60$ is measured in the intact gage section.

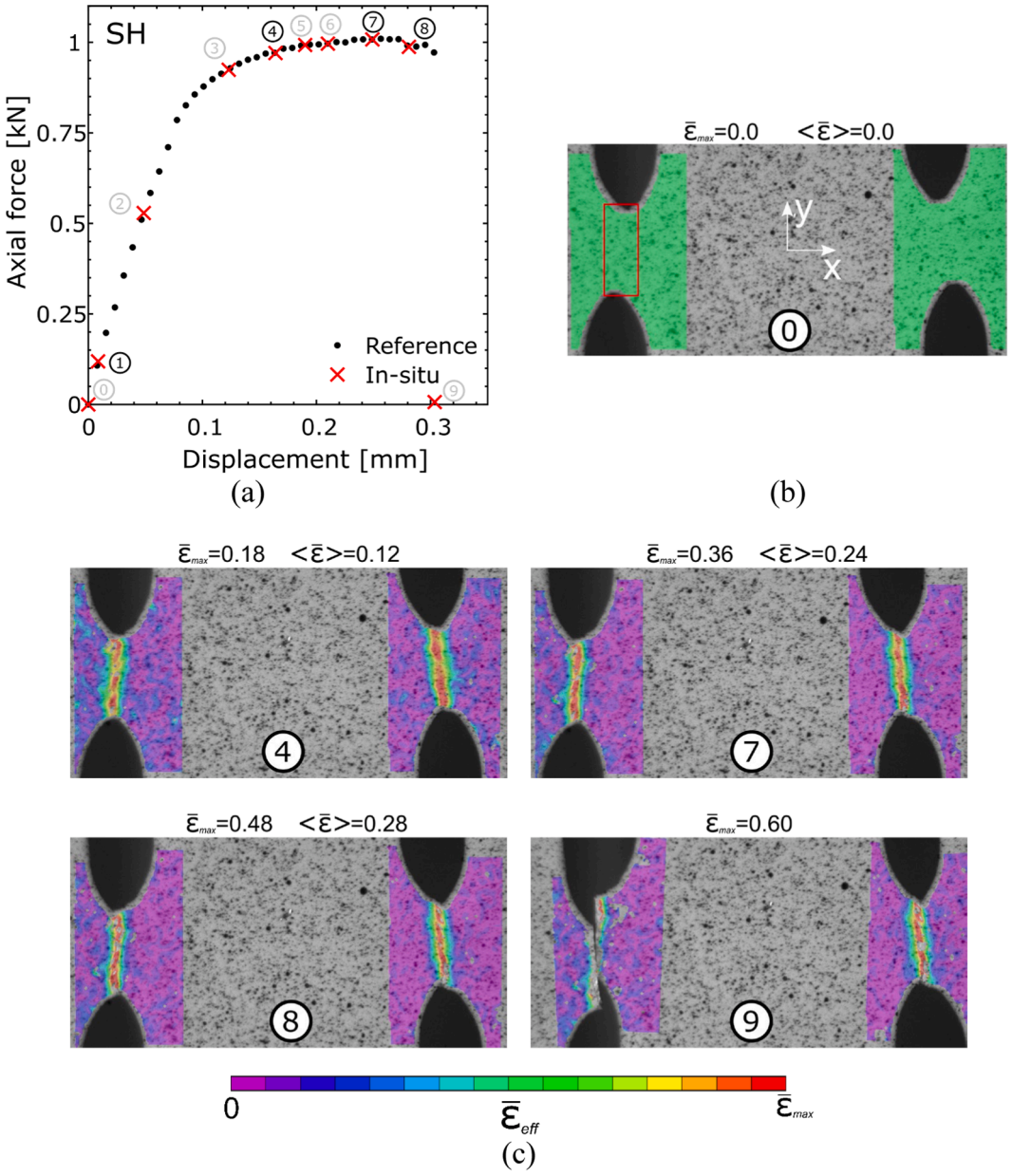

Fig. B1. Shear experiment: (a) Force-displacement curves for the macroscopic (solid black line) and the nine in-situ laminography load steps (red crosses). (b) Laminography experiment as seen by the optical camera. The green areas denote the regions of interest for DIC, the red box the region of interest observed by laminography. (c) DIC contour plots for selected load steps.

Reconstructed grayscale images are shown in Fig. B2. At the beginning of loading (step ①), several small and large intermetallic particles (light gray) are clearly visible in the matrix material (dark gray). However, no voids can directly be observed at the thickness slice of $z=-245\mu m$. Fig. B3 shows the corresponding projected 3D views of the segmented volume, in which the matrix material has been made transparent, while voids appear in color. For the first step, only a very small void volume fraction is observed.

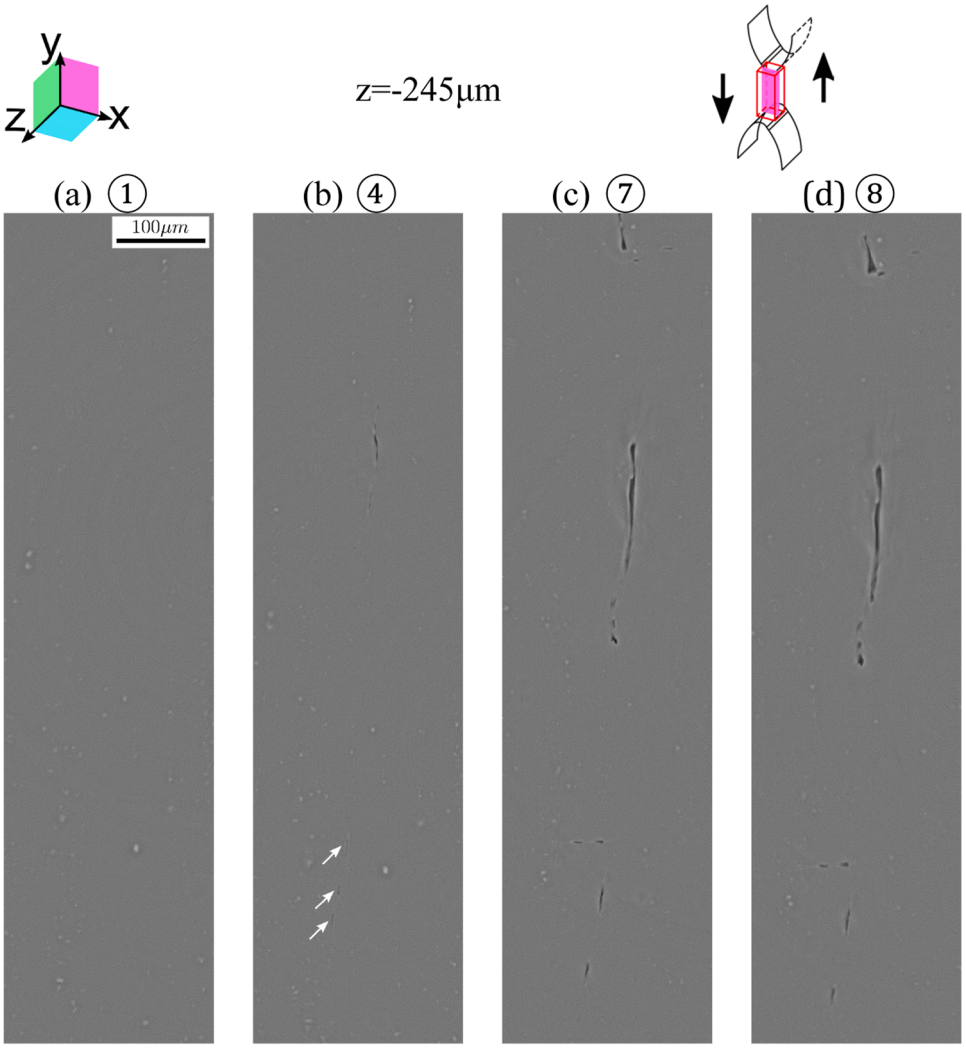

Fig. B2. Laminography images of the shear experiment at selected steps. (a) ① base material, (b) ④ micro-cracks become visible (white arrows) and grow (c-d) ⑦&⑧ along and perpendicular to the loading direction.

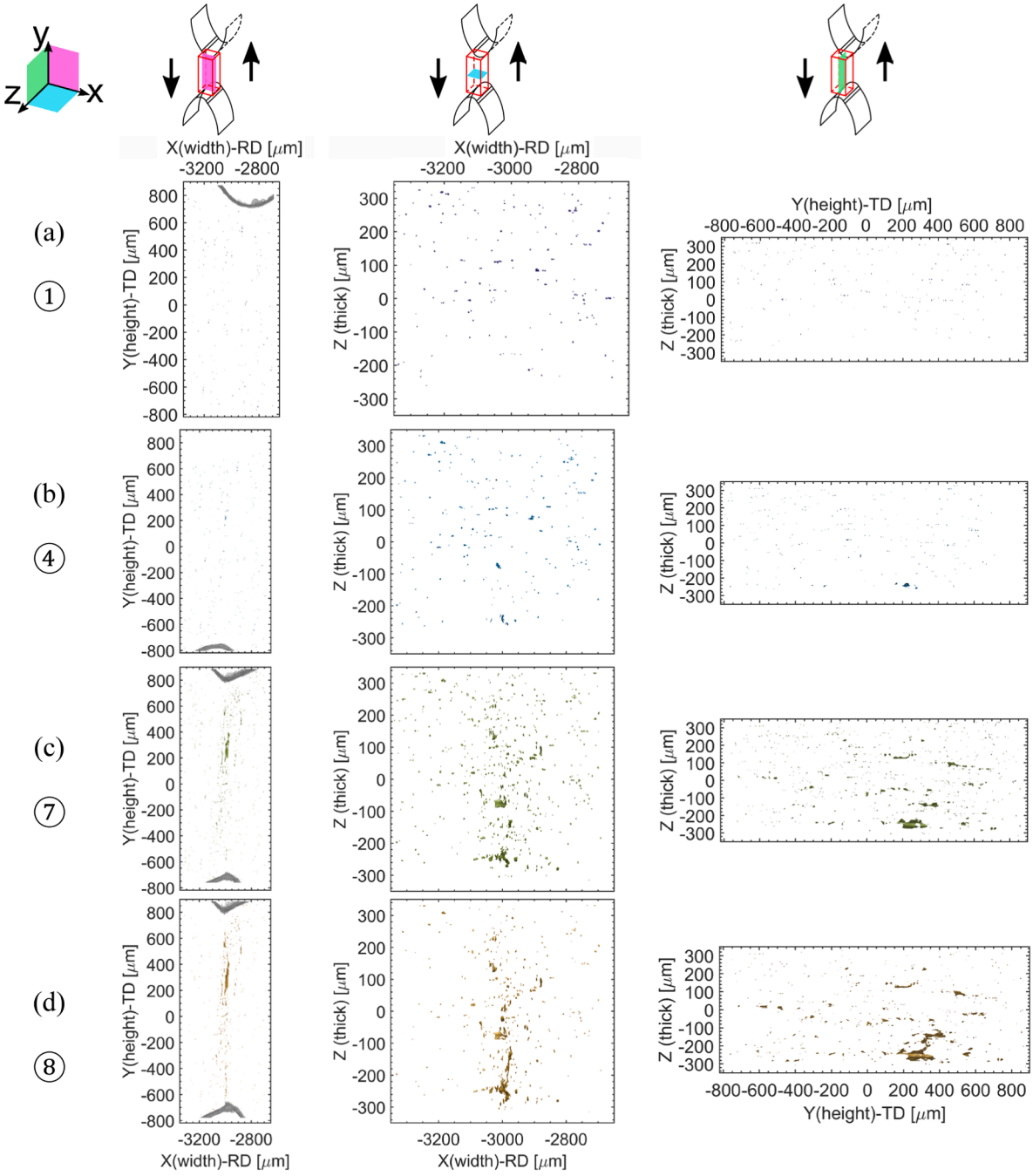

Fig. B3. Projected 3D views of the segmented observable volume of the shear experiment for selected steps. The notches are shown in light grey in the x-y plane for reference. The matrix material has been made transparent for visibility.

Shortly after the yield point (step ④), crack-like features are observed both in the grayscale slice (Fig. B2) as well as in the 3D reconstruction (Fig. B3). Besides the elongated micro-crack in the upper half of the image, smaller nucleation sites are highlighted by three white arrows. Upon further loading (steps ⑦ and ⑧), additional voids nucleate from the intermetallic particles and existing micro-cracks continue to grow (Fig. B3). The void features are mainly limited to the small band in the specimen gage section area which undergoes the highest levels of plastic deformation (x-y and x-z plane). At step ⑧, just before final failure, several flat micro-cracks have formed. One micro-crack extends >200 μm in length and almost 100 μm in width. It is also noteworthy that in the y-z plane, i.e. normal to the rolling direction, the voids seem to be positioned following virtual lines parallel to the transverse (loading) direction.

Post-mortem fractography of the shear specimens reveals a very smooth crack surface with some shear lips and almost no dimples (Fig. B4). The close up shows the presence of intermetallic particles on the crack surface. They have an approximate initial diameter of 2.9μm and are located at a distance of about 11μm, well aligned with the loading direction. Between the particles, and further along the loading direction, a groove extends for ca. 15μm. Within this "drag zone", one of the particles is shattered into two pieces, which are located at approximately 1.4$\mu m$from each other. It is speculated that these grooves have been formed by the motion of the hard particle in the softer matrix material, originating from particle fracture and de-cohesion during the later loading steps. This would also support the observation of void alignment with the loading direction along "virtual lines" in Fig. B3 (step ⑦&⑧).

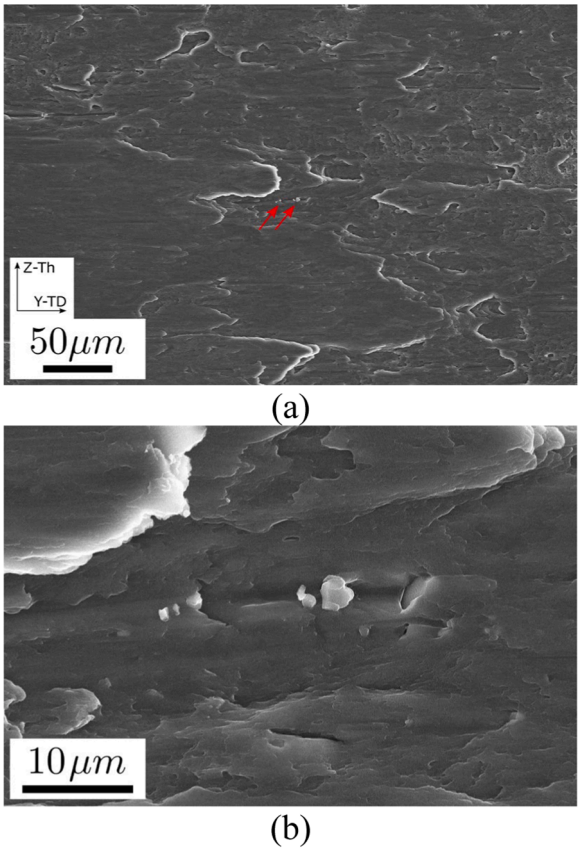

Fig. B4. Fractography of the macroscopic shear specimen: (a) Selected region of interest and (b) close-up around the red arrows. Besides shear lips, some (cracked) intermetallic particles and their drag marks are visible (red arrows).

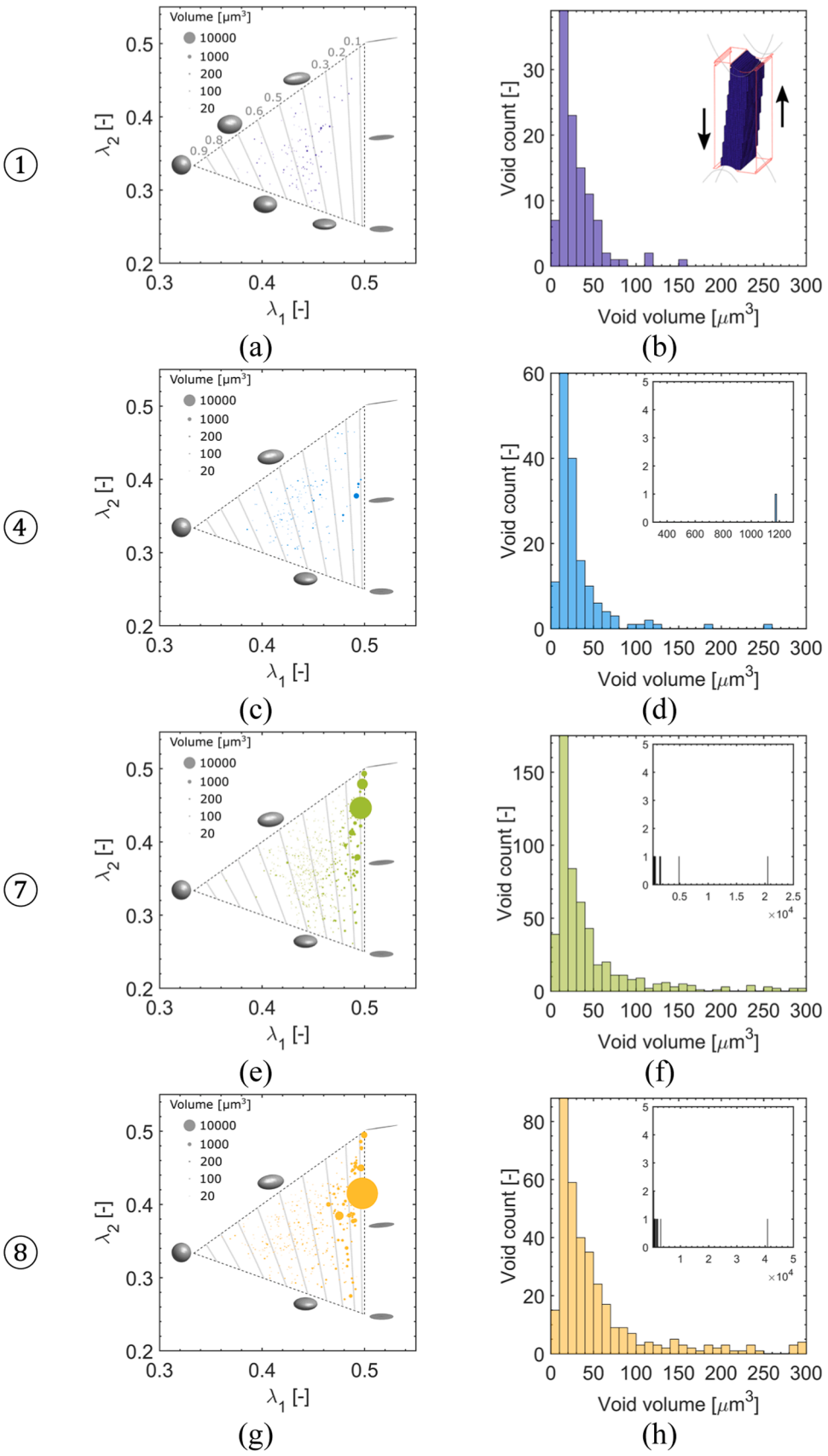

Fig. B5. Detailed void population analysis of the shear experiment for selected loading steps. Left column: evolution of the void shape (λ_1 vs. λ_2). Right column: Evolution of void count vs. void volume. Dashed lines denote constant Feret shape factors. The disc area scales linearly with the void volume.

Appendix C. Extended experimental results on CH specimen

The region on one side of the central hole is observed during 11 loading steps until final failure (red box, Fig. C1b). Fig. C1a presents the force displacement curves from both in-situ and ex-situ experiments along with the local axial strain from a 1 mm long extensometer on the side of the central hole. After an initial elastic range, a distinct yield point is observed at step ②, followed by a slight force increase up to 3.07 kN around step ⑨. Final failure is observed 0.2 mm later and about 0.05 mm after the last evaluated imaging step ⑪. Fig. 11b shows the area observed during in-situ experiments at step ⓪ with the region of interest for DIC (green area) and imaging area for laminography reconstruction (red area). Selected results from the DIC measurement are shown in Fig. 11c. Before maximum force (step ⑥), the strain localizes next to the central hole with a slight left-right asymmetry. The strain continues to increase in those regions up to the final loading step ⑪ where the effective surface strain reaches a critical value of 0.3. Failure later initiates on the left side of the gage section.

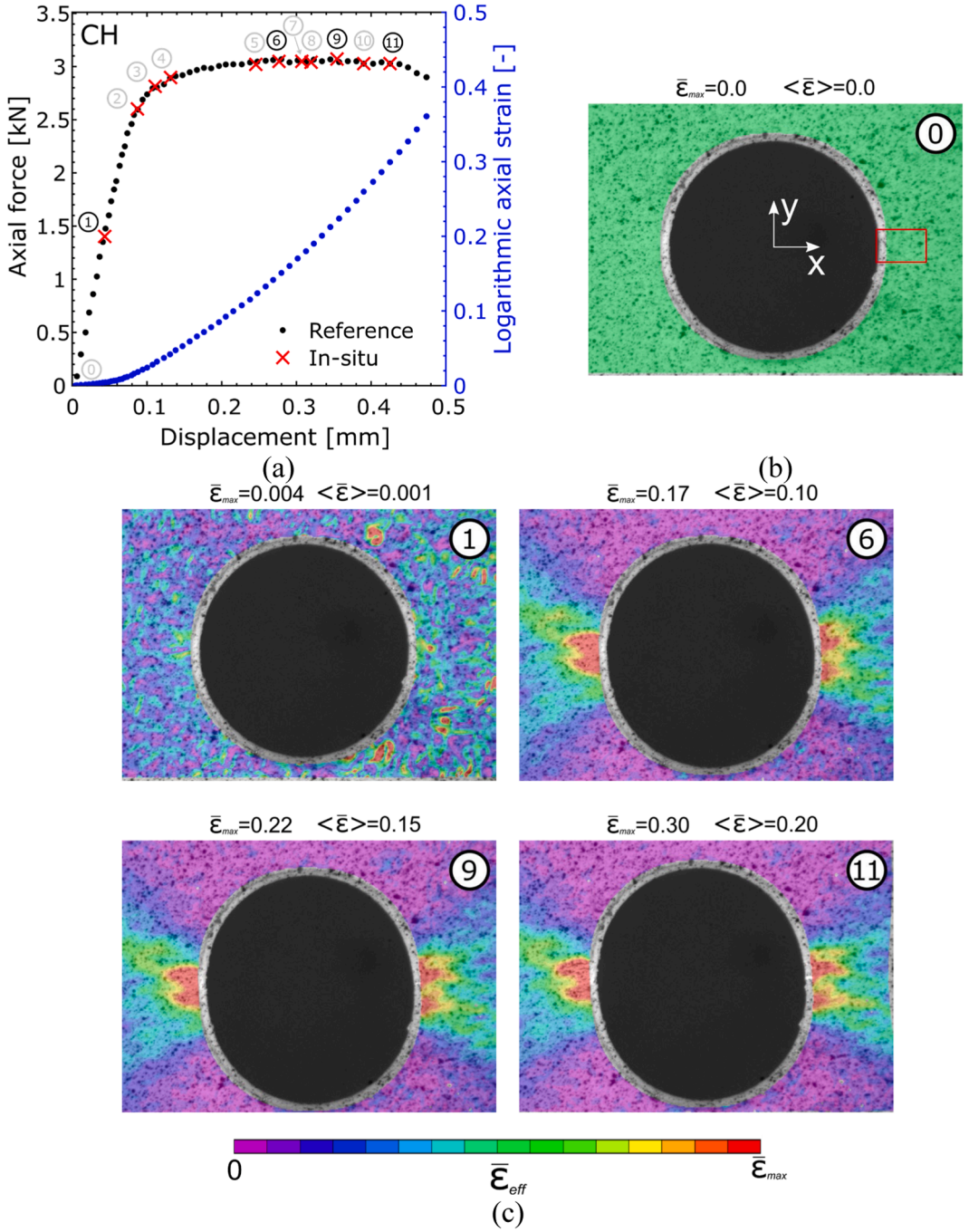

Fig. C1. Central hole experiment: (a) Force-displacement curves for the macroscopic (solid black line) and the eleven in-situ laminography load steps (red crosses). (b) Laminography experiment as seen by the optical camera. The green area denote the region of interest for DIC, the red box the region of interest observed by laminography. (c) DIC contour plots for selected load steps.

Fig. C2 shows reconstructed grayscale slices taken at mid-thickness (xy-plane, $z=-25$ µm) at selected loading stages. During the elastic step (①), preexisting voids are observed at the interface between second phase particles and matrix (white arrow Fig. 12a), i.e. particle-matrix decohesion. The second phase particles tend to align with the rolling (horizontal) direction. Further into the loading (step ⑥), the pre-existing voids continue to grow, while cracking of second phase particles is observed (e.g. rightmost arrow Fig. C2b). In addition, two elongated cracks appear in the matrix material along the x-direction (center arrow Fig. C2b). Both particle cracking and grain boundary decohesion occur perpendicular to the loading (vertical) direction. After maximum force (steps ⑨ and ⑪), all cracks continue to grow, with the highest growth rate on the elongated cracks. At the last step before failure, both cracks reach a length of 77 µm and are separated by about 20µm. Note that cracks also appear in a 20µm-wide brittle oxide layer around the central hole, however this is not part of the present investigation.

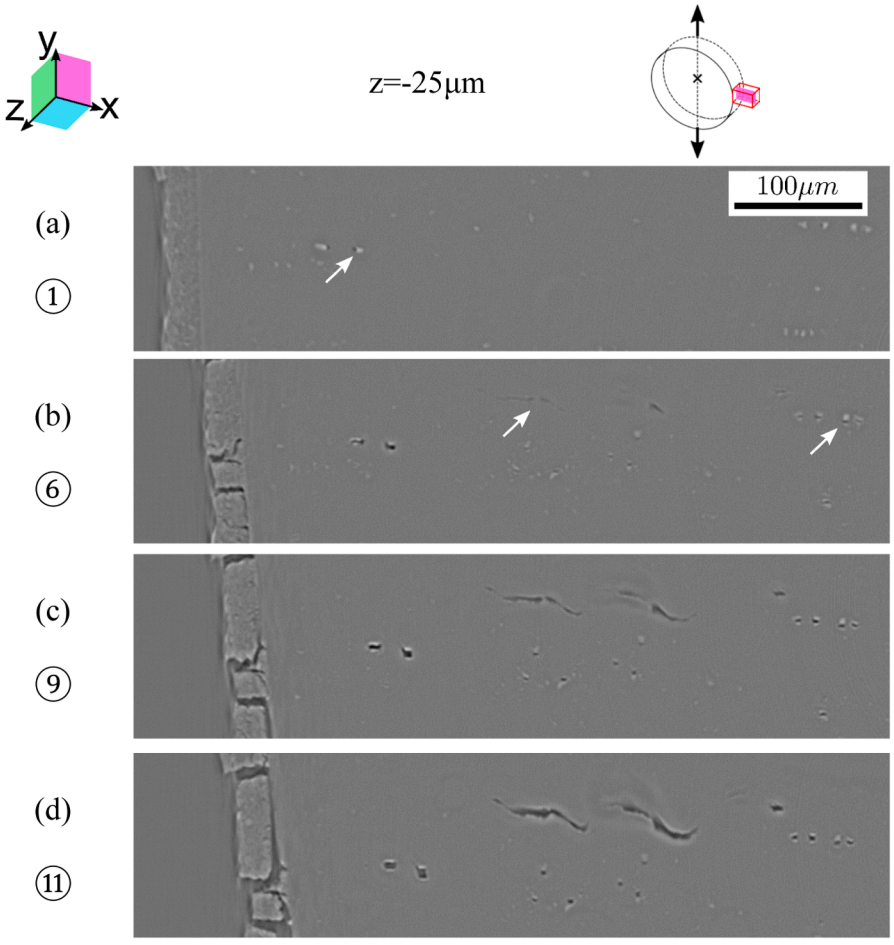

Fig. C2. Laminography images of the CH experiment close to the central hole at selected steps. (a) ① base material with intermetallic particle-matrix decohesion, (b) ⑥ brittle cracking of particles (right arrow) along with void growth and onsetting micro-cracks (left arrow) that grow (c-d) ⑨&⑪ perpendicular and inclined to the loading direction.

The 3D segmentation of the full volume (Fig. C3) indicates a similar behavior in the entire volume. Strong void nucleation is observed before maximum force (step ⑥) in the form of particle cracking and decohesion as well as a few incipient elongated cracks. Further into the loading, additional void nucleation and growth occurs in the vicinity of the central hole (step ⑨) and further away as the loading progresses (step ⑪). Two voids are found to extend >200 μm along the x-direction.

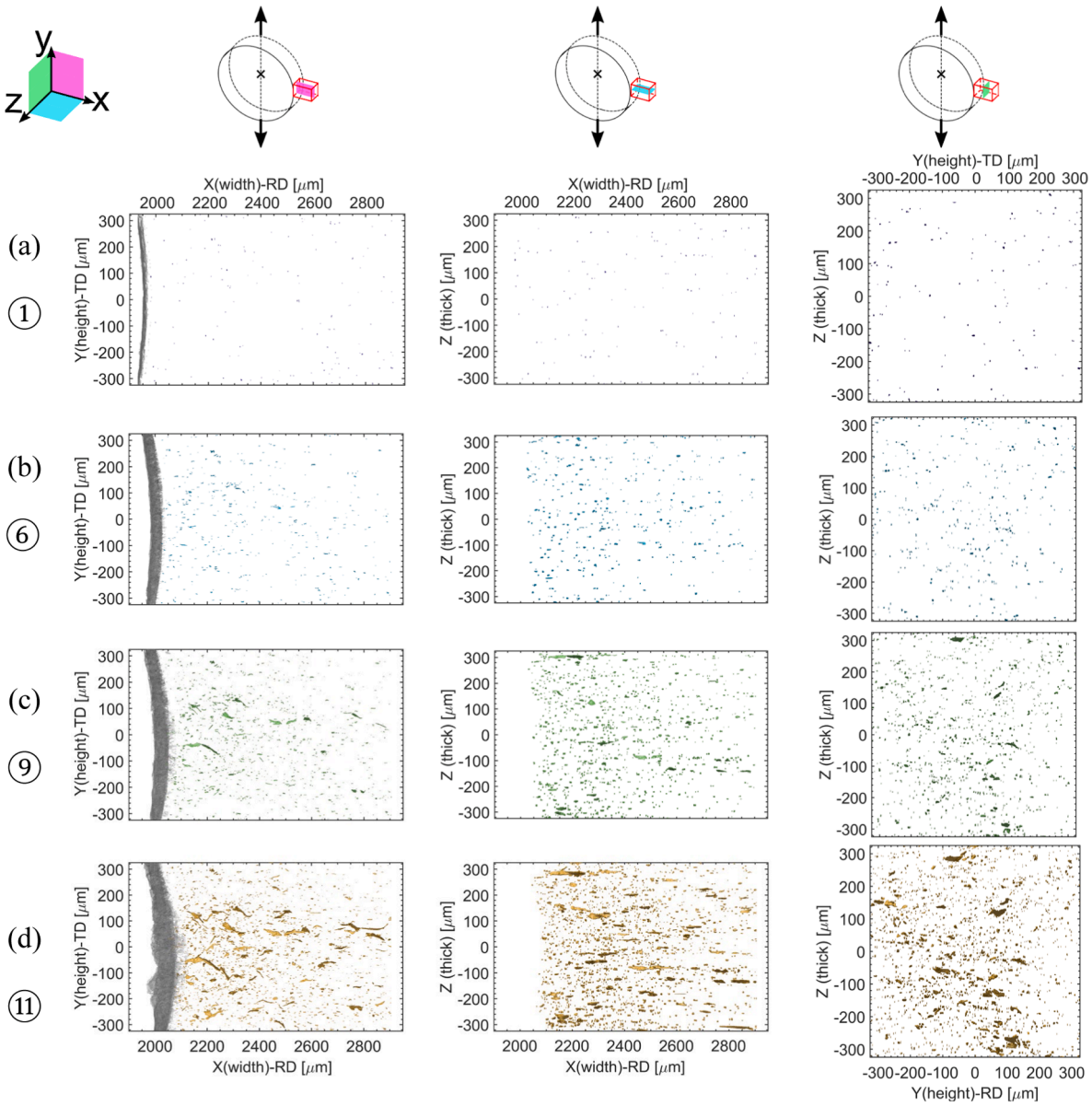

Fig. C3. Projected 3D views of the segmented volume of the central hole for selected steps. The notch is shown in light grey in the x-y plane for reference. The matrix material has been made transparent for visibility.

Fig. C4 shows selected micrographs of the fracture surface of the specimen. A triangular band reminiscent of the highly voided zone on Fig. C3d xz-plane is observed with many dimples within it (Fig. C4a). Outside the band, elongated features are observed. Second-phase particles are found at the bottom of the dimples (Fig. C4b,c). The particles are shattered in micron-sized pieces. Furthermore, long decohesion zones are observed (Fig. C4a,b), which are attributed to intergranular failure.

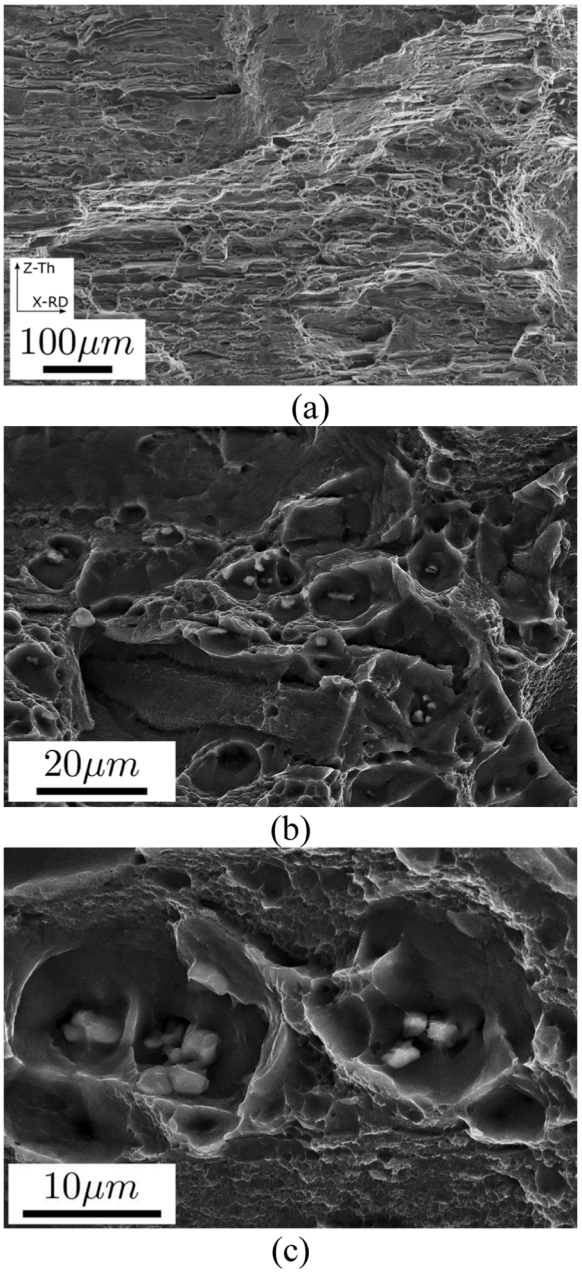

Fig. C4. Fractography of macroscopic central hole specimen. (a) Selected region of interest close to the hole edge (right hand side), (b) close-up of ductile dimples with (partially cracked) intermetallic particles at the bottom. Clearly visible is the lamellar/layered microstructure and intergranular failure.

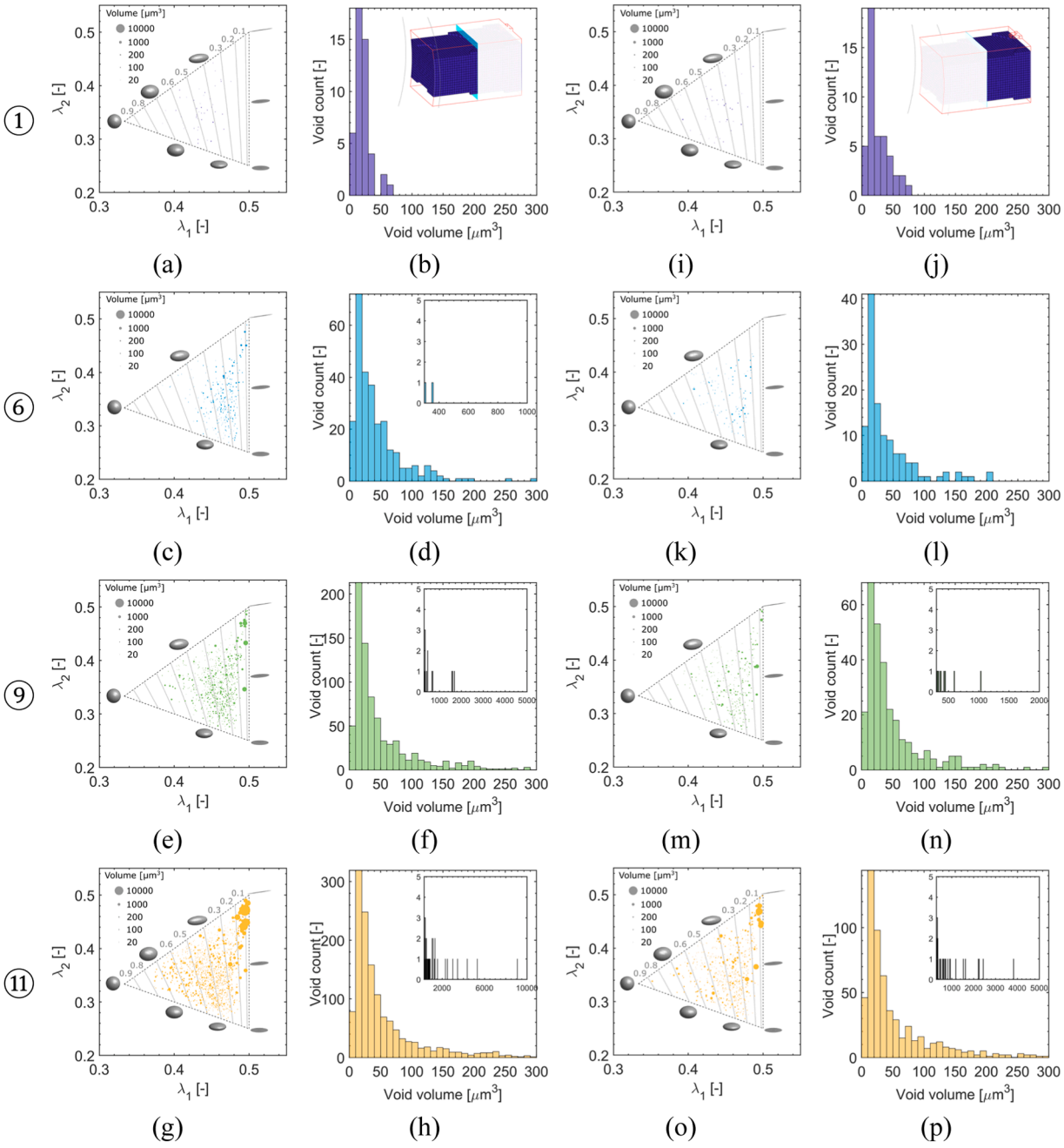

Fig. C5. Detailed void population analysis of the CH-edge (a-h) and CH-center (i-p) regions for selected loading steps. Left column: evolution of the void shape (λ_1 vs. λ_2). Right column: Evolution of void count vs. void volume. Dashed lines denote constant Feret shape factors. The disc area scales linearly with the void volume.

Appendix D. Extended experimental results on NT specimen

The two different regions of interest of the notched tension (NT) specimen are observed with 11 in–situ loading steps (red boxes, Fig. D1b). Fig. D1a shows the corresponding force-displacement response of the macroscopic NT experiment (black solid dots) along with the laminography results (red crosses). After an initial elastic response, a distinct yield point is visible at step ①, which is followed by a monotonic hardening up to a force maximum (2.76 kN, step ⑧) and a necking induced reduction of load carrying capacity until final fracture is attained at a displacement of 0.33 mm and 2 .66kN. Selected effective strain field are show in Fig. D1c. Already from initial yielding (step ①), strain concentrations are visible on the free boundaries of the gage section. These zones grow in bands towards the center of the specimen during further loading and all the way to fracture, reaching values of $\overline{\varepsilon}_{max} = 0.1$ at force maximum (step ⑧) and $\overline{\varepsilon}_{max} = 0.2$ before the onset of fracture (step ⑪).

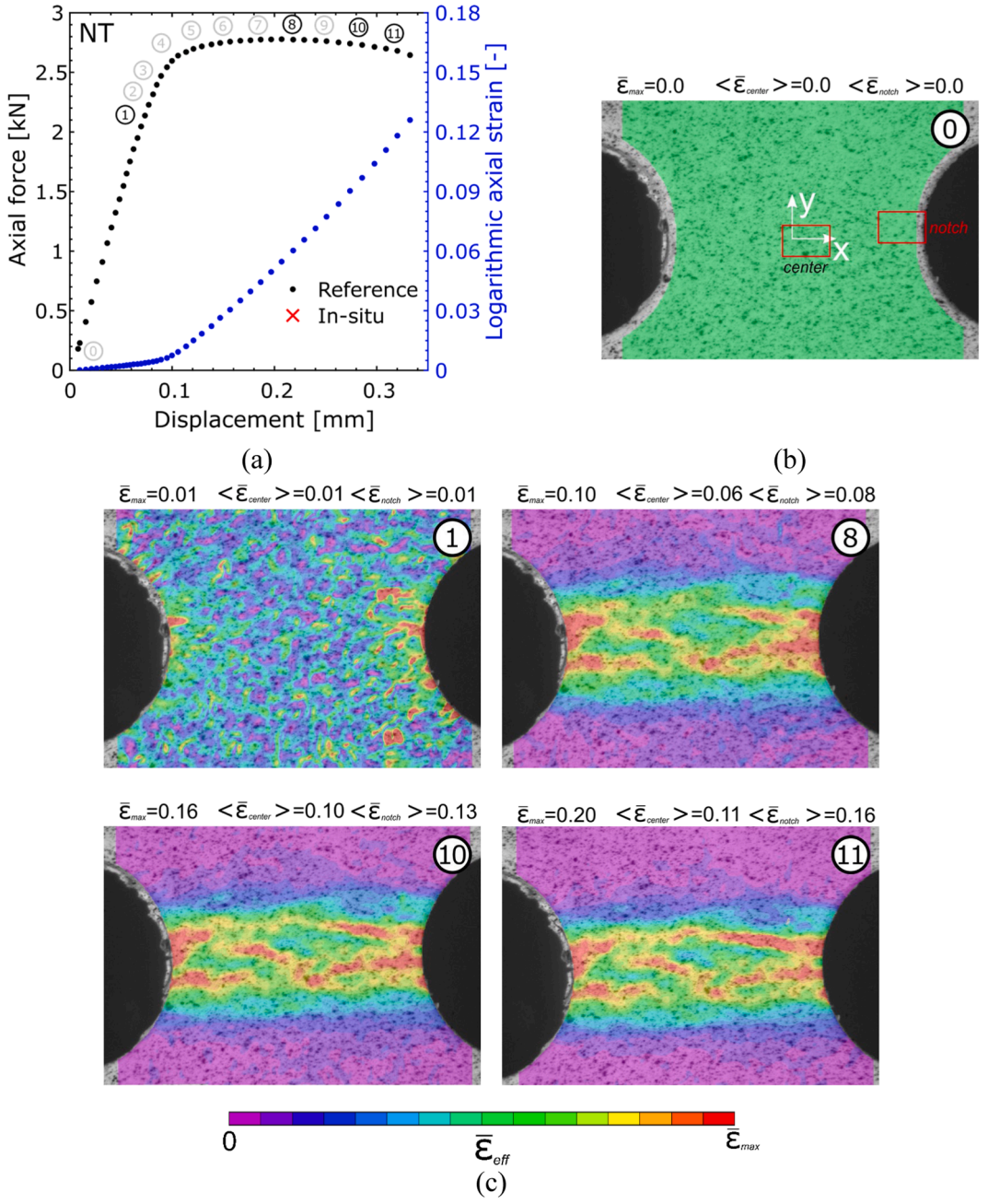

Fig. D1. Notched Tension experiment: (a) Force-displacement curves for the macroscopic (solid black line) and the eleven in-situ laminography load steps (red crosses). (b) Laminography experiment as seen by the optical camera. The green area denote the regions of interest for DIC, the red boxes the regions of interest observed by laminography. (c) DIC contour plots for selected load steps.

Fig. D2 gives an overview of the reconstructed grayscale images for selected steps of the central regions of the notched tension (NT) experiment. Due to similarity in the observed features, the notch region is omitted here. Around the yield point (step ①, Fig. D2a) several intermetallic particles with diameters of up to 15 μm are observed. None of these shows any signs of cracking or matrix debonding. Significant changes are then witnessed around the force maximum (step ⑧, Fig. D2b). The initially uncracked particles show distinct cracks that form perpendicular to the direction of loading (i.e. they lie in the RD-TH plane); inside the matrix material, a microcrack that extends about 171 μm along the specimen width direction (RD-direction) is visible. In its vicinity, laminographic artefacts (visible as blurry shapes) indicate the proximity of more microcracks at different planes; these become apparent in the observed plane as they grow during loading steps ⑩ and ⑪. At this last step before fracture, several microcracks can be seen, one of which has grown to >500 μm along grain boundaries. At the same time, other cracks that initiated from second phase particles seem to have stopped evolving.

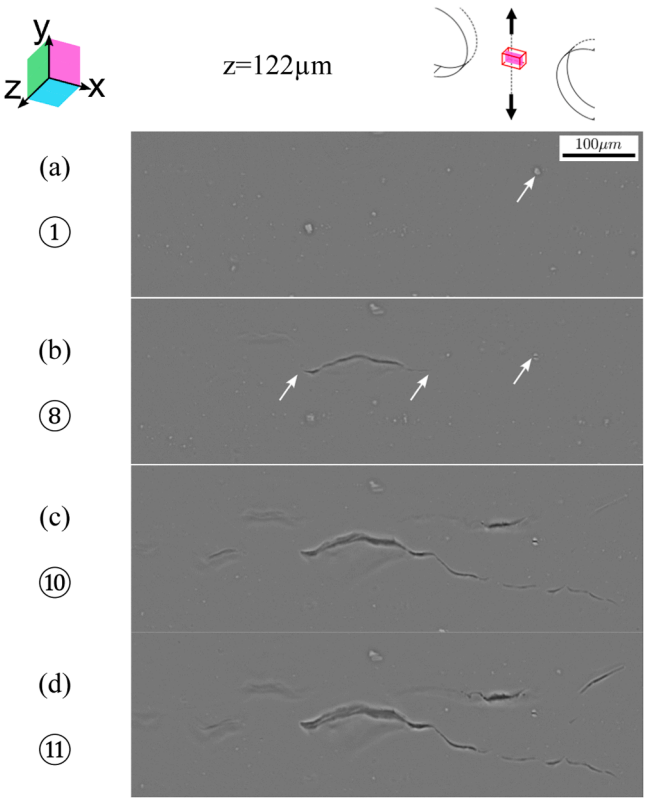

Fig. D2. Laminography images of the notched tension specimen center at selected steps. (a) ① base material with second phase particles (white arrow), (b) ⑧ cracked second phase particles and micro-cracks are visible (white arrows), (c-d) ⑩&⑪ which further grow perpendicular and inclined to the loading direction.

The projected 3D views of the segmented volumes of the central and notch region of the NT specimen are shown in Figs. D3 and D4. Both regions show larger elongated microcracks around the force maximum (step ⑧, Figs. D3b and D4b). As seen in the grayscale images, these voids grow significantly in a stable manner towards final fracture. It is noteworthy that over the central region microcracks appear and grow at several locations, while in the notch region a distinct separation of a zone with almost no large cracks about 500 μm from the free boundary is observed in the x-y and x-z plane. This is attributed to the gradual change in stress state from uniaxial tension on the free boundary, to plane strain tension in the central region of the specimen. At the same time, the formation of two bands of concentrated voids is observed in the y-z plane, most prominent in the last two steps (Fig. D4c,d). While the bands appear to be balanced in step ⑩, a clear localization in the positive y-and z-axis is observed in ⑪. It is speculated that this will be the plane of final localization preceding fracture.

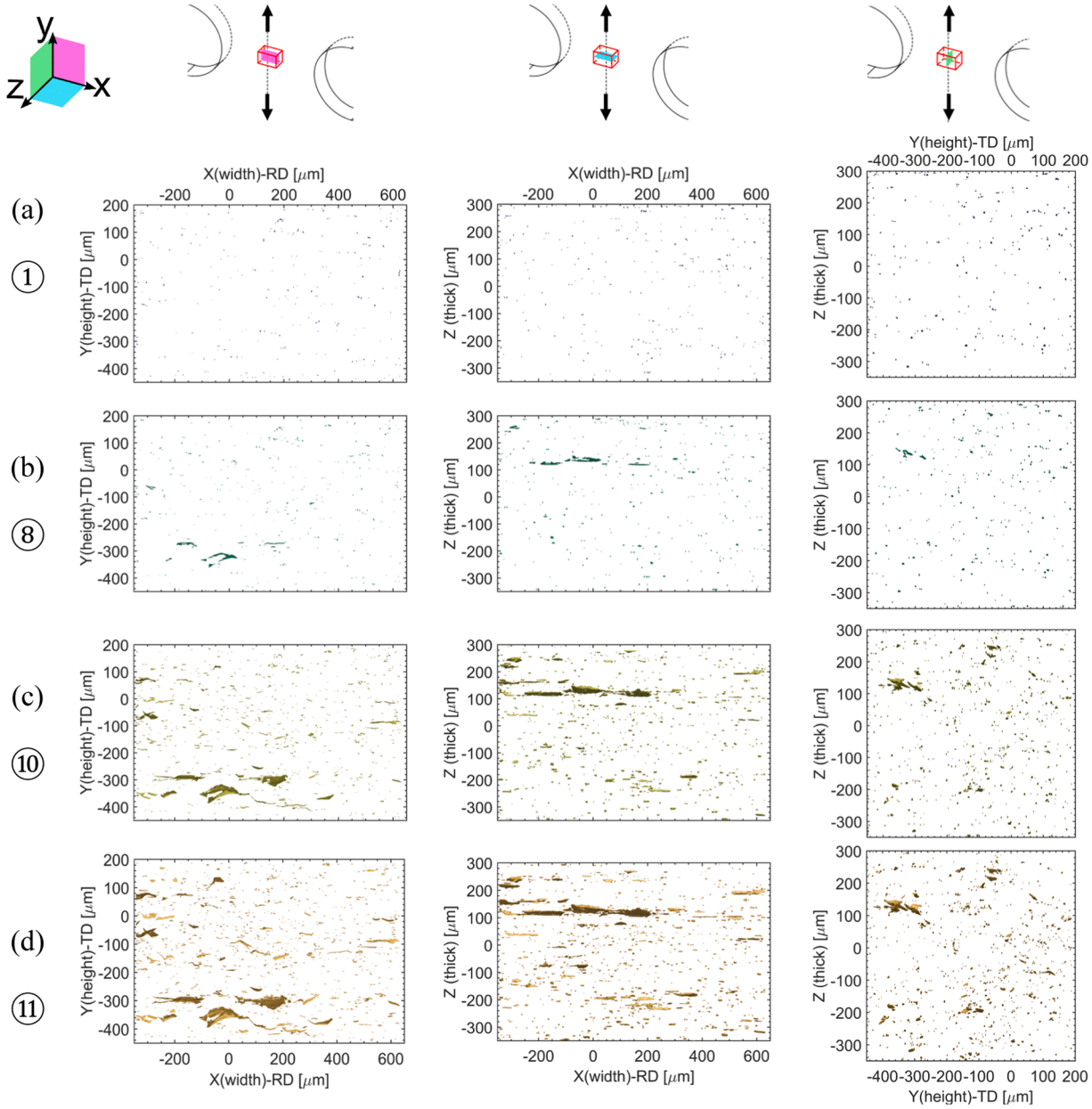

Fig. D3. Projected 3D views of the segmented volume of the NT center for selected steps. The matrix material has been made transparent for visibility.

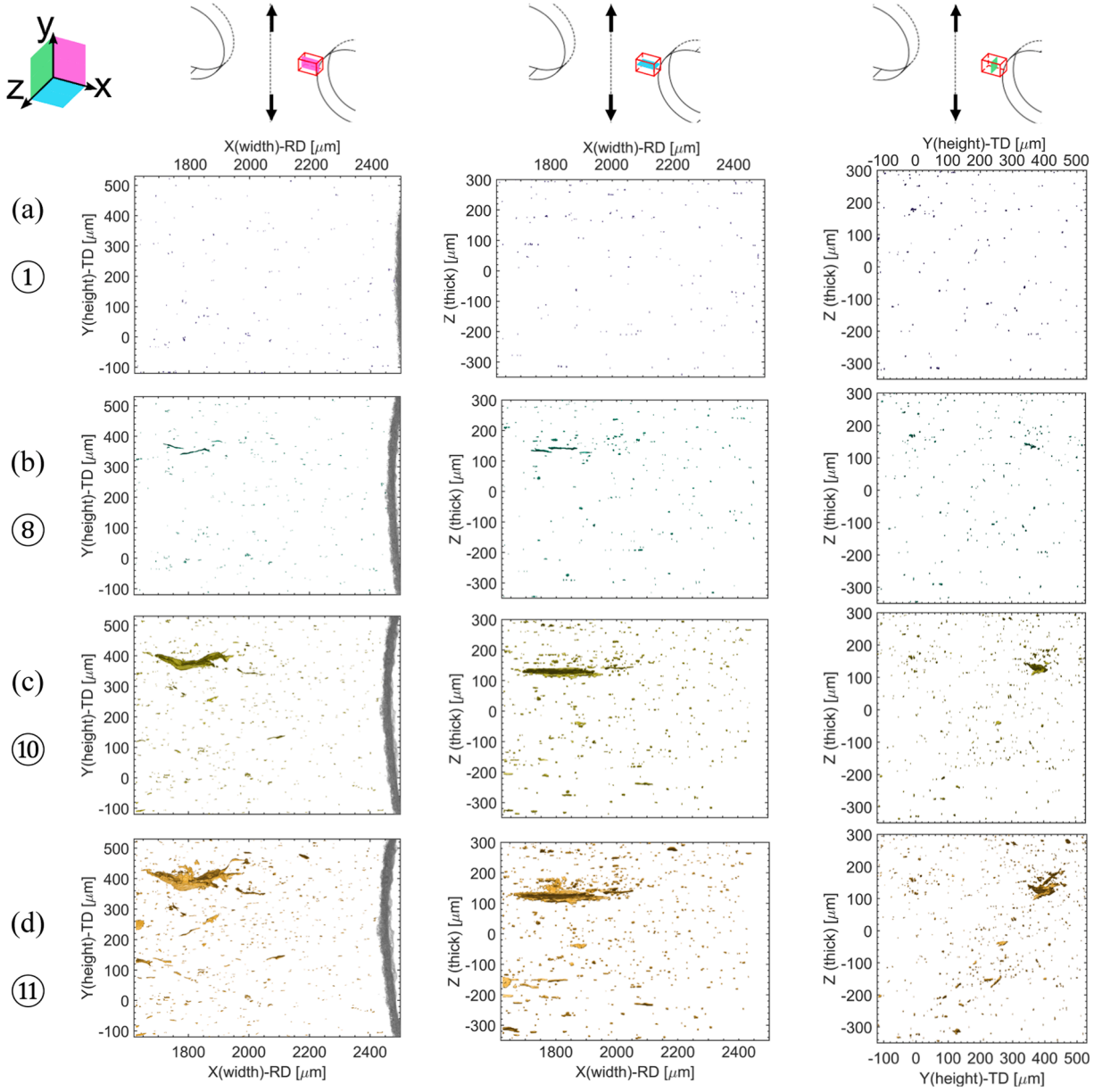

Fig. D4. Projected 3D views of the segmented volume of the NT notch for selected steps. The notch is shown in light grey in the x-y plane for reference. The matrix material has been made transparent for visibility.

The results of post-mortem fractography on the notched specimen's central region are shown in Fig D5. All zones show severe ductile deformation. The lamellar in-plane grain structure is clearly visible, with strongly necked grains of (partially) zero thickness. Ductile dimples with shattered micron-sized second phase particles at their bottom are visible along the necking lines of the grains.

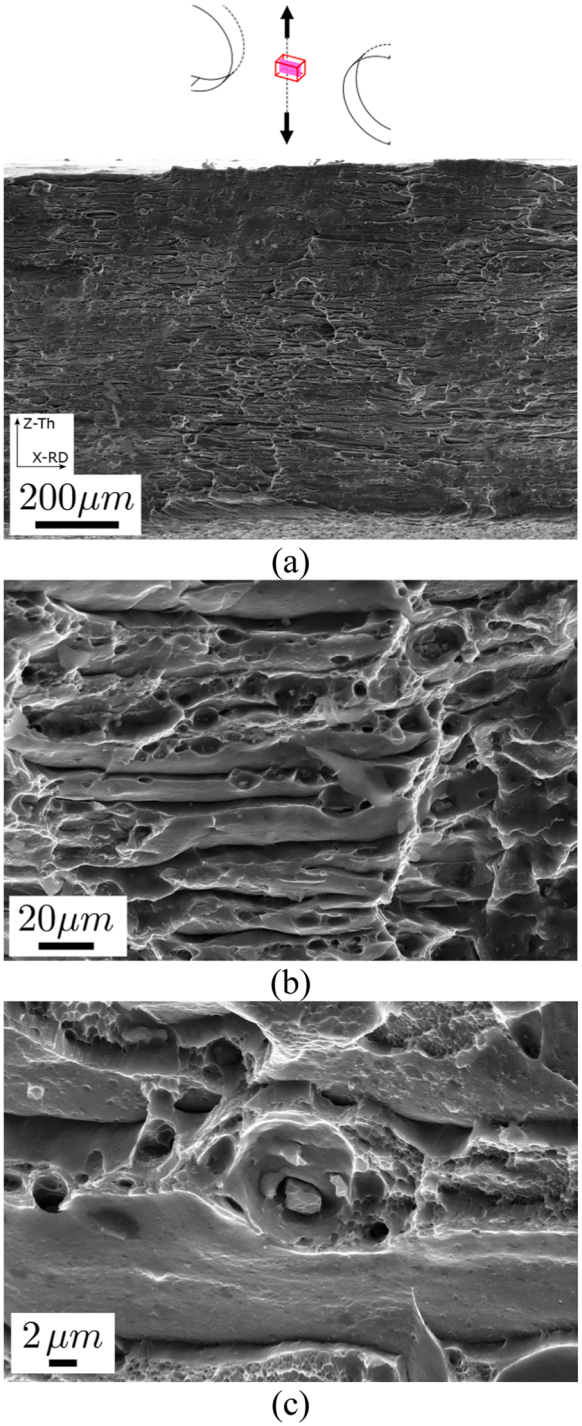

Fig. D5. Fractography of the macroscopic notched tension specimen for the central region. (a) Selected region of interest close to the specimen center, (b, c) close-up of ductile dimples with (partially cracked) intermetallic particles at the bottom. Clearly visible is the lamellar/layered microstructure and intergranular failure.

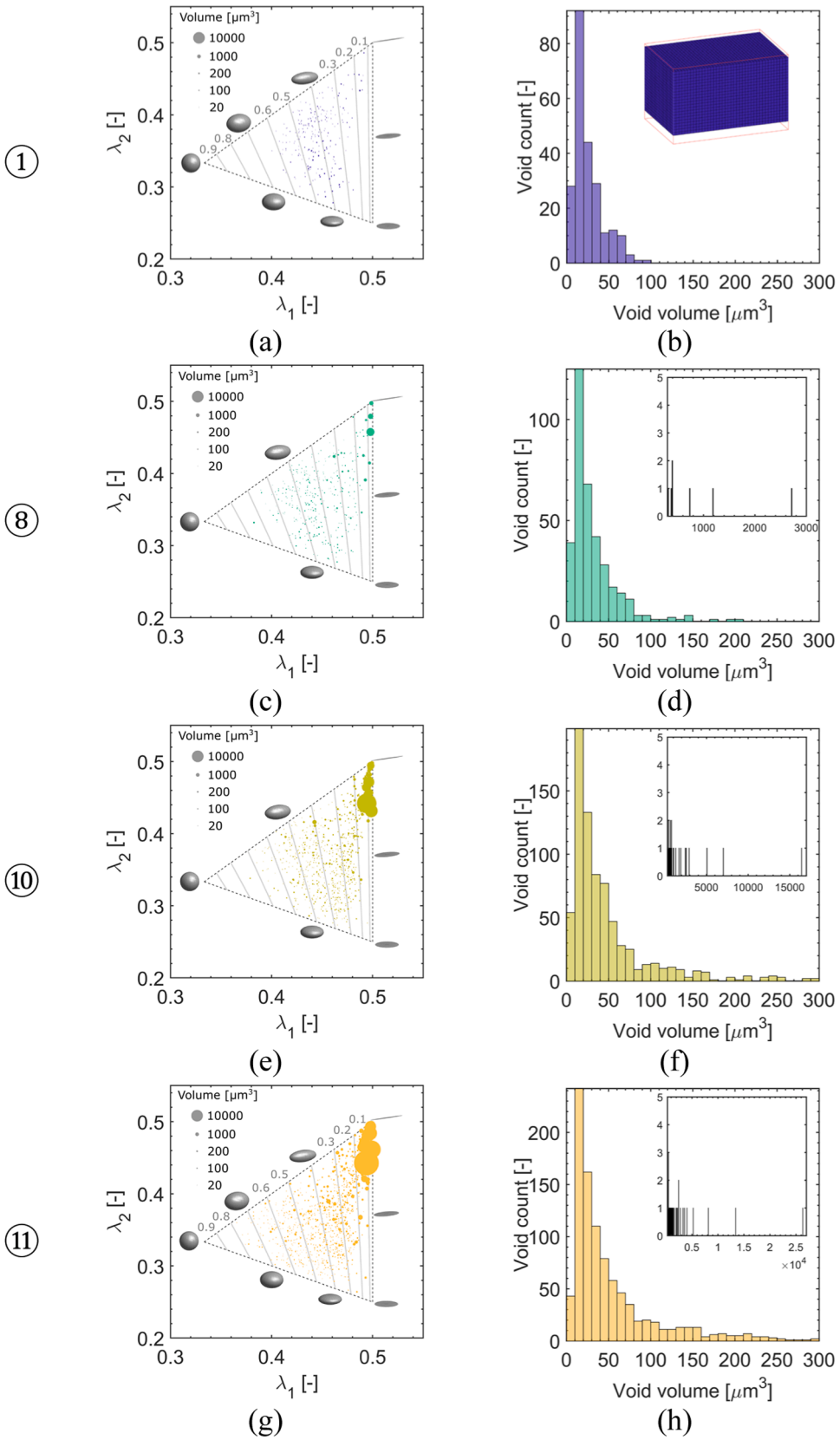

Fig. D6. Detailed void population analysis of the NT-center region for selected loading steps. Left column: evolution of the void shape (λ_1 vs. λ_2). Right column: Evolution of void count vs. void volume. Dashed lines denote constant Feret shape factors. The disc area scales linearly with the void volume.

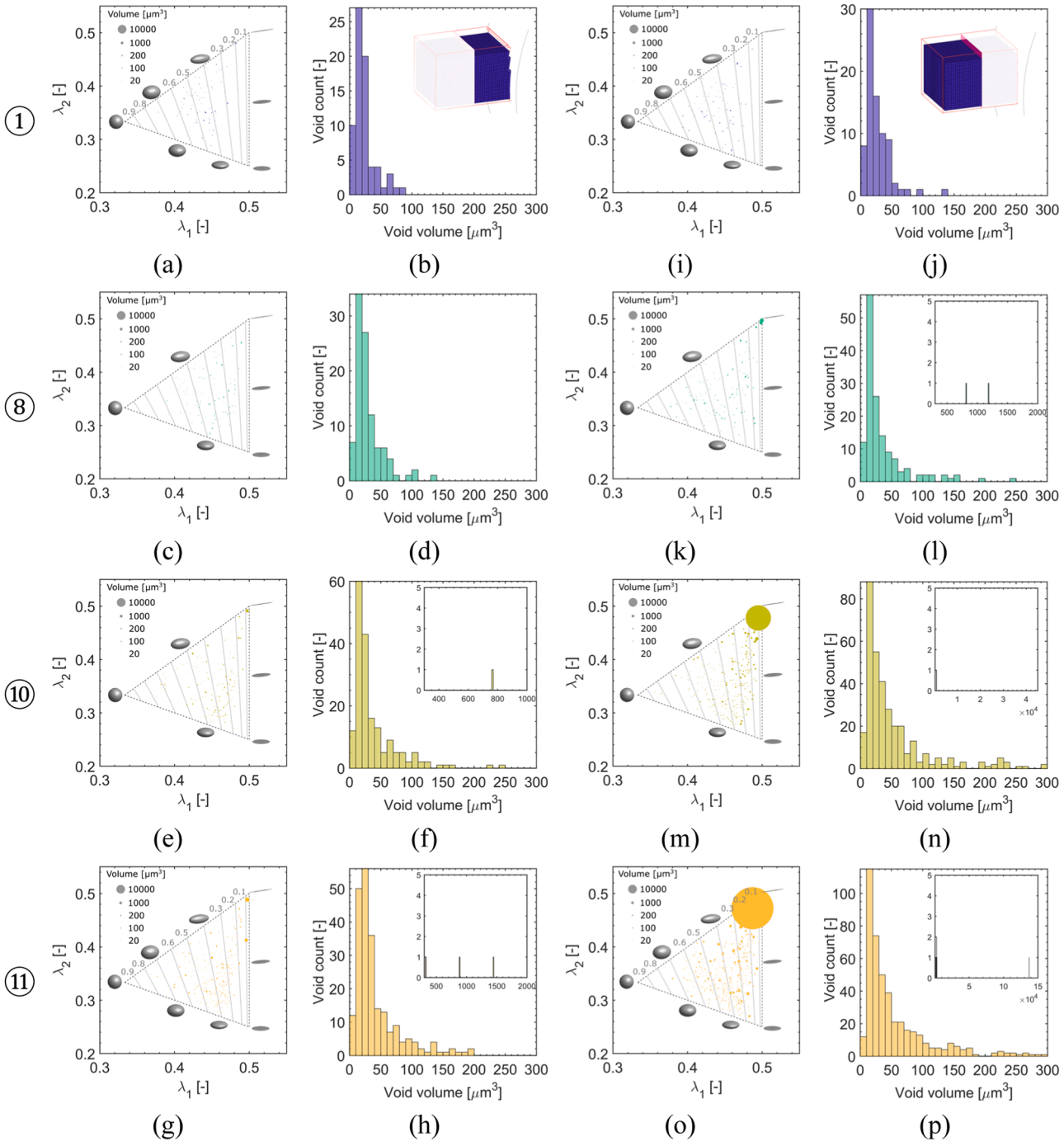

Fig. D7. Detailed void population analysis of the NT-notch/edge (a-h) and NT-notch/center (i-p) regions for selected loading steps. Left column: evolution of the void shape (λ_1 vs. λ_2). Right column: Evolution of void count vs. void volume. Dashed lines denote constant Feret shape factors. The disc area scales linearly with the void volume.

Appendix E. Extended experimental results on CT specimen

For the compact tension (CT) specimen no additional macroscopic experiment is performed. It should be noted that this experiment has already been presented in [43,65]. Fig. E1 shows reconstructed grayscale slices taken from the xy-plane at $z=-92$ µm) for selected loading stages. During the elastic step (①), mainly second phase particles are observed with only a few voids present in and around those particles (white arrows). Upon further loading, more particle-matrix decohesion and intermetallic cracking occurs (step ③) and initial micro-cracks in the matrix material are observed. The subsequent loading steps before fracture (④ and ⑤) show significant void growth as well as coalescence, mainly from the voids in the matrix material. The voids located around the second phase particles do not evolve significantly in size. It should be noted that due to the out-of-plane necking of the material, the observed plane changes slightly as some material (and voids) drift in and out of the plane.

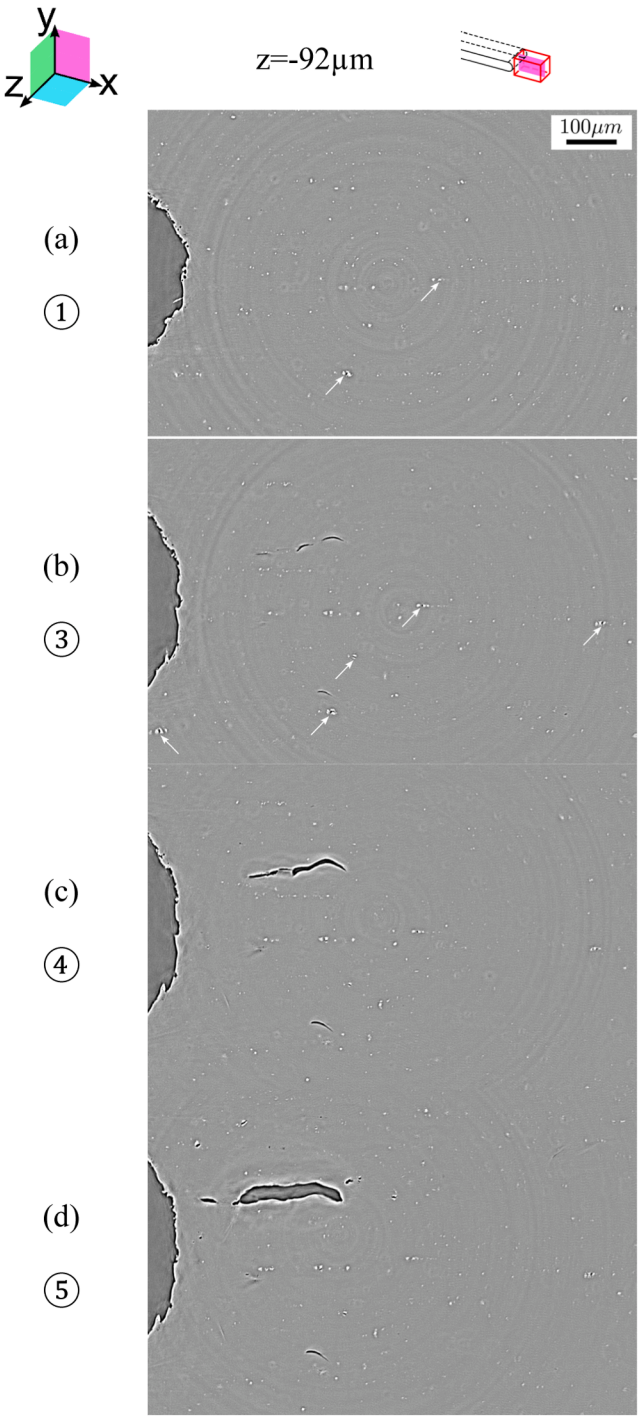

Fig. E1. Laminography images of the compact tension experiment at selected steps. (a) ① base material with intermetallic particles (white arrows), (b) ③ micro-cracks become visible and grow (c-d) ④& ⑤ perpendicular and inclined to the loading direction.

When looking at the projected 3D views of the reconstructed volumes, the observations from the cut slices can be mapped to the whole volume (Fig. E2). Initially scattered small voids (step ①) are replaced increasingly by growing voids and micro-cracks appearing at several locations. This occurs along with the beginning of coalescence (from step ③ to ④) and the formation of very large voids just before the onset of fracture (step ⑤). It is noteworthy that the micro-cracks and voids form directly behind the machined notch (xy-plane) and across the whole observed volume (xz-plane). The yz-plane indirectly reveals the strain gradient that fosters the preferred growth of the voids along a slanted, almost cross shaped trajectory.

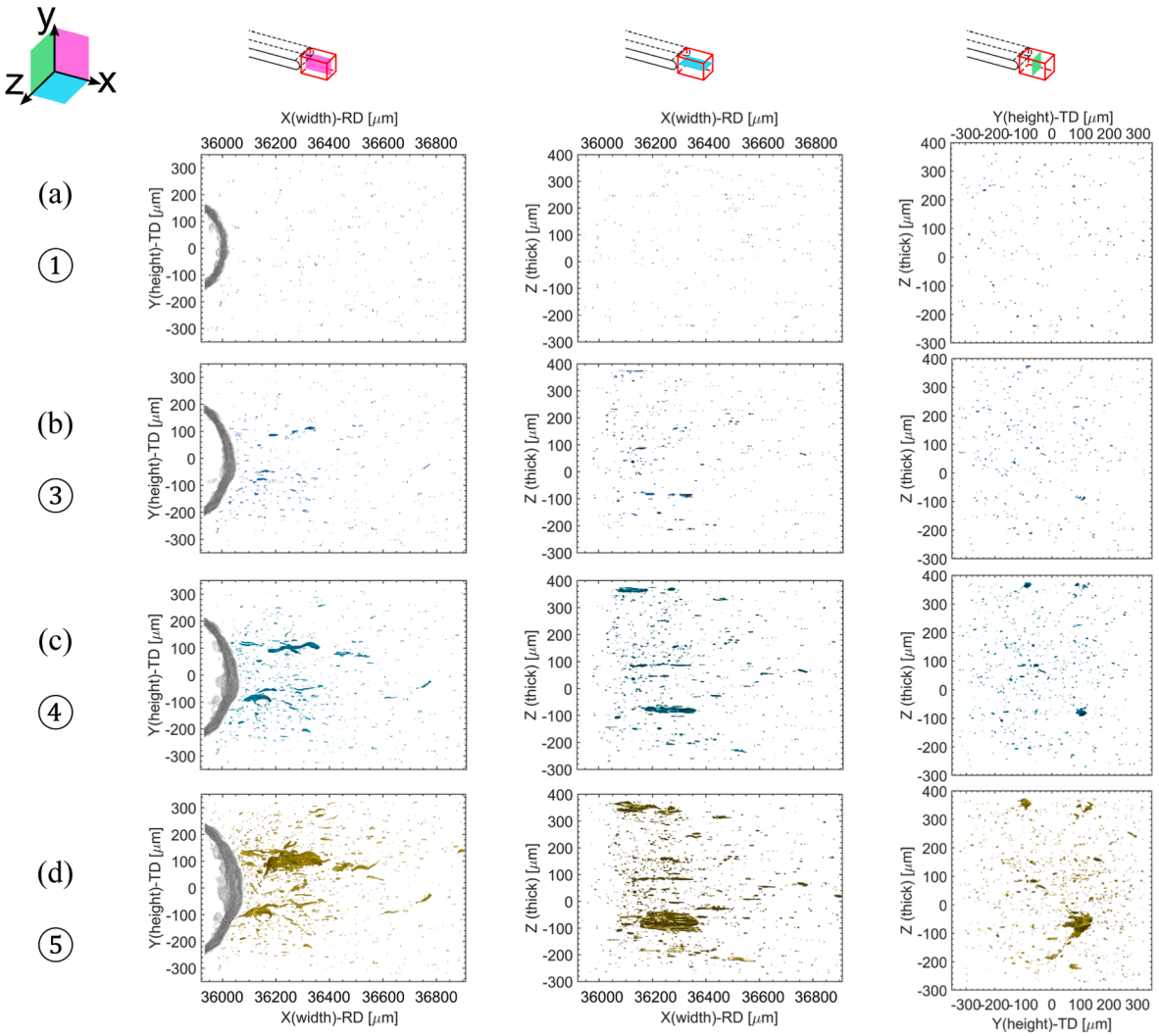

Fig. E2. Projected 3D views of the segmented volume of the CT experiment for selected steps. The notch is shown in light grey in the x-y plane for reference. The matrix material has been made transparent for visibility.

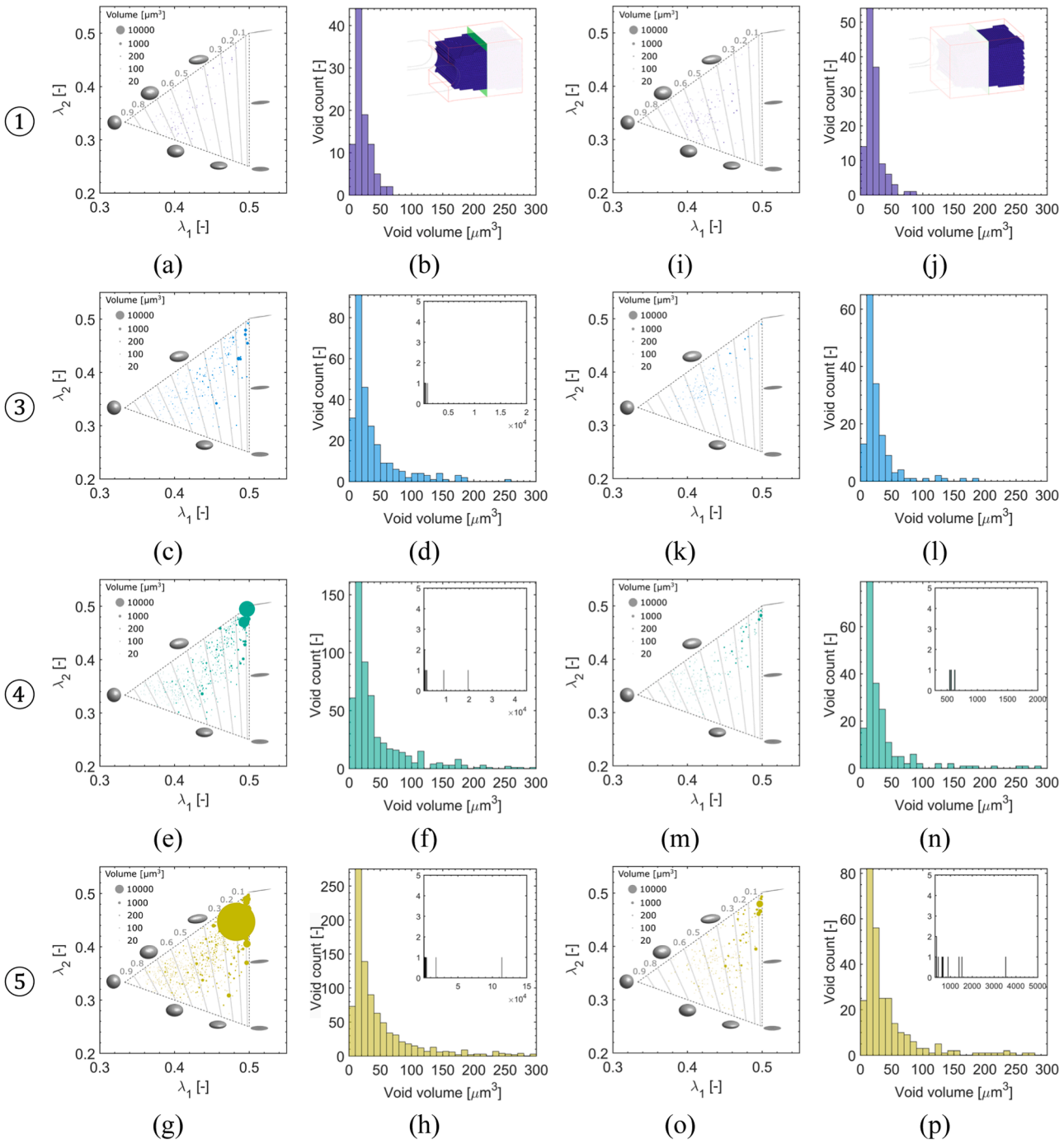

Fig. E3. Detailed void population analysis of the CT-edge (a-h) and CT-center (i-p) regions for selected loading steps. Left column: evolution of the void shape (λ_1 vs. λ_2). Right column: Evolution of void count vs. void volume. Dashed lines denote constant Feret shape factors. The disc area scales linearly with the void volume.

References

[1] A. Pineau, A.A. Benzerga, T. Pardoen, Failure of metals I: Brittle and ductile fracture, Acta Mater 107 (2016) 424–483, https://doi.org/10.1016/j.actamat.2015.12.034.

[2] F.A. McClintock, A Criterion for Ductile Fracture by the Growth of Holes, J. Appl. Mech. 35 (1968) 363–371, https://doi.org/10.1115/1.3601204.

[3] J.R. Rice, D.M. Tracey, On the ductile enlargement of voids in triaxial stress fields*, J. Mech. Phys. Solids 17 (1969) 201–217, https://doi.org/10.1016/0022-5096(69)90033-7.

[4] A.L. Gurson, Continuum Theory of Ductile Rupture by Void Nucleation and Growth: Part I—Yield Criteria and Flow Rules for Porous Ductile Media, J. Eng. Mater. Technol. 99 (1977) 2–15, https://doi.org/10.1115/1.3443401.

[5] C.C. Chu, A. Needleman, Void Nucleation Effects in Biaxially Stretched Sheets, J. Eng. Mater. Technol. 102 (1980) 249–256, https://doi.org/10.1115/1.3224807.

[6] V. Tvergaard, Influence of voids on shear band instabilities under plane strain conditions, Int. J. Fract. 17 (1981) 389–407, https://doi.org/10.1007/BF00036191.

[7] V. Tvergaard, A. Needleman, Analysis of the cup-cone fracture in a round tensile bar, Acta Metall 32 (1984) 157–169, https://doi.org/10.1016/0001-6160(84)90213-X.

[8] I.A. Khan, A.A. Benzerga, A. Needleman, A shear modified enhanced Gurson constitutive relation and implications for localization, J. Mech. Phys. Solids 171 (2023) 105153, https://doi.org/10.1016/J.JMPS.2022.105153.

[9] A.R. Ferreira, S.P.B. Proença, A. Benallal, Yield criteria for voided materials with anisotropic matrix behavior, Eur. J. Mech. - A/Solids 104 (2024) 105079, https://doi.org/10.1016/J.EUROMECHSOL.2023.105079.

[10] A.S. Khan, H. Zhang, Mechanically alloyed nanocrystalline iron and copper mixture: behavior and constitutive modeling over a wide range of strain rates, Int. J. Plast. 16 (2000) 1477–1492, https://doi.org/10.1016/S0749-6419(00)00024-3.
[11] K. Danas, P.Ponte Castañeda, Influence of the Lode parameter and the stress triaxiality on the failure of elasto-plastic porous materials, Int. J. Solids Struct. 49 (2012) 1325–1342, https://doi.org/10.1016/j.ijsolstr.2012.02.006.
[12] M. Gologanu, J.B. Leblond, J. Devaux, Approximate models for ductile metals containing non-spherical voids—Case of axisymmetric prolate ellipsoidal cavities, J. Mech. Phys. Solids 41 (1993) 1723–1754, https://doi.org/10.1016/0022-5096(93)90029-F.
[13] K. Madou, J.B. Leblond, A Gurson-type criterion for porous ductile solids containing arbitrary ellipsoidal voids—I: Limit-analysis of some representative cell, J. Mech. Phys. Solids 60 (2012) 1020–1036, https://doi.org/10.1016/j.jmps.2011.11.008.
[14] K. Nahshon, J.W. Hutchinson, Modification of the Gurson Model for shear failure, Eur. J. Mech. - A/Solids 27 (2008) 1–17, https://doi.org/10.1016/j.euromechsol.2007.08.002.
[15] L.E. Dæhli, D. Morin, T. Børvik, O.S. Hopperstad, A Lode-dependent Gurson model motivated by unit cell analyses, Eng. Fract. Mech. 190 (2018) 299–318, https://doi.org/10.1016/J.ENGFRACMECH.2017.12.023.
[16] G. Han, J. He, S. Li, Simple shear deformation of sheet metals: finite strain perturbation analysis and high-resolution quasi-in-situ strain measurement, Int. J. Plast. (2021) 103194, https://doi.org/10.1016/J.IJPLAS.2021.103194.
[17] P.F. Thomason, A three-dimensional model for ductile fracture by the growth and coalescence of microvoids, Acta Metall 33 (1985) 1087–1095, https://doi.org/10.1016/0001-6160(85)90202-0.
[18] T. Pardoen, J.W. Hutchinson, An extended model for void growth and coalescence, J. Mech. Phys. Solids 48 (2000) 2467–2512, https://doi.org/10.1016/S0022-5096(00)00019-3.
[19] A.A. Benzerga, Micromechanics of coalescence in ductile fracture, J. Mech. Phys. Solids 50 (2002) 1331–1362, https://doi.org/10.1016/S0022-5096(01)00125-9.
[20] C. Tekoglu, J.B. Leblond, T. Pardoen, A criterion for the onset of void coalescence under combined tension and shear, J. Mech. Phys. Solids 60 (2012) 1363–1381, https://doi.org/10.1016/J.JMPS.2012.02.006.
[21] L. Babout, Y. Brechet, E. Maire, R. Fougères, On the competition between particle fracture and particle decohesion in metal matrix composites, Acta Mater 52 (2004) 4517–4525, https://doi.org/10.1016/J.ACTAMAT.2004.06.009.
[22] N.A. Fleck, J.W. Hutchinson, V. Tvergaard, Softening by void nucleation and growth in tension and shear, J. Mech. Phys. Solids 37 (1989) 515–540, https://doi.org/10.1016/0022-5096(89)90027-6.
[23] M.F. Horstemeyer, J. Lathrop, A.M. Gokhale, M. Dighe, Modeling stress state dependent damage evolution in a cast Al?Si?Mg aluminum alloy, Theor. Appl. Fract. Mech. 33 (2000) 31–47, https://doi.org/10.1016/S0167-8442(99)00049-X.
[24] T.F. Morgeneyer, J. Besson, Flat to slant ductile fracture transition: Tomography examination and simulations using shear-controlled void nucleation, Scr. Mater. 65 (2011) 1002–1005, https://doi.org/10.1016/j.scriptamat.2011.09.004.
[25] E. Maire, P.J. Withers, Quantitative X-ray tomography, Int. Mater. Rev. 59 (2014) 1–43, https://doi.org/10.1179/1743280413Y.0000000023.
[26] C. Landron, O. Bouaziz, E. Maire, J. Adrien, Characterization and modeling of void nucleation by interface decohesion in dual phase steels, Scr. Mater. 63 (2010) 973–976, https://doi.org/10.1016/J.SCRIPTAMAT.2010.07.021.
[27] H. Toda, A. Takijiri, M. Azuma, S. Yabu, K. Hayashi, D. Seo, M. Kobayashi, K. Hirayama, A. Takeuchi, K. Uesugi, Damage micromechanisms in dual-phase steel investigated with combined phase- and absorption-contrast tomography, Acta Mater 126 (2017) 401–412, https://doi.org/10.1016/J.ACTAMAT.2017.01.010.
[28] E. Maire, S. Zhou, J. Adrien, M. Dimichiel, Damage quantification in aluminium alloys using in situ tensile tests in X-ray tomography, Eng. Fract. Mech. 78 (2011) 2679–2690, https://doi.org/10.1016/J.ENGFRACMECH.2011.07.004.
[29] C. Landron, E. Maire, O. Bouaziz, J. Adrien, L. Lecarme, A. Bareggi, Validation of void growth models using X-ray microtomography characterization of damage in dual phase steels, Acta Mater 59 (2011) 7564–7573, https://doi.org/10.1016/J.ACTAMAT.2011.08.046.
[30] B.P. Croom, H. Jin, P.J. Noell, B.L. Boyce, X. Li, Collaborative ductile rupture mechanisms of high-purity copper identified by in situ X-ray computed tomography, Acta Mater 181 (2019) 377–384, https://doi.org/10.1016/J.ACTAMAT.2019.10.005.
[31] Y. Madi, J.M. Garcia, H. Proudhon, Y. Shinohara, L. Helfen, J. Besson, T. F. Morgeneyer, On the Origin of the Anisotropic Damage of X100 Line Pipe Steel: Part I—In Situ Synchrotron Tomography Experiments, Integr. Mater. Manuf. Innov. 8 (2019) 570–596, https://doi.org/10.1007/S40192-019-00165-0/FIGURES/34.
[32] F. Hannard, A. Simar, E. Maire, T. Pardoen, Quantitative assessment of the impact of second phase particle arrangement on damage and fracture anisotropy, Acta Mater 148 (2018) 456–466, https://doi.org/10.1016/J.ACTAMAT.2018.02.003.
[33] M.W. Vaughan, H. Lim, B. Pham, R. Seede, A.T. Polonsky, K.L. Johnson, P.J. Noell, The mechanistic origins of heterogeneous void growth during ductile failure, Acta Mater 274 (2024) 119977, https://doi.org/10.1016/J.ACTAMAT.2024.119977.
[34] L. Lecarme, E. Maire, A. Kumar, C. De Vleeschouwer, L. Jacques, A. Simar, T. Pardoen, Heterogenous void growth revealed by in situ 3-D X-ray microtomography using automatic cavity tracking, Acta Mater 63 (2014) 130–139, https://doi.org/10.1016/J.ACTAMAT.2013.10.014.
[35] M.A. Azman, C.Le Bourlot, A. King, D. Fabrègue, E. Maire, 4D characterisation of void nucleation, void growth and void coalescence using advanced void tracking algorithm on in situ X-ray tomographic data, Mater. Today Commun. 32 (2022) 103892, https://doi.org/10.1016/J.MTCOMM.2022.103892.
[36] Y. Guo, T.L. Burnett, S.A. McDonald, M. Daly, A.H. Sherry, P.J. Withers, 4D imaging of void nucleation, growth, and coalescence from large and small inclusions in steel under tensile deformation, J. Mater. Sci. Technol. 123 (2022) 168–176, https://doi.org/10.1016/J.JMST.2022.01.024.
[37] L. Helfen, T. Baumbach, P. Mikul??k, D. Kiel, P. Pernot, P. Cloetens, J. Baruchel, High-resolution three-dimensional imaging of flat objects by synchrotron-radiation computed laminography, Appl. Phys. Lett. 86 (2005) 1–3, https://doi.org/10.1063/1.1854735.
[38] L. Helfen, T.F. Morgeneyer, F. Xu, M.N. Mavrogordato, I. Sinclair, B. Schillinger, T. Baumbach, Synchrotron and neutron laminography for three-dimensional imaging of devices and flat material specimens, Int. J. Mater. Res. 103 (2012) 170–173, https://doi.org/10.3139/146.110668/MACHINEREADABLECITATION/RIS.
[39] A. Buljac, X. Kong, L. Helfen, F. Hild, T.F. Morgeneyer, Shear loading dominated damage mechanisms and strain localization studied by in situ 3D laminography imaging and Digital Volume Correlation for AA2198-T8, Mech. Mater. (2023) 104558, https://doi.org/10.1016/J.MECHMAT.2023.104558.
[40] X. Kong, M. Hurst, L. Helfen, F. Gaslain, T. Baumbach, H. Suhonen, T. F. Morgeneyer, Ductile shear damage micromechanisms studied by correlative multiscale nanotomography and SEM/EBSD for a recrystallized aluminum alloy 2198 T8, J. Mater. Sci. 59 (2024) 13690–13708, https://doi.org/10.1007/S10853-024-09933-6/FIGURES/15.
[41] X. Kong, L. Helfen, M. Hurst, D. Hänschke, D. Missoum-Benziane, J. Besson, T. Baumbach, T.F. Morgeneyer, 3D in situ study of damage during a 'shear to tension' load path change in an aluminium alloy, Acta Mater 231 (2022) 117842, https://doi.org/10.1016/J.ACTAMAT.2022.117842.
[42] X. Kong, J. Chen, Y. Madi, D. Missoum-Benziane, J. Besson, T.F. Morgeneyer, Plasticity and ductility of an anisotropic recrystallized AA2198 Al-Cu-Li alloy in T3 and T8 conditions during proportional and non-proportional loading paths: simulations and experiments, J. Theor. Comput. Appl. Mech. (2023), https://doi.org/10.46298/JTCAM.8913.
[43] T.F. Morgeneyer, T. Taillandier-Thomas, L. Helfen, T. Baumbach, I. Sinclair, S. Roux, F. Hild, In situ 3-D observation of early strain localization during failure of thin Al alloy (2198) sheet, Acta Mater 69 (2014) 78–91, https://doi.org/10.1016/J.ACTAMAT.2014.01.033.
[44] X. Kong, T.F. Morgeneyer, D. Missoum-Benziane, G. Rousselier, A polycrystalline damage model applied to an anisotropic aluminum alloy 2198 under non-proportional load path changes, Int. J. Plast. (2023) 103674, https://doi.org/10.1016/J.IJPLAS.2023.103674.
[45] N. Nayan, S.V.S. Narayana Murty, R. Sarkar, A.K. Mukhopadhyay, S. Ahlawat, S. K. Sarkar, M.J.N.V. Prasad, I. Samajdar, The Anisotropy of Serrated Flow Behavior of Al-Cu-Li (AA2198) Alloy, Metall. Mater. Trans. A Phys. Metall. Mater. Sci. 50 (2019) 5066–5078, https://doi.org/10.1007/S11661-019-05431-6/FIGURES/10.
[46] C.C. Roth, D. Mohr, Ductile fracture experiments with locally proportional loading histories, Int. J. Plast. (2016), https://doi.org/10.1016/j.ijplas.2015.08.004.
[47] P.A. Douissard, A. Cecilia, X. Rochet, X. Chapel, T. Martin, T. Van De Kamp, L. Helfen, T. Baumbach, L. Luquot, X. Xiao, J. Meinhardt, A. Rack, A versatile indirect detector design for hard X-ray microimaging, J. Instrum. 7 (2012) P09016, https://doi.org/10.1088/1748-0221/7/09/P09016.
[48] A. Myagotin, A. Voropaev, L. Helfen, D. Hänschke, T. Baumbach, Efficient Volume Reconstruction for Parallel-Beam Computed Laminography by Filtered Backprojection on Multi-Core Clusters, IEEE Trans. Image Process. 22 (2013) 5348–5361, https://doi.org/10.1109/TIP.2013.2285600.
[49] T. Faragó, S. Gasilov, I. Emslie, M. Zuber, L. Helfen, M. Vogelgesang, T. Baumbach, Tofu: a fast, versatile and user-friendly image processing toolkit for computed tomography, J. Synchrotron Radiat. 29 (2022) 916, https://doi.org/10.1107/S160057752200282X.
[50] M. Vogelgesang, T. Farago, T.F. Morgeneyer, L. Helfen, T. dos Santos Rolo, A. Myagotin, T. Baumbach, Real-time image-content-based beamline control for smart 4D X-ray imaging, J. Synchrotron Radiat. 23 (2016) 1254–1263, https://doi.org/10.1107/S1600577516010195.
[51] P. Cloetens, M. Pateyron-Salomé, J.Y. Buffière, G. Peix, J. Baruchel, F. Peyrin, M. Schlenker, M. Pateyron-Salomé, J.Y. Buffiè, G. Peix, J. Baruchel, F. Peyrin, M. Schlenker, Observation of microstructure and damage in materials by phase sensitive radiography and tomography, J. Appl. Phys. 81 (1997) 5878–5886, https://doi.org/10.1063/1.364374.
[52] C.C. Roth, D. Mohr, Effect of strain rate on ductile fracture initiation in advanced high strength steel sheets: Experiments and modeling, Int. J. Plast. 56 (2014) 19–44, https://doi.org/10.1016/j.ijplas.2014.01.003.
[53] A. Buljac, L. Helfen, F. Hild, T.F. Morgeneyer, Effect of void arrangement on ductile damage mechanisms in nodular graphite cast iron: in situ 3D measurements, Eng. Fract. Mech. 192 (2018) 242–261, https://doi.org/10.1016/j.engfracmech.2018.01.008.
[54] W.H. Walton, W.H. Walton, Feret's Statistical Diameter as a Measure of Particle Size, Natur 162 (1948) 329–330, https://doi.org/10.1038/162329B0.
[55] E.P. Denis, C. Barat, D. Jeulin, C. Ducottet, 3D complex shape characterization by statistical analysis: Application to aluminium alloys, Mater. Charact. 59 (2008) 338–343, https://doi.org/10.1016/j.matchar.2007.01.012.
[56] C.C. Roth, T.F. Morgeneyer, Y. Cheng, L. Helfen, D. Mohr, Ductile damage mechanism under shear-dominated loading: in-situ tomography experiments on dual phase steel and localization analysis, Int. J. Plast. (2018), https://doi.org/10.1016/j.ijplas.2018.06.003.
[57] T. Tancogne-Dejean, C.C. Roth, T.F. Morgeneyer, L. Helfen, D. Mohr, Ductile damage of AA2024-T3 under shear loading: Mechanism analysis through in-situ laminography, Acta Mater 205 (2021) 116556, https://doi.org/10.1016/J.ACTAMAT.2020.116556.
[58] M. Hurst, L. Helfen, T.F. Morgeneyer, H. Suhonen, A. Buljac, F. Hild, J.P. Suuronen, T. Baumbach, D. Hänschke, Hierarchically guided in situ nanolaminography for the

visualisation of damage nucleation in alloy sheets, Sci. Reports 13 (2023) 1–11, https://doi.org/10.1038/s41598-022-27035-8, 2023 131.
[59] M. Gille, H. Proudhon, J. Oddershede, R. Quey, T.F. Morgeneyer, 3D strain heterogeneity and fracture studied by X-ray tomography and crystal plasticity in an aluminium alloy, Int. J. Plast. (2024) 104146, https://doi.org/10.1016/J.IJPLAS.2024.104146.
[60] C.P. Kohar, A. Zhumagulov, A. Brahme, M.J. Worswick, R.K. Mishra, K. Inal, Development of high crush efficient, extrudable aluminium front rails for vehicle lightweighting, Int. J. Impact Eng. 95 (2016) 17–34, https://doi.org/10.1016/j.ijimpeng.2016.04.004.
[61] M. Dunand, A.P. Maertens, M. Luo, D. Mohr, Experiments and modeling of anisotropic aluminum extrusions under multi-axial loading – Part I: Plasticity, Int. J. Plast. 36 (2012) 34–49, https://doi.org/10.1016/j.ijplas.2012.03.003.
[62] H.W. Swift, PLASTIC INSTABILITY UNDER, J. Mech. Phys. Solids 1 (1952).
[63] E. Voce, The relationship between stress and strain for homogeneous deformations, in: 1948.
[64] W.F. Hosford, A Generalized Isotropic Yield Criterion, J. Appl. Mech. 39 (1972) 607–609, https://doi.org/10.1115/1.3422732.
[65] A. Buljac, T. Taillandier-Thomas, T.F. Morgeneyer, L. Helfen, S. Roux, F. Hild, Slant strained band development during flat to slant crack transition in AA 2198 T8 sheet: in situ 3D measurements, Int. J. Fract. 200 (2016) 49–62, https://doi.org/10.1007/S10704-015-0052-Z/FIGURES/12.